

PhD TUTORIAL

Coherent control of spontaneous emission near a photonic band edge

Mesfin Woldeyohannes and Sajeev John

Department of Physics, University of Toronto, 60, St George Street, Toronto, ON, M5S 1A7, Canada

Received 6 August 2002

Published 14 February 2003

Online at stacks.iop.org/JOptB/5/R43

Abstract

We demonstrate the coherent control of spontaneous emission for a three-level atom located within a photonic band gap (PBG) material, with one resonant frequency near the edge of the PBG. Spontaneous emission from the three-level atom can be totally suppressed or strongly enhanced depending on the relative phase between the steady-state control laser coupling the two upper levels and the pump laser pulse used to create an excited state of the atom in the form of a coherent superposition of the two upper levels. Unlike the free-space case, the steady-state inversion of the atomic system is strongly dependent on the externally prescribed initial conditions. This non-zero steady-state population is achieved by virtue of the localization of light in the vicinity of the emitting atom. It is robust to decoherence effects provided that the Rabi frequency of the control laser field exceeds the rate of dephasing interactions. As a result, such a system may be relevant for a single-atom, phase-sensitive optical memory device on the atomic scale. The protected electric dipole within the PBG provides a basis for a qubit to encode information for quantum computations. A detailed literature survey on the nature, fabrication and applications of PBG materials is presented to provide context for this research.

Keywords: Photonic band gap materials, photon localization, coherent control, spontaneous emission, optical memory

(Some figures in this article are in colour only in the electronic version)

1. Introduction

Photonic band gap (PBG) materials are periodic dielectric structures that exhibit a range of frequencies for which electromagnetic wave propagation is classically forbidden. These systems lead to strong localization of light at the classical level and suppression of spontaneous emission, leading to interesting phenomena in quantum optics as well as important technological applications. Near a photonic band edge, spontaneous emission is anomalous and leads to fractionalized steady-state inversion for a single atom. On the other hand, driving a multi-level atom with a sufficiently strong resonant field alters the radiative dynamics in a fundamental way, even in ordinary vacuum. It leads to such interesting effects as the enhancement of the index of refraction

with greatly reduced absorption, electromagnetically induced transparency and optical amplification without population inversion.

In view of these results, it would be interesting to investigate the combined effects of coherent control by an external driving field and photon localization facilitated by a PBG on spontaneous emission from a three-level atom embedded in a PBG material. This is precisely what is done in this paper. In section 2 an extensive literature survey on the nature, fabrication and applications of PBG materials is presented to provide context for this research. Section 3 introduces the model system in the leading approximation, whereby a number of spontaneous emission effects and non-radiative interactions are neglected. It is demonstrated that storage of quantum information in a single three-level atom is

facilitated by the localization of light in the vicinity of the atom, suggesting an application of the model system as a memory device on the atomic scale.

The effects of higher-order terms on the basic results found in section 3 are discussed in section 4. This includes a semi-quantitative analysis of phonon-relaxation mechanisms for the model system. We have demonstrated that such dephasing effects can be offset by intense driving fields. Different ways of realization of the model system are also discussed in section 4.

The appendices contain supplementary material. The Hamiltonian of a three-level atom interacting with a quantized radiation field is derived in appendix A. The various expressions for the Green functions used in the main body of the paper are calculated in appendix B. Solution of the relevant equations of motion by means of Laplace transformation and the complex inversion formula is carried out in appendix C. Details of the quantum beats problem for both the free-space and PBG cases are discussed in appendix D. The radiative dynamics of a two-level atom embedded in a PBG material is discussed in appendix E.

2. Photonic band gap materials: introductory survey

2.1. Introduction

A new paradigm has emerged in which the band structure concepts of solid-state physics are applied to electromagnetism, leading to the invention of artificial electromagnetic crystal structures. These structures are called *photonic crystals* (PCs) and were originally proposed by John and Yablonovitch as a means to realize two fundamentally new optical principles—the localization and trapping of light in bulk material [1, 2], and the complete inhibition of spontaneous emission [3, 4] over a broad frequency range.

A PC is the photonic analogue of an electronic crystal. Rather than a periodic array of atoms which scatters and modifies the energy–momentum relation of electrons, a PC consists of a three-dimensionally ordered dielectric structure having spatially periodic dielectric constant, with a lattice parameter comparable to the wavelength of the electromagnetic wave. The band structure of a PC is referred to as a *photonic band structure* (PBS). Provided that the conditions of sufficiently high index-contrast between the high- and low-index regions, appropriate spatial structure, and dielectric filling ratio are met, photonic states inside a PC will be classified into bands separated by band gaps. These frequency gaps are termed PBGs and a PC with a PBG is often referred to as a *PBG material*. Figure 1 shows the PBS for the lowest ten bands of a PBG material made of silicon ($n = 3.45$) inverse opal. The PBG occurs between the eighth and ninth bands.

The concepts of reciprocal space, Brillouin zones, dispersion relations, Bloch wavefunctions, Van Hove singularities etc of solid-state physics are now being applied to PBG materials [5–9]. Unlike electrons in a semiconductor crystal which are constrained by Fermi statistics and therefore have to be excited from the valence band to the conduction band to become mobile, photons are bosons which propagate freely at frequencies both above and below the PBG. Thus the terms ‘valence band’ and ‘conduction band’ may not be appropriate

in the context of a PC. Instead, the bands above and below a PBG can be distinguished by applying the electromagnetic variational theorem [10]. According to this theorem, for modes in the lower photonic band, the power of modes lies primarily in the high-index regions, whereas for modes in the upper photonic band the power lies in the low-index regions. In PCs, the low-index regions are often air regions. For this reason it is more meaningful to refer to the band *above* a PBG as the ‘*air*’ band, and the one below the gap as the ‘*dielectric*’ band.

Most of the promising applications of PBG materials depend on the widths and locations of their PBGs. The gap size in a PBG material is determined by the refractive index contrast of the two materials that constitute the 3D structure, and by the filling ratio of the higher-index material [11]. The location of the gap is determined by the lattice constant of the PC. For a face-centred cubic (fcc) lattice, the gap is centred at roughly twice the index modulation wavelength.

The extent of a PBG is characterized by a dimensionless parameter called the *gap–midgap ratio*. It is the ratio $r \equiv \Delta\omega/\omega_0$ of the width $\Delta\omega = \omega_c - \omega_v$ of the gap to the *midgap* frequency ω_0 , where ω_v and ω_c are the lower and upper band edge frequencies of the gap, respectively. This characterization of the extent of a PBG is independent of the scale of the crystal. If the system is compressed (expanded) by a factor s , all the relevant frequencies (ω_v , ω_0 and ω_c) will increase (decrease) by the same factor so that the r stays the same. For example, a gap–midgap ratio of $r = 10\%$, which is readily achievable in present-day PBG materials [12], translates to a gap width of about 0.2 eV at an optical midgap frequency (the energy $(\hbar\omega)$ of an optical transition ($\omega \sim 2\pi \times 10^{15}$ Hz) is of the order $E \sim 2$ eV). By contrast the electronic band gap of germanium at room temperature is 0.67 eV, while that of GaAs is 1.43 eV [13].

For the frequency range spanned by the gap, a PBG material is completely free of propagating electromagnetic modes. Put another way, *the density of propagating photon modes is absolutely zero within a PBG* (see figure 2). The effect is analogous to the existence of gaps in the electron density of states in crystalline solids. By contrast, in free space (or a cavity of infinite volume), the density of photon modes $\rho(\omega)$ varies as ω^2 and exhibits no gap. In a cavity of finite volume, the density of states is substantially modified for frequencies close to the cavity cutoff. Below cutoff, the cavity sustains no modes at all¹, and near and above cutoff, the density of states can be increased relative to the continuum case [14].

The absence of propagating electromagnetic modes, in a refractive medium without dissipation, is due to a synergetic interplay between the microcavity resonances of individual dielectric particles of the PC and the Bragg scattering resonance of the array. One of the conditions for the appearance of a PBG is that the density of dielectric scatterers be chosen such that the microscopic (Mie) scattering resonance of a single unit cell of the PC occurs at the same frequency as the macroscopic (Bragg) resonance of the periodic array [15]. This is a highly restrictive condition in three dimensions. It

¹ A laser will oscillate in a cavity only if the round-trip phase shift $\Delta\phi$ is an integral multiple of 2π or the round-trip optical path length l is an integral number of wavelengths. For a linear bare cavity of length L , we have $\Delta\phi = 2\pi(2L/c)\nu$, and $l = 2L$. The axial resonant modes of the cavity are thus $\nu_m = mc/2L$; and the cavity cutoff is $\nu_c = c/2L$.

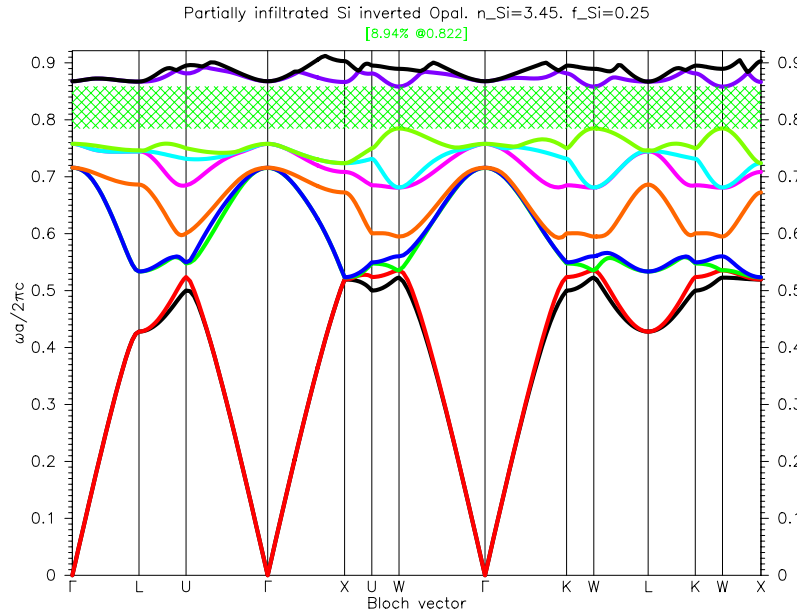


Figure 1. The PBS for the lowest ten bands of a PBG material made of silicon ($n = 3.45$) inverse opal. The filling ratio of silicon is 25%. In units of $\omega a/2\pi c$, where a is the lattice constant, the width of the gap is 0.822 whereas the gap–midgap ratio is 8.94%. (Courtesy of Ovidiu Toader, Department of Physics, University of Toronto.)

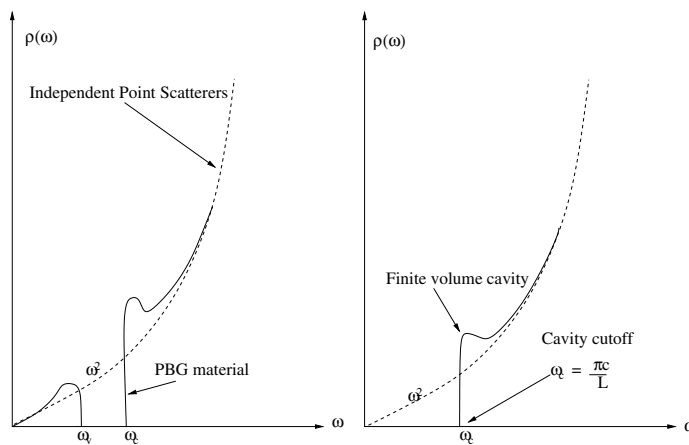


Figure 2. Summary of photon density of states in different cases. For free-space or independent-point scatterers (dotted curve) there is no gap in the photon density of states. For a PBG material (solid curve), there is a complete PBG between the band edge frequencies ω_v and ω_c . A cavity of finite volume sustains no modes below cutoff, whereas near but above cutoff, the density of states can be increased relative to the free-space case.

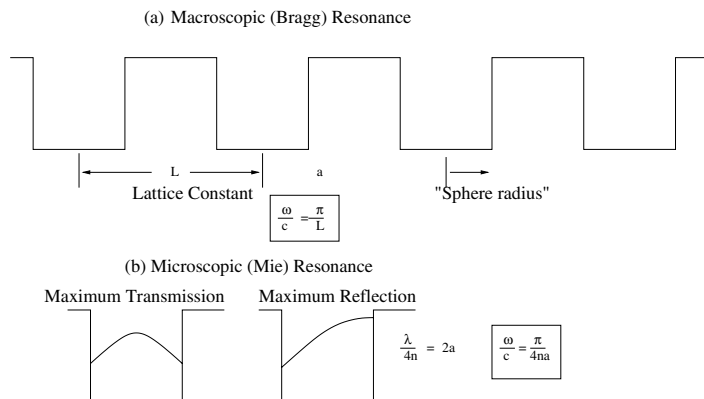


Figure 3. The PBG arises from a synergetic interplay between macroscopic and microscopic resonances. This effect is maximized when the lattice constant L and the sphere radius a are chosen in such a way that the two resonance conditions coincide.

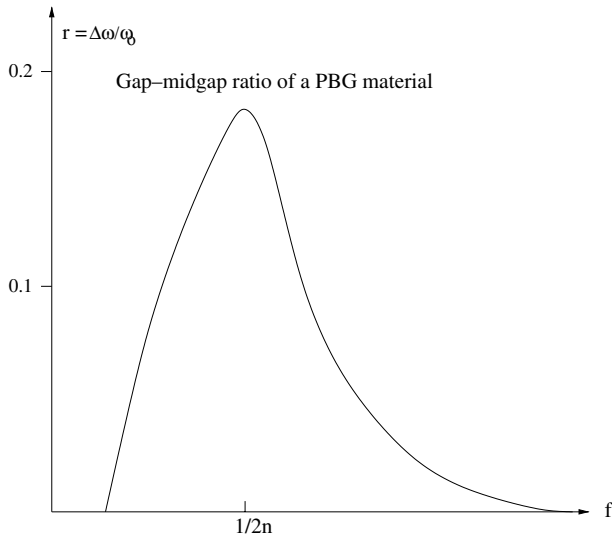


Figure 4. The gap–midgap ratio $r = \Delta\omega/\omega_0$ of a PC as a function of the volume filling fraction f of the solid material. The maximum gap occurs at $1/(2n)$ where n is the refractive index of the solid.

may be illustrated (see figure 3) by a simple example of one-dimensional (1D) wave propagation through a periodic array of square wells of width a and spaced by a distance L . Suppose the refractive index is n inside each well and is unity outside. Then the Bragg scattering condition is given by $\lambda = 2L$ where λ is the vacuum wavelength of light. The analogue of a Mie resonance in one dimension is a maximum in the reflection coefficient from a single well and this occurs when a quarter wavelength fits into the well: $\lambda/(4n) = 2a$. Combining these two conditions yields the optimal volume filling fraction $f \equiv 2a/L = 1/(2n)$. The generic form of the magnitude of the PBG with volume filling fraction f of dielectric material is shown in figure 4.

The vanishing of the density propagating photon modes within a PBG means that, for the frequency range spanned by the gap, *linear propagation of electromagnetic waves is forbidden in any direction* in the PBG material. Thus, light incident on a PBG material with a frequency in the gap region will be backscattered from the material, independent of the angle of incidence. In other words, a PBG material acts as a 4π *steradian stop band* for the frequency range spanned by the PBG. This effect is again analogous to the strict prohibition of propagating electron waves in conventional crystals for a frequency range spanned by an electronic band gap. Strong suppression of transmission, with an associated peak in the reflectivity at the characteristic frequencies, is then an experimental signature of a PBG [3].

Although PBSs are analogous to electronic band structures, there are major differences between them [16]. Electrons have spin $1/2$ and are fermions, and electronic band structure is obtained by solving the appropriate Schrödinger equation. Frequently, the electronic spin is ignored in band structure calculations, and Schrödinger's equation is treated in the scalar wave approximation [13, 17]. On the other hand, photons are spin 1 bosons and it is generally never a good approximation to neglect the vector (polarization) character of the electromagnetic field (that is to treat the two polarizations of the field independently) in band structure

calculations [18, 19]. One consequence of the vector nature of the electromagnetic field is that the band structures for *transverse-electric* (TE) and *transverse-magnetic* (TM) modes can be completely different. In particular, there can be PBGs for one and not for the other [10]. To have a *complete band gap* for all polarizations, a PC should not only have TM and TE band gaps, but these band gaps should also overlap. While there are a number of techniques for band structure calculations of electronic crystals [17], PBS calculations are largely based on the plane-wave expansion of the electromagnetic fields and use of Bloch's theorem to reduce the problem to the solution of a set of linear equations [9, 10, 12].

PBG materials have been attracting considerable attention in the scientific and engineering community due to their potential capabilities which are of immense practical and commercial importance. There have already been a number of books [10], special journal issues [20–22], conference proceedings [23–26], bibliographies [27], and surveys [28–30]. Many applications have been proposed [10, 24, 25, 31], including those which would considerably enhance the performances of quantum electronic devices such as semiconductor lasers, and those which would drastically reduce the sizes of devices such as couplers, beam splitters, filters, cavities and lenses, paving the way for the integration of a large number of highly compact optical components onto an all-optical microchip. In this paper the application of PBG materials for optical memory on an atomic scale is considered.

2.2. Vacuum fluctuations, spontaneous emission and the Lamb shift

The electromagnetic vacuum is characterized by the absence of photons—the mean value of the electric (or magnetic) field at any given point in vacuum is identically zero. However, due to the quantum mechanical nature of the field, the root mean square deviation of the electric (or magnetic) field in vacuum is different from zero. This means, for example, that if we perform one measurement of the field in vacuum, it is possible to find randomly varying non-zero results [32]. We say that the ‘vacuum state’ of photons is subject to *vacuum fluctuations* or *zero-point fluctuations* (ZPFs).

One effect of ZPFs is that, even in the absence of incident photons, they can perturb an excited atom to fall back to a lower energy state by emitting a photon, the energy of the global system being conserved in the process. This is the well known phenomenon of *spontaneous emission* [33–36]. Most of the light around us is ultimately the result of spontaneous emission. The phenomenon goes by various names, depending on the context. The term *luminescence*, for instance, is often used to describe spontaneous emission from atoms or molecules excited by some means other than by heat. If excitation occurs in an electric discharge such as a spark, the term *electroluminescence* is used. If the excited states are produced as a by-product of a chemical reaction, the emission is called *chemiluminescence*, or if this occurs in a living organism, *bioluminescence*, a good example being the luminescence of fireflies. *Photoluminescence* (PL) or *fluorescence* refers to spontaneous emission from an excited state produced by the absorption of light. *Phosphorescence* describes the situation in

which the spontaneous emission persists long after the exciting light is shutoff, and is associated with a meta-stable (long-lived) level [37].

Another effect of ZPFs is to impart to the atomic electrons an erratic motion which slightly modifies the energy of the atomic levels. This modification in the energy levels due to the coupling of the atom to the electromagnetic vacuum is known as the *Lamb shift* and was of utmost importance for the development of QED. To explain the Lamb shift, it was necessary to assume that the electrons in an atom were continually emitting and re-absorbing photons. The emission and absorption processes are virtual in that the associated energies are not subject to energy conservation. (According to the uncertainty relation between energy and time [38], energy is sharply defined only when a measurement is performed over a sufficiently long period of time. It is thus completely consistent with energy conservation that an electron can emit a quantum even without having the necessary energy, as long as the quantum is re-absorbed quickly enough.) Such photons are called *virtual photons* and energy shifts caused by virtual processes are termed *self-energy*.

2.3. Markovian and non-Markovian photon reservoirs

Atom–photon reservoir interaction depends crucially on the behaviour of the density of photon modes of the reservoir, $\rho(\omega)$, near the relevant atomic transition frequency ω_0 . If, near ω_0 , $\rho(\omega)$ is a smoothly varying function of frequency, the atom–reservoir interaction will be characteristically *Markovian* [14, 39]. In such an interaction, the future of the atomic system is entirely determined by the present and not by the past, that is *the atom loses all memory of its past*. Moreover, the spontaneous emission from the atom may be described by the well known Wigner–Weisskopf formalism [40]. In this formalism, spontaneous decay is characteristically *exponential* (with a decay rate γ), the spectrum of the spontaneously emitted photons has a *Lorentzian* shape of half-width γ centred at the radiatively shifted frequency $\omega_0 + \delta\omega_0$ (where ω_0 is the bare atomic transition frequency); and both the γ and $\delta\omega_0$ depend only on the density of modes in the photon reservoir. As an example, atom–photon interaction in free space is Markovian, free space being an infinitely broad featureless photon reservoir.

On the other hand, if, near ω_0 , $\rho(\omega)$ changes on a frequency scale comparable to the spontaneous-emission rate (estimated on the basis of the local photon mode density), the atom–reservoir interaction may be *non-Markovian*. In this case, the Wigner–Weisskopf approximation can no longer be used, and the atomic decay necessarily becomes *non-exponential* and the emission spectrum *non-Lorentzian*.

There are several situations in which the Wigner–Weisskopf approach breaks down [41, 42]. One such situation occurs in a microcavity where the cavity decay rate is much less than the spontaneous emission decay rate of the atomic system so that there will be an oscillatory exchange of the energy between the atomic and photonic degrees of freedom before the spontaneously emitted photon leaks out of the cavity. The atom–photon interaction is then sufficiently strong to split the atomic level into a doublet which, in turn, leads to the splitting of the spontaneous emission spectrum. Such a splitting is

known as the *vacuum Rabi splitting* [43]. The qualitative change of the spectrum from a single Lorentzian peak into a two-peaked structure is a clear indication of the onset of a non-Markovian (non-exponential) decay.

Non-Markovian system–reservoir interaction is also expected to occur in the case when the density of photon modes of the reservoir exhibits a threshold-like behaviour, that is, when $\rho(\omega)$ exhibits a sudden jump or some weaker kind of singular non-analytic behaviour. Such a behaviour occurs, for example, in a waveguide close to its fundamental frequency. If the atomic transition frequency lies close to the threshold, non-exponential (usually algebraic) temporal behaviour dominates the whole decay process, leading to strong modifications in the shape of the spontaneous-emission spectrum. Specifically, the emission spectrum becomes non-Lorentzian (non-Markovian) and may even exhibit additional peaks or valleys [41, 42].

In this paper, we consider a non-Markovian interaction caused by a PC possessing gaps in its photonic density of modes. Quantum electrodynamics in such a reservoir is the subject of the next section.

2.4. Inhibition of single-photon spontaneous emission

Spontaneous emission rate was, at one time, regarded as an intrinsic property of a material over which we have no control [40]. In spectroscopy, it gave rise to the term *natural line width*. However, in 1946 Purcell [44] already suggested that the spontaneous emission rate of radiating dipoles can be tailored by using a cavity to modify the dipole–field coupling and the density of available photon modes. If the modal density in the vicinity of the frequency of interest is greater than that of free space, the spontaneous emission will be enhanced (*Purcell effect*); if it is less, spontaneous emission will be inhibited. This important concept is now well established thanks to the experimental and theoretical development of cavity quantum electrodynamics [26, 45–47].

The challenging application of Purcell’s concept to optoelectronics has been intensively pursued. A number of interesting experimental [45, 48] and theoretical [49] studies with metallic cavities have shown the basic soundness of the idea of engineering atomic spontaneous emission by imposing boundary conditions on the electromagnetic field other than those of free space. A microcavity with perfectly reflecting walls can considerably inhibit or enhance spontaneous emission of atoms placed inside it, depending on whether the cavity is tuned to or detuned from the relevant atomic transition frequency [25, 46, 50]. Spontaneous emission is predicted [48] to be eliminated altogether from an atom placed in a waveguide, provided the atomic transition frequency is below the fundamental frequency of the waveguide.

Although extremely interesting in their own right, metallic cavities are less important in practice, because they do not scale well into optical frequencies. At high frequencies metallic cavities become more and more lossy (because metals are transparent in the ultraviolet [51]). Moreover, simple geometries for the boundaries, such as single- and parallel-plane mirrors do not lead to suppression of spontaneous emission in all directions and, therefore, entail only minor modifications of the spontaneous emission rate [52–54]. On the other hand, PCs made of positive-dielectric-constant

materials (such as glasses and insulators) can be almost free of dissipative losses at any prescribed frequency. Moreover, 3D PBG materials are able to confine optical waves in all three dimensions.

A rough picture of spontaneous emission in a PBG material follows from Fermi's golden rule. Suppose that we have a single two-level atom in an initial excited state written as $|i, 0_k\rangle$, where 0_k indicates the absence of photons of wavevector k . Let the final state of the system consist of the atom in the final state $|f\rangle$, after the emission of a single photon of wavevector k . The final state of the system is then $|f, 1_k\rangle$. In the weak atom–field coupling regime, the atomic spontaneous emission rate is given by Fermi's golden rule [55]:

$$W_{fi} = \frac{2\pi}{\hbar} |\langle f, 1_k | \mathbf{d} \cdot \mathbf{E}(\omega_0, \mathbf{r}_0) | i, 0_k \rangle|^2 \rho(\omega_0). \quad (1)$$

Here \hbar is Planck's constant, \mathbf{d} is the electric dipole moment operator for the atomic transition, $\mathbf{E}(\omega_0, \mathbf{r}_0)$ the electric field operator at the dipole frequency ω_0 and position \mathbf{r}_0 , and $\rho(\omega_0)$ is the density of electromagnetic states at the dipole frequency ω_0 available for the spontaneously emitted photon. Equation (1) is valid, provided that $\rho(\omega)$ is smooth in the vicinity of ω_0 .

Equation (1) shows that the spontaneous emission rate can be enhanced, attenuated, or even suppressed by changing $\rho(\omega_0)$ and/or the matrix element $V_{fi} = \langle f, 1_k | \mathbf{d} \cdot \mathbf{E}(\omega_0, \mathbf{r}_0) | i, 0_k \rangle$. Within a PBG, $\rho(\omega) = 0$ which, in turn, means that $W_{fi} = 0$. In other words, *single-photon spontaneous emission is completely inhibited* within a PBG. This implies that ZPFs, which are present even in vacuum, are absent for frequencies inside a PBG. Thus, within the forbidden frequency band, PBG materials are *emptier* than even the vacuum.

In PBG materials $\rho(\omega)$ and V_{fi} can be engineered to enhance spontaneous emission as well. The existence of PBG leads to other frequency regimes where $\rho(\omega)$ is larger than in free space. Recent experimental investigations of the spontaneous emission properties of organic dye molecules [56–62], semiconductor nanoparticle quantum dots (QDs) [63] and rare-earth ions [64] embedded in PBG materials made of inverted opals have reported pronounced modification of spontaneous emission spectra and noticeable changes in decay kinetics.

2.5. The photon–atom bound state

The absence of propagating modes within a PBG means that, for frequencies within the band gap, there are no *extended* states expressible in Bloch form—as plane waves with purely *real* wavevectors and modified by functions invariant under translation through any lattice vector. Instead, the wavevector is pure imaginary, which causes the modes to decay exponentially in space. Now consider a single excited two-level atom embedded in a PBG material with a transition frequency ω_a to the ground state which lies within the band gap. If this atom drops to the ground state via single-photon spontaneous emission (that is by emitting a single photon of frequency ω_a) the resulting photon state will be exponentially decaying away from the atom, since the frequency ω_a of the emitted photon lies within the classically forbidden energy gap

of the PBG material. In other words, the spontaneously emitted photon will tunnel through the crystal for a short length, called the *localization length*, before being Bragg reflected back to the emitting atom to re-excite it. The result is a strongly coupled eigenstate of the electronic degrees of freedom of the atom and the electromagnetic modes of the dielectric. This is the *photon–atom bound state* first predicted by John and Wang [5, 6] and is the optical analogue of an electronic impurity level bound state in the gap of a semiconductor [13]. When the atomic transition frequency is at midgap ($\omega_a = \omega_0$) the photon tunnelling distance is on the scale of few optical wavelengths, for a gap to midgap ratio of $\Delta\omega/\omega_0 = 5\%$. As ω_a approaches the band edge ω_c , the photon localization length ξ_{loc} grows larger and eventually diverges near ω_c : $\xi_{\text{loc}} \sim c/\sqrt{\omega_c|\omega_c - \omega_a|}$.

In free space, Lamb shift of atomic levels is dominated by the emission and re-absorption of high-energy virtual photons. Within a PBG, this self-dressing is dominated by the real, bound photon. In general this will lead to some anomalous Lamb shift. If an atomic level lies near a photonic band edge, a more striking effect is predicted to occur [65–67]. In this case the atom is resonantly coupled to photons of vanishing group velocity. The resultant self-dressing of the atom by its own localized radiation field is sufficiently strong to split the atomic level into a doublet. One member of the doublet is pulled into the gap and retains a photon bound state, whereas the other member is pushed into the continuum and exhibits resonance fluorescence. In the nearly free photon approximation to the electromagnetic band structure, the splitting of a hydrogenic $2p_{\frac{1}{2}}$ level is predicted to be as large as 10^{-7} – $10^{-6}\hbar\omega_a$ [6]. This is the analogue of the much weaker vacuum Rabi splitting (10–40 MHz) well known for atoms in microcavities [43]. Unlike the well known Mollow level splittings [68] observed when an atom is externally dressed by an intense laser field, the splitting in the present case is solely due to the atom's own localized radiation field and occurs even in the absence of any external driving field. As a result of the interference between the doublets, spontaneous emission from the atom displays an *oscillatory* behaviour which is quite distinct from a simple exponential decay as described by Fermi's golden rule [65–67]. Moreover, the photon–atom bound state leads to a novel *fractionalized* steady-state atomic population in the excited state [65–67]. Again, this is quite different from the free-space case where the steady-state population on an excited level is always zero, since all of the excited level population eventually decays to the ground level.

2.6. Dynamical suppression of spontaneous emission

Atomic level splitting may be effected not only passively through microcavities and PBG materials, but also actively by driving the relevant atomic transition by a resonant (or nearly resonant) laser field [69]. For a two-level atom consisting of the ground state $|0\rangle$ and an excited state $|1\rangle$, with transition frequency ω_a between them, the driving field splits the excited level into two levels having energies close to $\omega_a \pm \Omega/2$, where Ω characterizes the strength of the driving field and is called the *Rabi frequency* of the driving field [70]. This phenomenon of level splitting induced by a driving field is known as *dynamic Stark splitting* or *Autler–Townes splitting* [71] and has been

observed experimentally by several groups [72, 73]. The resulting two lines in the spontaneous emission spectrum of the atom are known as *Autler–Townes doublets*.

If a driven atom resides in a region of space in which the density of photon modes varies appreciably on a frequency scale set by the Rabi frequency of the driving field (such as near a photonic band edge), the interplay between the driving field and the threshold-like behaviour of the photon density of states may lead to dramatic modifications of the spontaneous emission from the atom. These modifications exhibit themselves through changes in the resonance fluorescence spectrum of the atom. The widths, heights, positions, and even shapes of the peaks in the spectrum become dependent on both the intensity of the driving field and the position of the atomic transition frequency relative to the band edge. This effect, brought about by the combined actions of a driving field and a photon density of modes which changes on the scale of the Rabi frequency of the driving field, has been termed in the literature as *dynamical suppression of spontaneous emission* [74].

2.7. Defect modes within a PBG

A pure semiconductor crystal such as silicon has valence and conduction bands separated by a bandgap. However, if this pure semiconductor crystal is *doped* with donor atoms (i.e. if some of the atoms in the crystal are replaced by donor atoms such as arsenic which contribute electrons to the conduction band), a donor level will appear within the forbidden band pushed down from the conduction band. Likewise, if the crystal is doped with acceptor atoms (atoms such as boron which accept electrons from the valence band and contribute holes), an acceptor level will be formed within the forbidden gap pushed up from the valence band [13]. Similarly, a PBG material is a periodic dielectric structure in which photonic states are classified into bands separated by band gaps. The presence of *defects* (local deviations from the ideal crystalline structure) in the crystal may drastically change the optical properties of the PBG material. A defect destroys the perfect 3D translational symmetry of the PBG material and may lead to the formation of a *defect mode* within the band gap region, analogous to donor and acceptor defect modes in a doped semiconductor crystal. If a single-defect mode is introduced into the PBG, the density of states of the system will be zero within the band gap, except for isolated peaks associated with the defect mode (see figure 5).

Defects in a PC may be introduced by adding extra dielectric material where it does not belong or by removing some of the dielectric material that should be there. The first type of defect is called a ‘*dielectric defect*’ and the second an ‘*air defect*’ [10]. Removing a *small* amount of high-index material from one unit cell (air defect) leads to the occurrence of a localized defect mode just above the top of the lower band, analogous to acceptor modes in semiconductors. On the other hand, adding a *small* amount of high-index material to a single unit cell (dielectric defect) causes a single localized state to split off from the upper band edge, analogous to donor modes in semiconductors [75]. This is a general result which applies for one-, two-, and three-dimensional PCs. Whereas in 1D and 2D crystals even arbitrarily small defects can localize modes,

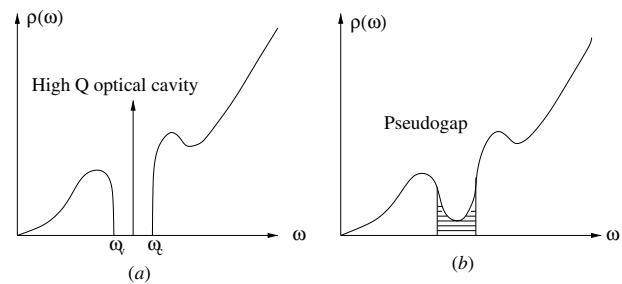


Figure 5. Photon density of states in a PBG material with defects. When a single dielectric defect is created, a localized defect mode appears within the forbidden gap (a). Further disorder in the PC gives rise to a pseudogap (b), instead of a complete gap.

in 3D crystals the defect must be larger than some critical size before its localizing power begins. This is the electromagnetic analogue of the quantum mechanical result that an arbitrarily weak attractive potential can bind a state in one and two dimensions, but not in three dimensions. Significant random perturbation of a PC (by adding or removing a *large* amount of dielectric material, for instance) may wash the gap out and result in a *pseudogap* where the density of states is significantly reduced from that of free space but is not absolutely zero (see figure 5).

The frequency of a defect mode is an *increasing function of the volume of an air defect and a decreasing function of the volume of a dielectric defect* [10, 16, 75, 76]. In other words, for air defect, the larger the volume of material removed, the farther the defect mode is pushed from the lower photonic band edge into the gap (that is, the higher the frequency of the defect mode). Conversely, for a dielectric defect, the larger the volume of high-index material added, the further the defect mode is pushed from the upper photonic band edge into the band gap (that is, the lower the frequency of the defect mode). Thus the frequency of a defect mode can be ‘tuned’ to any desired value within the gap by adding (or removing) the appropriate amount of dielectric material from a unit cell.

Powerful theoretical tools have been developed for modelling electromagnetic fields within PCs [9, 77, 78]. Numerical simulations [10, 79] and experiments [75, 80] have confirmed the confinement of light to local defects in a PBG material. Local defects confine photons to volumes of the order of $(\lambda/2n)^3$, where λ is the photon wavelength and n is the refractive index of the material [31]. Thus, the high-index-contrast systems that are often necessary for achieving PBGs result in strong photon confinement at local defects [10]. Such highly confined optical systems act as *microcavities* of very high quality factor² Q . They can be used to reduce the size and power requirements of integrated optical components, to generate single-mode operation of light-emitting devices, to reduce the lasing threshold of semiconductor lasers, and to allow higher modulation speed of these devices, as discussed in section 2.10.

² The quality factor Q of a cavity is a measure of the optical energy stored in the cavity over the total cycle-averaged power radiated out of the cavity. It is defined as $\omega/\Delta\omega$, where ω is the peak frequency of the resonance and $\Delta\omega$ is the width of the resonance. The sharper the resonance line of the cavity, the smaller the decay rate and the larger the Q .

2.8. Photonic crystals in one, two and three dimensions

PCs are formed by wavelength-scale periodic patterning of dielectric materials in one, two and three dimensions. The unique properties displayed by such crystals depend crucially on their dimensionality [10]. A 1D PC is nothing other than the well known dielectric Bragg mirror consisting of alternating layers with low and high indices of refraction. The term ‘one dimensional’ refers to the fact that the arrangement is periodic only in one direction (chosen here as the z -direction) and homogeneous in the xy -plane. PBGs appear in the direction of periodicity, the z -direction. A mode with frequency in the gap region and propagating in the z -direction (*on-axis* propagation) will be totally reflected from the PC. For *off-axis* propagation, however, there are no band gaps, since the off-axis direction contains no periodic dielectric regions to coherently scatter light and split open a gap. Thus off-axis propagating modes are expected to be oscillatory, with real wavevectors.

In a 1D PC, band gaps always appear for any dielectric contrast. In other words, there is no threshold dielectric contrast for the appearance of a PBG. The smaller the contrast, the smaller the widths of the gaps, but the gaps open up as soon as $n_1/n_2 \neq 1$, where n_1 and n_2 are the refractive indices of the dielectric materials. A defect can be introduced in a 1D PC, for example, by making one of the layers have a slightly different width than the rest. The defect mode is then localized in the z -direction but is extended in the x - and y -directions.

A 2D PC is periodic along two of its axes (say the x - and y -axes) and homogeneous along the third (the z -axis), a typical specimen being an array of dielectric columns arranged on a square or triangular lattice. PBGs appear in the plane of periodicity (the xy -plane). Thus, unlike the multilayer film which reflects light only at normal incidence, a 2D PC can reflect light incident from any direction in the plane of periodicity. Since the structure is homogeneous in the z -direction, modes travelling in that direction do not see a PBG.

In two dimensions, unlike in one dimension, there is a threshold dielectric contrast necessary for the appearance of a PBG. In other words, in a 2D structure, a PBG does not open up just because the structure has a refractive index contrast, but rather requires special design considerations, as discussed below.

A 2D PBG is *defined* as a gap for all EM waves propagating perpendicular to the z -axis of either polarization. A complete band gap, on the other hand, occurs only for 3D structures. Owing to the vector nature of the electromagnetic field, PBSs for TE and TM modes can be completely different. To have a 2D band gap for all polarizations, a photonic crystal should not only have TM and TE band gaps, but these band gaps should also overlap. TM band gaps are favoured in a lattice of isolated high-index regions, as in an array of dielectric columns in air. On the other hand, TE band gaps are favoured in the *inverse* structure, as in an array of air columns (veins) drilled in a dielectric substrate [10]. A structure with dielectric veins is said to be a *connected* structure in that *the high-index regions form a continuous path* instead of discrete spots. Thus, to design a PC that has band gaps for both TM and TE polarizations, one has to somehow reconcile these seemingly contradictory conditions. A triangular lattice of low-index columns (air columns, for instance) inside a high-index medium just does that. If the radius of the columns is

large enough, the spots between columns look like localized regions of high-index material, which are connected (through a narrow squeeze between columns) to adjacent spots.

In a 2D PC, made by perforating a high-index slab with a triangular or hexagonal array of air holes, a defect can be formed by removing an air hole and/or adjusting the diameters of a few neighbouring air holes. A mode (or a set of modes depending on the defect geometry) which is highly localized to the defect region in the xy -plane but extended in the z -direction may be formed. Photons can escape from the defect cavity by tunnelling through the 2D PC, or by leaking out in the z -direction. Removing rows of air holes is one way of creating line defects in a 2D PC. Such line defects can serve as waveguides able to transmit light around sharp corners with very high efficiency.

A 3D PC is a dielectric structure that is periodic along three different axes. Provided that the conditions of sufficiently high dielectric contrast, suitable periodicity, dielectric filling ratio and network connectivity are met, a PBG appears in all directions. Such a 3D PBG material, unlike the 1D and 2D ones, can reflect light incident from any direction. In other words, a 3D PBG material behaves as an *omnidirectional* high reflector.

Even though there are infinitely many possible geometries for a 3D PC, *to date the best structure found to support a full 3D PBG is the diamond lattice* [9, 81]. (Incidentally, the common semiconductors, silicon and germanium, also have diamond symmetry [13].) For a diamond lattice, a complete PBG exists whether one embeds dielectric spheres in air or air spheres in a dielectric medium, as long as the radius is chosen appropriately. The calculated band structure of a diamond lattice of air spheres in silicon ($\epsilon = 11.9$) substrate is shown in figure 6. Between the second and the third bands resides a band gap with a gap–midgap ratio of 27.28%, centred at $\omega_0 = (2\pi c/a)(0.589)$ where a is the lattice constant. The filling ratio of the air spheres is 81% indicating that the air spheres are overlapping (the structure is highly porous). Both the air and the dielectric regions are connected, in the sense that there are no isolated spots of either.

A systematic examination of the PBSs for dielectric sphere and air spheres on a diamond lattice, as a function of refractive index ratio and filling ratio, was made by Ho *et al* [9]. In all cases examined the lattice constant a was kept fixed and the radius r of the spheres was varied to change the filling fraction f . They found that when the refractive index is fixed at 3.6, complete band gaps exist over a wide range of filling ratios for both dielectric spheres and air spheres. (Crystalline silicon and other semiconductors are excellent infra-red optical materials, providing refractive indices ~ 3.5 .) The calculated size of the band gap normalized to the midgap frequency is plotted in figure 7(a) for both cases. For dielectric spheres on a diamond lattice, a maximum gap–midgap ratio of 15.7% was found at $f = 37\%$, whereas for the case of air spheres, the ratio can reach 28.8% at $f = 81\%$. In figure 7(b) the gap–midgap ratio $\Delta\omega/\omega_0$ is plotted as a function of refractive index for a fixed dielectric structure, with $f = 34\%$ for the case of dielectric spheres in air, and $f = 81\%$ for air spheres in a dielectric background. For both cases a complete PBG exists when the refractive index contrast exceeds 2. This is a very important result, because in the optical region there are

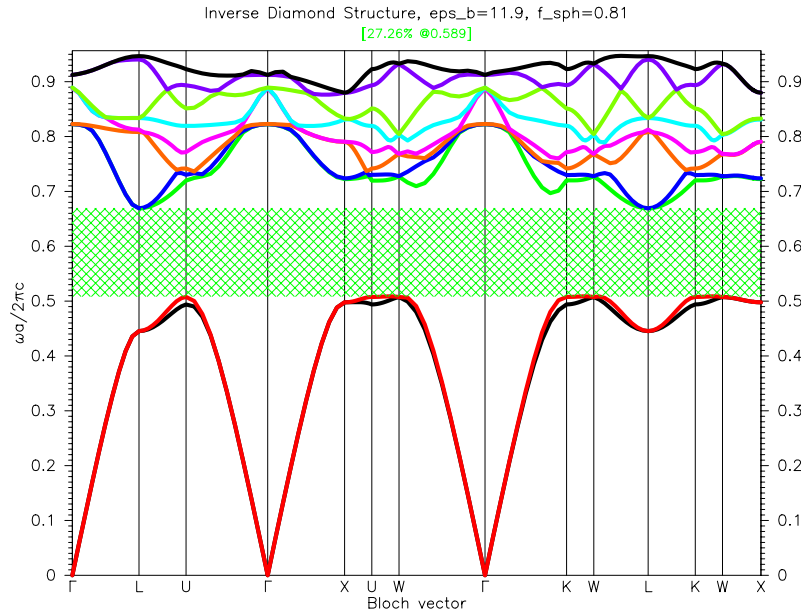


Figure 6. The PBS for the lowest ten bands of a diamond lattice of overlapping air spheres in a high-dielectric ($\epsilon = 11.9$) material. The filling ratio of the air spheres is 81%. The frequency is given in units of c/a where a is the lattice constant and c is the speed of light. A full PBG centred at $\omega_0 = 0.589(2\pi c/a)$ with a gap-midgap ratio of $r = \Delta\omega/\omega_0 = 27.26\%$ appears between the second and third bands.

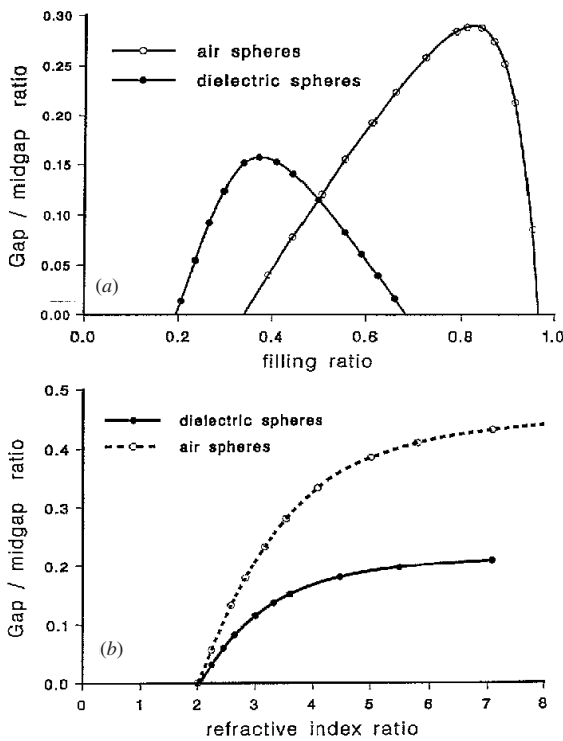


Figure 7. (a) Gap-midgap frequency ratio ($\Delta\omega/\omega_0$) as a function of filling ratio for the case of dielectric spheres in air and air spheres in dielectric. The refractive index of the material is chosen to be 3.6. (b) $\Delta\omega/\omega_0$ as a function of refractive index contrast for a fixed dielectric structure. The dotted curve is for the case of air spheres in dielectric with a filling ratio of 81%, and the solid curve is for dielectric spheres in air with a filling ratio of 34%.

many transparent materials with refractive index above 2. For increasing contrasts the gap-midgap ratio saturates to a value of 21% for the case of solid spheres and to a very large value of 46% for the case of air spheres [9].

In a 3D PBG material, just as in 1D and 2D ones, perturbing a single lattice site may cause the appearance of a single peak in the photon density of states at a frequency that may lie inside the band gap. The width of this peak tends to zero as the crystal size tends to infinity. Since no extended states are allowed in the crystal within the band gap, the mode in the band gap must decay exponentially away from the defect. But in this case the decay occurs in all three dimensions. Thus, in a 3D PBG material, the defect mode is localized at a single point in the crystal. By contrast, one (two)-dimensional PBG materials can only localize light on a plane (line).

2.9. Fabrication of PBG materials

There have been two main challenges in the field of PBG materials. The first was to show that a full 3D PBG could actually exist in some type of dielectric structure. The second was to show that such a PBG material could be created in a microstructure amenable to practical microfabrication. The theoretical calculations of Ho *et al* predicted that periodic dielectric materials with a diamond [9] or diamond-like [82] symmetry would have a full 3D PBG. The gap is centred at roughly twice the index modulation wavelength. Thus, for microwave (MW) control, a PC should be constructed with millimetre dimensions, for infra-red control with micron dimensions, and for optical control with submicron dimensions. Based on the Ho *et al* calculations, the first experimental PBG material was fabricated by Yablonovitch and co-workers [81], with a band gap in the MW region. This structure, sometimes known as the *Yablonovite*, was made by mechanically drilling cylindrical holes through a low loss dielectric block (of refractive index $n \sim 3.6$) so as to create a structure with diamond symmetry.

While demonstrating the existence of a photonic gap, the fabrication of the Yablonovite is a very sophisticated process that cannot be easily reproduced or extended to

optical wavelengths. Several different geometries have been suggested for the fabrication of 3D PBG materials [11, 83, 84], and 3D PBGs have been developed in the near infra-red [85–89]. However, the microfabrication of large-scale PCs with full 3D band gaps at infra-red and optical frequencies is a major challenge. To achieve band gaps for the infra-red and visible spectrum, the periodicity of the crystal should be on the scale of the wavelength of light (about 500 nm), both constituent materials of the crystal should be topologically interconnected [90], and the ratio of their refractive indices should be close to 3.0 [12]. The submicron size periodic lattices required for optical frequency PBG materials limits the use of microlithographic fabrication techniques [87, 91, 92]. Self-organizing systems such as colloidal crystals [93–95], and artificial opals [96–98] provide a template for fabricating these structures.

Colloidal particles have been synthesized from a variety of materials, such as latex and SiO_2 , as monodispersed spheres having precisely controlled diameters (<5% variation in sphere diameter) in the range of from a few nanometres to a few micrometres [93, 95]. A suspension of such colloidal microspheres, with a typical concentration of 10^{10} particles cm^{-3} , can sediment under gravity into a cubic-close-packed structure with relatively large domain size ($\sim 1 \text{ cm}^2$) [99]. These 3D lattices have a crystalline structure similar to that of a natural opal. (A natural *opal* is a close-packed fcc lattice of SiO_2 spheres ($\epsilon = 2.1$) with a filling fraction of $\sim 74\%$.) These artificial opals are solid but present a low mechanical stability which can be greatly improved by a *sintering* process [100]. Sintering or thermal treatment of these artificial opals at elevated temperatures reduces the inter-particle pore volume by changing point contacts between spheres into faceted ones, leading to the formation of a mechanically robust crystal. Thus, colloidal crystal growth produces inherently 3D structures, a significant advantage over lithographic techniques which primarily produce 2D patterns. However, neither colloids nor opals achieve the high refractive index ratios necessary for PBG formation. These requirements are attained by using the colloidal crystals as templates to fabricate *inverse opals* which are close-packed lattices of air balls in a dielectric matrix.

Inverse opals are fabricated in a three-step process. First, a colloidal crystal of latex or silica spheres is self-assembled to generate a high-quality fcc lattice template. Next, the *interstitial regions* (the void spaces among the colloidal particles of an opal-like lattice) are infiltrated with high refractive index material [101–106]. The third step involves the removal of the template material by heat or chemical treatment, immersing the sample in an appropriate chemical etching solution being one example. The end result is a membrane consisting of highly ordered 3D arrays of air balls interconnected by circular ‘windows’ as shown by the computer simulation [107] displayed in figure 8.

A highly porous inverse opal, with a filling ratio of 20–30% of the high dielectric material, is needed for optimum photonic effects [12, 84, 107]. Theoretically, it has been demonstrated [12] that inverted opal structures exhibit near-visible PBGs on the scale of 10% of the midgap frequency. Such structures have been experimentally realized with TiO_2 (refractive index $n = 2.8$) and CdSe [101, 105, 106, 108].

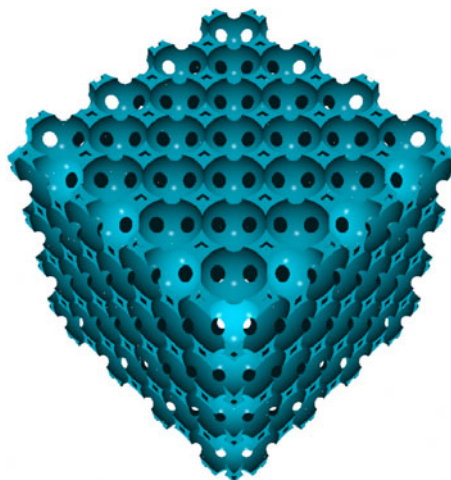


Figure 8. Computer representation of an inverse opal structure. Note the circular ‘windows’ interconnecting the air balls. (Courtesy of Ovidiu Toader, Department of Physics, University of Toronto.)

However, both of these structures are below the required refractive index threshold for PBG formation.

An important application of PBG materials arises for the band gap around $1.5 \mu\text{m}$ —the wavelength most commonly used in fibre optical communication. Such a PBG structure requires colloidal spheres with a diameter of $\sim 870 \text{ nm}$. In this connection, an important step has been achieved [109] through the fabrication of large-scale silicon inverse opals, with a complete 3D PBG centred near $1.5 \mu\text{m}$.

2.10. Applications of PBG materials

The ability to control spontaneous emission using PBG materials will have profound consequences for optoelectronics devices. It can be used to dramatically enhance the light *extraction efficiency* (the ratio of the flux emitted into specified modes to the total emitted flux) of light emitting diodes (LEDs) [110–113], which, in turn, has the effect of reducing the absorption loss and increasing the modulation (response) speed of LEDs. It also has potential applications in *photocatalysis*—a very large field which impacts various areas of chemical synthesis and applications in biochemistry, fuels development, and solar energy conversion [114]. PBG materials made out of a semiconducting material can be used to control the radiative recombination of electrons and holes in the semiconductor [115]. In a semiconductor laser, this would lead to a near-unity quantum efficiency into the lasing mode.

A PBG material can be used as a perfect *dielectric mirror* which reflects light, since light incident on a PBG material with a frequency in the gap region is backscattered from the material, independent of the angle of incidence. This property lends PBG materials to numerous applications, reflectivity being the heart of so many devices such as lasers. For instance, a PBG material might make a very good, narrow-band filter, by reflecting all (and only) frequencies in the gap. PCs, fabricated so as to have a PBG for only one type of polarization, can be used as polarization filters or polarizers which reflect back one type of polarization while allowing another independent polarization to pass through. In these applications dielectric structures have an advantage over metallic mirrors which rely

on the high (frequency dependent) conductivity of metals and suffer dissipative losses at higher frequencies.

The reflective property of PBG materials can also be used to advantage in the design of *planar antennae* [116–118] which, in integrated circuits, play the important role of radiating signals off the chip into free space [119]. By using a 3D PBG as an antenna substrate, it is possible to ensure that all of the antenna power is radiated into air rather than into the substrate, provided that the driving frequency of the antenna lies within the band gap.

The localized mode associated with a defect in an otherwise perfect PBG material can act as a microcavity of very high quality factor Q (see section 2.7). This high- Q defect mode microcavity can be considered for all the applications in which high- Q optical microcavities are used. It can be used to realize the optical engineer's dream of *threshold-less* lasers [120, 121]. It may also be used in experiments to illustrate the quantum properties of light, and atom–photon interactions, such as the Jaynes–Cummings model [122] which describes the interaction of two-level atoms with a single quantized mode of the radiation field.

Just as point defects in a PC are used to trap light, extended defects (such as a line of point defects) can be used to guide light from one location to another. If the frequency of the guided mode lies within the PBG, the mode is forbidden to escape into the crystal, regardless of the shape of the waveguide, because *the confinement mechanism does not have angular dependence*. Thus, a waveguide cut out of a PBG material is capable of guiding light around sharp bends with little or no leakage, even when the radius of curvature of the bend is less than the wavelength of light [123–126]. Moreover, since the light is guided in a hollow waveguide surrounded by omnidirectionally reflecting PBG material, the propagation is primarily through air and will therefore experience substantially lower absorption losses [125]. These properties of a PBG waveguide are in sharp contrast to those of conventional waveguides such as optical fibres. Conventional waveguides are based on the principle of total internal reflection which confines light only of a limited angle. If a waveguide takes a tight curve, the angle of incidence will be too large for total internal reflection to occur so that the light escapes at the corners and is lost. Moreover, in conventional waveguides, light is guided through a dense medium, and, therefore, for long distances, material absorption becomes significant even in low-loss materials. To compensate for losses the fibre is doped with erbium which is used to amplify the signal. This, in turn, limits the bandwidth of the fibre to that of the narrow-band erbium excitation lines [127].

The polarization characteristics of photonic bands in PCs, even those without a PBG, mean that these crystals can possess large birefringence in the long-wavelength limit. The birefringence or *double refraction*—defined as the difference in the effective refractive indices seen by the electric fields associated with two orthogonal polarizations—of 2D PCs (composed of a triangular lattice of air cylinders in silicon) was recently investigated both theoretically and experimentally by van Driel and co-workers [129]. The measured birefringence (for an electric field polarized parallel and perpendicular to the cylinder axis) reaches a maximum value of 0.366 near the first photonic band edge at $\lambda \approx 6.52 \mu\text{m}$. In

contrast, at wavelength 589.3 nm, the birefringence of quartz (crystalline SiO_2) is 0.0091 whereas that of calcite (CaCO_3) is 0.172 [130]. Photonic crystal birefringence could be used in a wide variety of photonic devices, including wave-plates, polarization rotators, optical isolators and beam splitters.

2D PBG materials, in contrast to 3D microstructures, are much more amenable to controlled fabrication owing to mature nanofabrication technology. As a consequence, 2D PCs have been more thoroughly investigated than their 3D counterparts [131–134]. Although they do not provide 3D light guiding or confinement, 2D structures could already bring a sizable part of the advantages expected from 3D structures. The enhancement and suppression of spontaneous emission in thin-film 2D PCs at room temperature have been investigated [110]. The optical and confinement properties of 2D PCs have been studied [135–137]. Triangular and hexagonal 2D defect mode PBG microcavities showing a Q -factor of at least 900 have already been demonstrated [138, 139]. One can think of such cavity modes as filters that select only the resonant frequency [140]. The use of 2D PBG materials to localize light to a single defect and thereby form a high- Q nanocavity laser with a modal volume of less than $0.03 \mu\text{m}^3$, constituting the smallest laser ever made, is reported [80, 141]. The performance and guiding properties of waveguides fabricated in 2D PBG materials are investigated [126, 142].

The potential applications of PBG materials for passive devices such as filters, waveguides, antenna substrates and reflectors have already been discussed. The possibility of dynamically controlling the spectral and spatial properties of PBG materials by active elements is expected to open new application prospects [143]. The latest development in this direction involves the use of liquid crystals as active elements to tune PBG materials made out of inverted opals. This novel concept of tunability was first proposed by Busch and John [144, 145] who studied the effects of partially infiltrating (coating) the spherical voids of an inverted opal made out of silicon with a low-index nematic liquid crystal [146]. They showed that the width of a band gap can be adjusted or the band gap can be eliminated altogether by an applied electric field which changes the orientation of the nematic director. In this manner, the PBG can be either globally altered or locally addressed by applied voltages. The timescale of electro-optic modulation of the PBG may be on the scale of microseconds to milliseconds depending on the response time of the nematic.

The recent spectacular technological advances in the synthesis of 3D PBG materials at infra-red and optical frequencies have made it possible to envision a PBG material as a platform for integrating an all-optical circuitry. An array of densely packed PC microcavities [138], waveguides [126], prisms [128], switches [147] and light sources [80, 141] can be integrated on a very small area of a PC by engineering the appropriate defects inside the crystal, paving the way for all-optical computing.

3. Coherent control of spontaneous emission near a photonic band edge: the leading approximation

Recently, quantum interference and coherence in a multilevel atomic system has attracted a lot of attention, because it leads

to such interesting effects as the enhancement of the index of refraction with greatly reduced absorption, electromagnetically induced transparency, and optical amplification without population inversion [14]. The coherent control of molecular chemical reactions [148] is an emerging frontier in chemical physics [149]. Using the coherence properties of an external laser field driven interaction, radiatively controlled chemical pathways can be enhanced or retarded by quantum mechanical interference effects. Selective photo-dissociation of molecules mediated by the interference between two two-photon excitation processes has been reported [150]. Coherent control of current in a semiconductor has also been demonstrated [151]. In view of these achievements, it is of great interest to consider the combined effects of coherent control by means of external laser fields and the coherent localization effects facilitated by a PBG.

In this section we investigate the coherent control of spontaneous emission for a three-level atom located within a perfect PBG structure. The model is considered in what we call the leading approximation whereby a number of spontaneous emission effects and non-radiative interactions are neglected. This renders the problem amenable to analytical solution. Considerations beyond the leading approximation are deferred to section 4.

3.1. Description of the model system

The physical system we consider consists of a single three-level atom placed inside a PBG material which is then driven by a laser field, see figure 9. We let $|0\rangle$ denote the ground level of the atom; and $|1\rangle$ and $|2\rangle$ the two excited levels with orthonormality conditions $\langle i|j\rangle = \delta_{ij}$, where δ_{ij} is the Kronecker delta function. We designate the energy of an atomic level $|i\rangle$ by $\hbar\omega_i$ and the frequency separation between levels $|i\rangle$ and $|j\rangle$ by $\omega_{ij} = \omega_i - \omega_j$. The transition between levels can be described using the atomic operators $\sigma_{ij} = |i\rangle\langle j|$, with the property $\sigma_{ij}|k\rangle = \delta_{jk}|i\rangle$, from which the commutation relation

$$[\sigma_{ij}, \sigma_{ik}] = \delta_{jl}\sigma_{ik} - \delta_{ik}\sigma_{lj} \quad (2)$$

can readily be obtained.

The upper atomic level $|2\rangle$ is dipole coupled to the ground level $|0\rangle$ by radiation modes (photon reservoir) in a three-dimensional periodic dielectric structure. The transition frequency ω_{20} is assumed to be near the edge of the gap in the density of the reservoir photon modes. Each mode of the photon reservoir is characterized by a wavevector \mathbf{k} and a polarization index $\lambda (= 1, 2)$ and can be treated as a quantum oscillator with frequency $\omega_{\mathbf{k}}$. Transitions between photon occupation number states $|n_{\mathbf{k}\lambda}\rangle$ are described by the radiation field annihilation ($a_{\mathbf{k}\lambda}$) and creation ($a_{\mathbf{k}\lambda}^\dagger$) operators satisfying the standard Bose algebra

$$[a_{\mathbf{k}\lambda}, a_{\mathbf{k}'\lambda'}^\dagger] = \delta_{\mathbf{k}\mathbf{k}'}\delta_{\lambda\lambda'}. \quad (3)$$

We assume that atomic operators σ_{ij} commute with the field operators $a_{\mathbf{k}\lambda}$ and $a_{\mathbf{k}\lambda}^\dagger$. The transition $|2\rangle \rightarrow |1\rangle$ between the two upper levels is driven by a resonant control laser field.

We assume that spontaneous emission on the transitions $|2\rangle \rightarrow |1\rangle$ and $|1\rangle \rightarrow |0\rangle$ is inhibited either by symmetry considerations or by the presence of the PBG. This assumption

constitutes the *leading approximation* to our model system. This approximation describes the essential physics contained in the model system. In section 4, we consider corrections to this leading approximation brought about by the inclusion of the spontaneous emission channels $|2\rangle \rightarrow |1\rangle$ and $|1\rangle \rightarrow |0\rangle$, and other non-radiative interactions.

First we consider a three-level atom in the so-called V configuration (figure 9(a)). In such a configuration, the upper levels $|2\rangle$ and $|1\rangle$ are of the same symmetry so that single-photon spontaneous emission $|2\rangle \rightarrow |1\rangle$ is not dipole allowed. Now if we assume that the transition frequency ω_{10} is deep inside the gap, then single-photon spontaneous emission for the transition $|1\rangle \rightarrow |0\rangle$ will lead to a photon-atom bound state [65, 152]. Thus, *for a three-level atom in the V configuration, the leading approximation is satisfied if ω_{10} lies deep inside the gap*. In a V system, the external control laser field of frequency ω_L which couples levels $|2\rangle$ and $|1\rangle$ drives a two-photon transition ($2\omega_L = \omega_{21}$), since the levels are of the same symmetry. From a practical point of view, we want the transition frequency ω_{21} to be as large as possible, as it may be difficult to generate MW fields of sufficient amplitude to drive the required two-photon transition. However, the magnitude of ω_{21} is restricted by the width of the PBG. For a gap centred at frequency ω_0 and with a gap to midgap ratio of $r \equiv \Delta\omega/\omega_0$, conditions that ω_{20} be near the edge of the gap and that ω_{10} be deep inside the gap require that $\omega_{21} = \omega_{20} - \omega_{10} < r\omega_0$. Thus, to make ω_{21} large we need a gap with as high a central frequency as possible and as large a width as possible. For a gap centred at an optical frequency $\omega_0 \sim 10^{16}$ Hz and with a gap to midgap ratio of 10%, the frequency separation ω_{21} between levels $|2\rangle$ and $|1\rangle$ must be approximately 5×10^{14} Hz.

Another means of overcoming the above practical limitation associated with the V system is to couple levels $|1\rangle$ and $|2\rangle$ indirectly by way of a transition to a higher level $|3\rangle$ which lies far above level $|2\rangle$. This will allow us to both strongly couple levels $|1\rangle$ and $|2\rangle$ and use a narrow band gap, even when the transition frequency ω_{21} lies in the near or far infra-red. Level $|3\rangle$ is dipole coupled to level $|1\rangle$ (and hence to level $|2\rangle$, since they are of the same symmetry) and the transitions ω_{31} and ω_{32} are both in the visible and both lie outside the gap, as shown in figure 9(c). The transition ω_{31} is then pumped by a resonant laser $\omega_p = \omega_{31}$ followed by a stimulated emission into level $|2\rangle$ using a laser which couples levels $|3\rangle$ and $|2\rangle$ [153].

Next we consider a three-level system in the Λ configuration (figure 9(b)). In such a configuration, levels $|1\rangle$ and $|0\rangle$ have the same symmetry and there is no dipole-allowed single-photon spontaneous emission between these levels. Now, if we further assume that the transition frequency ω_{21} is far inside the gap, the dipole-allowed transition $|2\rangle \rightarrow |1\rangle$ will create a photon-atom bound state whose radiative lifetime is given by the two-photon spontaneous emission time for the $|1\rangle \rightarrow |0\rangle$ transition. Thus, *for a three-level atom in the Λ configuration, the leading approximation is satisfied if ω_{21} lies deep inside the gap*. To reconcile the conditions that ω_{20} is near the band edge and that ω_{21} is deep in the gap, we require that $\omega_{10} = \omega_{20} - \omega_{21} \leq r\omega_0$. Given the practical fact that $r \leq 0.1$, it follows that levels $|1\rangle$ and $|0\rangle$ should be close to each other but both far from level

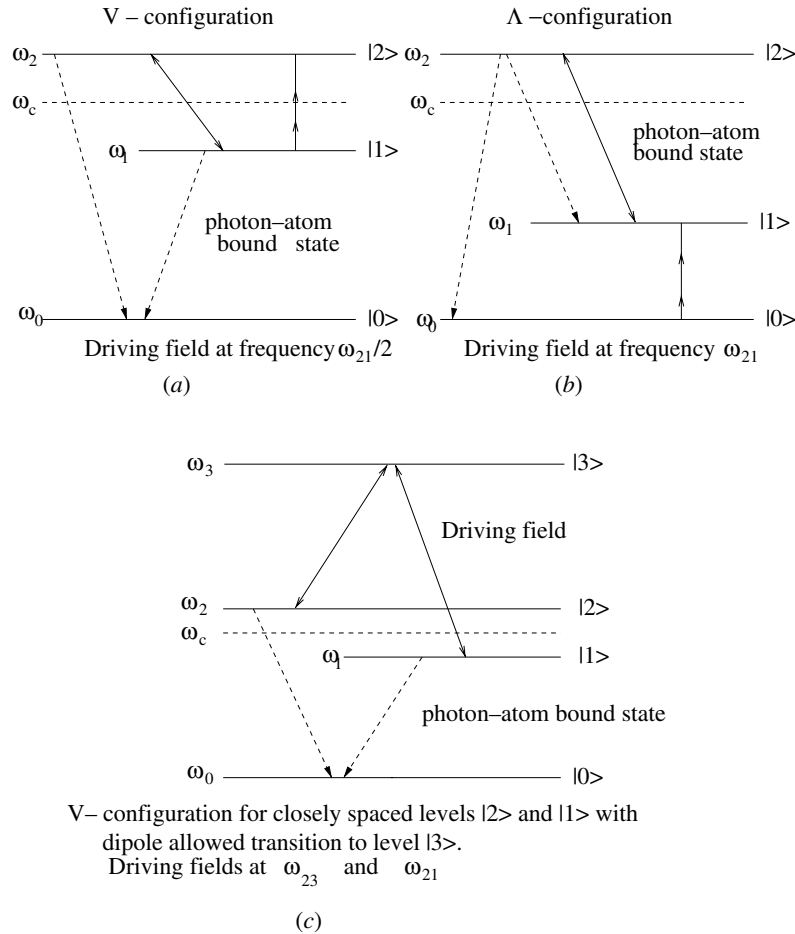


Figure 9. Schematic representations of a driven three-level system (a) in the V configuration and (b) in the Λ configuration. The transition frequency ω_{20} is near the band edge frequency ω_c of a PBG. Lines with arrows at both ends denote the control laser field of Rabi frequency Ω driving the transition $|2\rangle \leftrightarrow |1\rangle$. Double arrowed lines denote two-photon transitions. Dashed lines denote dipole-allowed transitions. In the V configuration levels $|2\rangle$ and $|1\rangle$ are of the same symmetry and ω_{10} is deep inside the PBG so that there are no single-photon spontaneous emissions on the transitions $|2\rangle \rightarrow |1\rangle$ and $|1\rangle \rightarrow |0\rangle$. Similarly in the Λ configuration levels $|1\rangle$ and $|0\rangle$ are of the same symmetry and ω_{21} is deep inside the PBG so that there are no single-photon spontaneous emissions on the transitions $|2\rangle \rightarrow |1\rangle$ and $|1\rangle \rightarrow |0\rangle$. The control laser field drives a two-photon transition ($2\omega_L = \omega_{21}$) in the V configuration and a single-photon transition ($\omega_L = \omega_{21}$) in the Λ configuration. Figure 1(c) shows indirect coupling of levels $|1\rangle$ and $|2\rangle$ in a V system via another level $|3\rangle$. Such a scheme will allow us to strongly couple levels $|1\rangle$ and $|2\rangle$ even when the transition ω_{21} lies in the infra-red or far infra-red.

$|2\rangle$, as shown in figure 9(b). This, in turn, will reduce the decay rate of the photon-atom bound state due to two-photon spontaneous emission from $|1\rangle \rightarrow |0\rangle$. However, since ω_{21} is within the gap, the control laser driving the single-photon transition $|2\rangle \rightarrow |1\rangle$ must be injected by means of engineered or naturally occurring defect or waveguide modes within the band gap material.

3.2. Model Hamiltonian and equations of motion

The Hamiltonian describing the leading approximation to our model system can be written as (see appendix A)

$$H = H_A + H_R + H_{AR} + H_{AL}, \quad (4)$$

where

$$H_A = \sum_{i=0}^2 \hbar \omega_i \sigma_{ii}, \quad (5a)$$

$$H_R = \sum_{\lambda=1}^2 \sum_{\mathbf{k}} \hbar \omega_{\mathbf{k}} a_{\mathbf{k}\lambda}^\dagger a_{\mathbf{k}\lambda}, \quad (5b)$$

$$H_{AR} = i\hbar \sum_{\lambda=1}^2 \sum_{\mathbf{k}} g_{\mathbf{k}\lambda} (a_{\mathbf{k}\lambda}^\dagger \sigma_{02} - \sigma_{20} a_{\mathbf{k}\lambda}). \quad (5c)$$

Here H_A represents the Hamiltonian of the bare atom whereas H_R stands for the Hamiltonian of the photon reservoir (neglecting the zero-point energy). The Hamiltonian H_{AR} describes interaction between the atomic transition $|2\rangle \rightarrow |0\rangle$ and the photon reservoir. Here $g_{\mathbf{k}\lambda}$ is the frequency-dependent coupling constant (assumed to be real) between the atomic transition $|2\rangle \rightarrow |0\rangle$ and the mode $\{\mathbf{k}\lambda\}$ of the radiation field:

$$g_{\mathbf{k}\lambda} = \frac{\omega_{20} d_{20}}{\hbar} \left(\frac{\hbar}{2\epsilon_0 \omega_{\mathbf{k}} V} \right)^{1/2} \hat{\mathbf{e}}_{\mathbf{k}\lambda} \cdot \hat{\mathbf{d}}_{20}. \quad (6)$$

In this expression d_{20} and $\hat{\mathbf{d}}_{20}$ are the magnitude and unit vector of the atomic dipole moment \mathbf{d}_{20} for the transition $|2\rangle \rightarrow |0\rangle$, V is the sample volume, $\hat{\mathbf{e}}_{\mathbf{k}\lambda}$ are the two transverse (polarization) unit vectors and ϵ_0 is the Coulomb constant. The coupling constant $g_{\mathbf{k}\lambda}$ fully characterizes the density of modes in the photon reservoir.

The interaction Hamiltonian H_{AR} is written in the electric dipole approximation [70]. It is also written in the rotating wave approximation (RWA) [70] in which virtual processes of excitation (de-excitation) of the atom with simultaneous creation (annihilation) of a photon (that is, terms of the form $a_{k\lambda}^\dagger \sigma_{20}$ and $a_{k\lambda} \sigma_{02}$) are neglected.

In equation (4), the Hamiltonian H_{AL} represents the interaction between the atom and the coherent monochromatic laser field driving the transition $|2\rangle \leftrightarrow |1\rangle$. We assume that *the driving field is sufficiently strong that it can be treated classically*. In the Λ configuration, levels $|2\rangle$ and $|1\rangle$ are of opposite symmetry, and, therefore, the transition $|2\rangle \rightarrow |1\rangle$ is a dipole-allowed transition. Thus, the external control laser field which couples levels $|2\rangle$ and $|1\rangle$ drives a one-photon transition ($\omega_L = \omega_{21}$). In this case H_{AL} can be written as [154]

$$H_{AL}^\Lambda = i\hbar\Omega_\Lambda [e^{i(\omega_L t + \phi)} \sigma_{12} - e^{-i(\omega_L t + \phi)} \sigma_{21}], \quad (7)$$

where ω_L , Ω_Λ and ϕ represent the angular frequency, the Rabi frequency and the phase of the driving laser.

The *Rabi frequency* [70] is a measure of the strength of the interaction between the driving field and the atomic transition $|2\rangle \rightarrow |1\rangle$. For a dipole-allowed transition, such as $|2\rangle \rightarrow |1\rangle$ in the Λ system, the Rabi frequency of the driving field is proportional to the product of the atomic dipole moment d_{21} and the amplitude $E_0 = |\mathbf{E}_0|$ of the sinusoidal optical field:

$$\hbar\Omega_\Lambda = d_{21}E_0. \quad (8)$$

On the other hand, in the V configuration, the upper levels $|2\rangle$ and $|1\rangle$ are of the same symmetry and, therefore, the transition $|2\rangle \rightarrow |1\rangle$ is not dipole allowed. Thus, the external control laser field of frequency ω_L which couples levels $|2\rangle$ and $|1\rangle$ drives a two-photon transition ($2\omega_L = \omega_{21}$). In this case, the interaction Hamiltonian H_{AL} will be of the form

$$H_{AL}^V = \hbar\Omega_V [e^{i(2\omega_L t + \phi')} \sigma_{12} - e^{-i(2\omega_L t + \phi')} \sigma_{21}], \quad (9)$$

where the Rabi frequency Ω_V is now obtained from second-order perturbation theory [155]

$$\hbar\Omega_V = \sum_I \frac{(d_{2I} \cdot \mathbf{E}_0)(d_{I1} \cdot \mathbf{E}_0)}{\hbar(\omega_L - \omega_{I1})}. \quad (10)$$

Here the summation is over all intermediate states $|I\rangle$ of the atom.

For the sake of notational simplicity (not to write almost identical equations separately for the Λ and V systems) we write the interaction Hamiltonian H_{AL} in both the Λ and V cases as

$$H_{AL} = \hbar\Omega [e^{i(\omega_c t + \phi_c)} \sigma_{12} - e^{-i(\omega_c t + \phi_c)} \sigma_{21}], \quad (11)$$

assuming that what we mean by Ω , ω_c and ϕ_c can be understood from the context. For ω_{j0} in the optical regime, we can safely assume that

$$\Omega \ll \omega_{j0}. \quad (12)$$

Laser intensities required to make Ω comparable to an optical frequency would cause dielectric breakdown and are many orders of magnitude larger than that used in any resonance experiment [70].

In the framework of perturbation theory, which is usually employed in quantum electrodynamics, the Hamiltonian

$$H_0 = H_A + H_R \quad (13)$$

is regarded as the Hamiltonian of the unperturbed system whereas

$$H_I = H_{AR} + H_{AL} \quad (14)$$

describes the perturbation. In this paper we employ the *Schrödinger picture* of quantum mechanics [39] where observables are described by time-independent operators, the basis vectors of the appropriate Hilbert space are stationary (like the fixed coordinate system in ordinary geometry), and state vectors move continuously in this space according to the time-dependent Schrödinger equation

$$i\frac{\partial}{\partial t}|\Psi(t)\rangle = H|\Psi(t)\rangle, \quad (15)$$

where H is the Hamiltonian of the system.

The stationary states (eigenstates) of the unperturbed Hamiltonian H_0 of equation (5b) are listed below together with their corresponding eigenvalues:

$$|2, \{0\}\rangle, \hbar\omega_2, \quad |1, \{0\}\rangle, \hbar\omega_1, \quad |0, \{1_{k\lambda}\}\rangle, \hbar(\omega_0 + \omega_k). \quad (16)$$

Here the state vector $|j, \{0\}\rangle \equiv |j\rangle|0\rangle$ represents the atom in the upper states $|j\rangle$ and the vacuum electromagnetic field (that is, no photons present in the system). On the other hand, the state vector $|0, \{1_{k\lambda}\}\rangle$ represents the atom in the ground state $|0\rangle$ and a single photon in a mode $\{k\lambda\}$. The state $|j, \{0\}\rangle$ is a direct product of the atomic state $|j\rangle$ and the radiation state $|\{0\}\rangle$, since the atomic operators are assumed to commute with the radiation field operators. Similarly, $|0, \{1_{k\lambda}\}\rangle$ is a direct product of $|0\rangle$ and $|\{1_{k\lambda}\}\rangle$. The vectors $|1, \{1_{k\lambda}\}\rangle$ are assumed to be inaccessible in the V system, since there is no single-photon spontaneous emission on the transition $|2\rangle \rightarrow |1\rangle$. Two-photon spontaneous emission is considered to be negligible compared to the two-photon stimulated emission from $|2\rangle$ to $|1\rangle$, induced by the classical control laser field. This latter effect is described by the classical Rabi field (two-photon transition) amplitude $\hbar\Omega_V e^{i(2\omega_L t + \phi_c)}$. Similarly, in the Λ system, *single-photon spontaneous emission from $|2\rangle$ to $|1\rangle$, although allowed in the control laser mode, is assumed to be negligible compared to stimulated emission driven by the control laser field*. (Single-photon spontaneous emission is *not* allowed into the other modes having frequency ω_{21} because ω_{21} is deep within the gap.) For the Λ -system, the effects of stimulated emission are described by the classical Rabi field (one-photon transition) amplitude $\hbar\Omega_\Lambda e^{i(\omega_L t + \phi_c)}$.

We assume the following initial configuration for the model system. At $t = 0$, the radiation-field reservoir is initially in the vacuum state (no photon in the system), and the atom is prepared in a coherent superposition of its two upper levels $|2\rangle$ and $|1\rangle$ in the form

$$|\Psi(0)\rangle = \cos\theta|2, \{0\}\rangle + e^{i\phi_p} \sin\theta|1, \{0\}\rangle. \quad (17)$$

The parameter θ measures the degree of superposition of levels $|2\rangle$ and $|1\rangle$. A value of $\theta = 0$ means that the atom is initially prepared on the upper level $|2\rangle$, whereas $\theta = \pi/4$ means that the atom is initially prepared as an equal superposition of the

upper levels $|1\rangle$ and $|2\rangle$. The factor $e^{i\phi_p}$ gives the *relative* phase between the expansion coefficients of $|2\rangle$ and $|1\rangle$, and plays a significant role in physical predictions [156]. The coherent superposition state (17) can be prepared by an ultra-short pumping laser pulse of appropriate pulse area [70].

As a result of the perturbation H_I applied at time $t = 0$, the initial state $|\Psi(0)\rangle$ evolves in time according to Schrödinger equation (15). At any time t , the state vector of the system can be written as a linear combination of the eigenstates (16) of the unperturbed Hamiltonian H_0 . Accordingly, we write

$$|\Psi(t)\rangle = c_2(t)e^{-i\omega_2 t}|2, \{0\}\rangle + c_1(t)e^{-i\omega_1 t}|1, \{0\}\rangle + \sum_{k\lambda} c_{k\lambda}(t)e^{-i(\omega_k + \omega_0)t}|0, \{k\lambda\}\rangle, \quad (18)$$

where the time dependences of the amplitudes due H_0 are explicitly factored out in the form of exponentials. Comparing equations (18) and (17), we obtain

$$c_2(0) = \cos \theta, \quad c_1(0) = e^{i\phi_p} \sin \theta, \quad c_{k\lambda}(0) = 0, \quad (19)$$

as the initial values for the amplitudes $c_{1,2}(t)$ and $c_{k\lambda}(t)$ corresponding to the initial state (17).

The function $c_j(t)$ gives the probability amplitude to find the atom in the excited state $|j\rangle$ and the photon reservoir in the vacuum state. On the other hand, $c_{k\lambda}(t)$ gives the probability amplitude to find the atom on the ground state $|0\rangle$ and a single photon of wavevector \mathbf{k} and polarization λ in the photon reservoir. Thus, the probability of finding the atom in the excited level $|j\rangle$, more commonly known as the *population* of level $|j\rangle$, is given by

$$n_j(t) = |c_j(t)|^2, \quad (j = 1, 2). \quad (20)$$

The *steady-state population* of the atomic level $|j\rangle$ is then

$$n_{js} = \lim_{t \rightarrow \infty} n_j(t), \quad (j = 1, 2). \quad (21)$$

Using equation (19) in (20), we obtain

$$n_1(0) = \sin^2 \theta, \quad n_2(0) = \cos^2 \theta \quad (22)$$

for the initial populations of the upper levels $|1\rangle$ and $|2\rangle$. An important quantity in applications such as quantum computing is the cross-term

$$n_c(t) \equiv c_2(t)c_1^*(t). \quad (23)$$

This term measures the interference between the atomic amplitudes $c_1(t)$ and $c_2(t)$ and is known as the *coherence*. Its steady-state value is

$$n_{cs} = \lim_{t \rightarrow \infty} n_c(t). \quad (24)$$

Using equations (4) and (18) in (15), and projecting the result onto the eigenstates $|0, \{k\lambda\}\rangle$, $|1, \{0\}\rangle$ and $|2, \{0\}\rangle$ of H_0 , respectively, we obtain the following (infinite) set of coupled equations for the amplitudes $c_j(t)$ and $c_{k\lambda}(t)$:

$$\dot{c}_{k\lambda}(t) = g_{k\lambda}c_2(t)e^{i\mu_k t}, \quad (25a)$$

$$\dot{c}_1(t) = \Omega e^{i\phi_c} c_2(t), \quad (25b)$$

$$\dot{c}_2(t) = -\Omega e^{-i\phi_c} c_1(t) - \sum_{k\lambda} g_{k\lambda} c_{k\lambda}(t) e^{-i\mu_k t}. \quad (25c)$$

Here the dot over an amplitude signifies the total time derivative and

$$\mu_k = \omega_k - \omega_{20} \quad (26)$$

represents the detuning of the radiation mode frequency ω_k from the atomic transition frequency ω_{20} . Equation (25a) can be integrated (in time), using the initial condition (19), to give

$$c_{k\lambda}(t) = g_{k\lambda} \int_0^t c_2(t') e^{i\mu_k t'} dt'. \quad (27)$$

Substituting this expression for $c_{k\lambda}(t)$ in equation (25c) yields the following two coupled integro-differential equations:

$$\dot{c}_1(t) = \Omega e^{i\phi_c} c_2(t), \quad (28a)$$

$$\dot{c}_2(t) = -\Omega e^{-i\phi_c} c_1(t) - \int_0^t G(t-t') c_2(t') dt', \quad (28b)$$

where

$$G(t-t') = \sum_{k\lambda} g_{k\lambda}^2 e^{-i\mu_{k\lambda}(t-t')} \quad (29)$$

is the delay *Green function* of the problem. In writing down equation (28a) and (28b) we have exchanged the order of summation over $k\lambda$ and integration over time. The resulting Green function depends very strongly on the photon density of states of the relevant photon reservoir. In essence, $G(t-t')$ is a measure of the photon reservoir's memory of its previous state on the timescale for the evolution of the atomic system, hence the alternative name *memory kernel*.

The main objective of this section is to solve the coupled equations (28a) and (28b) for the amplitudes $c_j(t)$ in a given photon reservoir. These amplitudes can then be used to evaluate the populations and coherences of the atomic levels. The integral on the right-hand side of equation (28b) is a convolution integral which suggests solution by Laplace transformation [157]. Upon taking the Laplace transforms of equations (28a) and (28b) and using the initial condition (19), we find that

$$\tilde{c}_2(s) = \frac{s \cos \theta - \Omega e^{i\phi} \sin \theta}{s^2 + s\tilde{G}(s) + \Omega^2}, \quad (30a)$$

$$\tilde{c}_1(s) = \frac{e^{i\phi_p} \sin \theta [s + \tilde{G}(s)] + \Omega e^{i\phi_c} \cos \theta}{s^2 + s\tilde{G}(s) + \Omega^2}, \quad (30b)$$

where $\tilde{c}_j(s)$ and $\tilde{G}(s)$ are the Laplace transforms of $c_j(t)$ and $G(t)$, respectively, and

$$\phi = \phi_p - \phi_c \quad (31)$$

is determined by the relative phase between the control and pump lasers.

For a given dispersion relation ω_k , we can calculate $G(t-t')$ from equation (29) which, in turn, can be used to calculate $\tilde{G}(s)$. This $\tilde{G}(s)$ can then be used in equations (30a) and (30b) and the resulting expressions inverted to find analytical expressions for the amplitudes $c_j(t)$.

3.3. Model system in vacuum

First we consider the case of a three-level atom in free space. Besides being an interesting case in its own right [14], the free-space case will be useful to compare and interpret the results of the PBG case which is discussed in later sections. The leading approximation described by the Hamiltonian (4) can be valid in free space if $\gamma_{10} \ll \gamma_{20}$ in a V system (so that spontaneous emission on the transition $|1\rangle \rightarrow |0\rangle$ can be ignored), or if $\gamma_{21} \ll \gamma_{20}$ in a Λ system (so that spontaneous emission on the transition $|2\rangle \rightarrow |1\rangle$ can be ignored).

The electromagnetic vacuum is characterized by the dispersion relation

$$\omega(k) = ck. \quad (32)$$

For such a dispersion relation the Green function (29) takes the form

$$G(t - t') = \gamma_{20} \delta(t - t'), \quad (33)$$

where

$$\gamma_{ij} = \frac{1}{4\pi\epsilon_0} \frac{4\omega_{ij}^3 d_{ij}^2}{6\hbar c^3} \quad (34)$$

is half the spontaneous emission rate Γ_{ij} for the transition $|i\rangle \rightarrow |j\rangle$, and $\delta(t - t')$ is the Dirac delta function (see appendix B). Thus, in free space, the memory kernel is proportional to the delta function. This is because free space is an infinitely broad photon reservoir (flat spectrum) and, therefore, its response should be instantaneous. Interactions governed by such a delta-function-dependent memory kernel are said to be Markovian [14].

From equation (33) we obtain

$$\tilde{G}(s) = \gamma_{20}, \quad (35)$$

and using this in equation (30a) and (30b) we obtain

$$\tilde{c}_2(s) = \frac{s \cos \theta - \Omega e^{i\phi} \sin \theta}{D(s)}, \quad (36a)$$

$$\tilde{c}_1(s) = \frac{e^{i\phi_p} \sin \theta (s + \gamma_{20}) + \Omega e^{i\phi_c} \cos \theta}{D(s)}, \quad (36b)$$

where

$$D(s) = s^2 + \gamma_{20}s + \Omega^2 = \prod_{j=1}^2 (s - q_j), \quad (37)$$

and q_j ($j = 1, 2$) are the roots of the quadratic equation

$$x^2 + \gamma_{20}x + \Omega^2 = 0, \quad (38)$$

found by substituting $x = s$ in the equation $D(s) = 0$. They are given by

$$q_{1,2} = -\frac{\gamma_{20}}{2} \pm \sqrt{\left(\frac{\gamma_{20}}{2}\right)^2 - \Omega^2}. \quad (39)$$

Equations (36a) and (36b) are easily inverted to give

$$c_2(t) = \sum_{j=1}^2 D_j e^{q_j t}, \quad c_1(t) = \sum_{j=1}^2 E_j e^{q_j t}, \quad (40)$$

where

$$D_j = \frac{q_j \cos \theta - \Omega e^{i\phi} \sin \theta}{q_j - q_k}, \quad (j \neq k), \quad (41a)$$

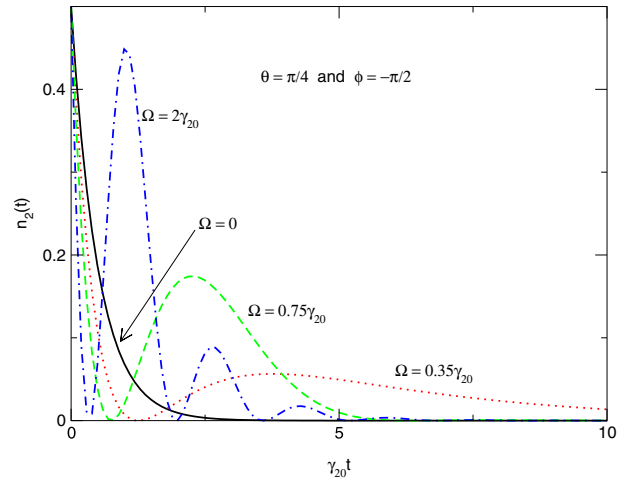


Figure 10. Atomic population $n_2(t)$ in ordinary vacuum as a function of the scaled time $\gamma_{20}t$ for the initial conditions $\theta = \pi/4$ (that is equal superposition of the upper levels), for $\phi = -\pi/2$, and for different values of Ω . The results are obtained in the leading approximation making them applicable to both the Λ and V configurations.

$$E_j = \frac{(q_j + \gamma_{20})e^{i\phi_p} \sin \theta + \Omega e^{i\phi_c} \cos \theta}{q_j - q_k}, \quad (j \neq k). \quad (41b)$$

From equation (39) we see that both roots q_j are (a) negative when $\Omega \leq \gamma_{20}/2$, and (b) complex (with a negative real part equal to $-\gamma_{20}/2$) when $\Omega > \gamma_{20}/2$. Thus the time evolution of amplitudes $c_j(t)$ (and hence of the upper-level populations $n_j(t)$) can be divided into two regimes of different behaviour. For $\Omega > \gamma_{20}/2$, the populations display pronounced oscillations before decaying to zero. On the other hand, when $\Omega < \gamma_{20}/2$ the populations barely complete an oscillation before decaying to zero. Thus, the driving field induces oscillations on the populations of the upper levels. The stronger the driving field (i.e. the larger the Ω), the faster the oscillations. This behaviour of the populations is depicted in figure 10 where $n_2(t)$ is plotted as a function of the scaled time $\gamma_{20}t$ for various of Ω . Even if $\Omega \leq \gamma_{20}/2$ (so that both roots $q_{1,2}$ are real), the coefficients $D_{1,2}$ of equation (41a) may have opposite signs leading to a minimum in $n_2(t)$ as is the case for $\Omega = 0.35\gamma_{20}$ in figure 10. When $\Omega = \gamma_{20}/2$, equation (38) has a double root $q_1 = q_2 = -\gamma_{20}/2$ and inversion of equations (36a) and (36b) gives

$$c_2(t) = \{\cos \theta - [(\gamma_{20}/2) \cos \theta + \Omega e^{i\phi} \sin \theta]t\} e^{-(\gamma_{20}/2)t}, \quad (42a)$$

$$c_1(t) = e^{i\phi_p} \{\sin \theta + [(\gamma_{20}/2) \sin \theta + \Omega e^{-i\phi} \sin \theta]t\} e^{-(\gamma_{20}/2)t}. \quad (42b)$$

Equation (39) shows that both roots $q_{1,2}$ have a negative real part, irrespective of the value of Ω . This means that the amplitudes $c_{1,2}(t)$ decay in time and tend to zero as $t \rightarrow \infty$ so that the steady-state populations n_{1s} and n_{2s} are both zero:

$$n_{js} \equiv \lim_{t \rightarrow \infty} |b_j(t)|^2 = 0, \quad (j = 1, 2). \quad (43)$$

In other words, in free space, the populations of the excited states $|2\rangle$ and $|1\rangle$ eventually decay to the ground level $|0\rangle$ (there is no population trapped on the upper levels), independent of

the strength Ω of the driving field. The only effect of the driving field is to cause transfer of populations from $|2\rangle$ to $|1\rangle$ and vice versa until all the upper-level population decays to the ground level. This is a general result valid for almost any broad-band smoothly varying electromagnetic density of states. On the other hand, when the density of electromagnetic modes vanishes in the vicinity of an atomic transition (such as near a photonic band edge) photon localization leads to non-zero steady-state atomic populations on the excited levels [65]. The extent of localization depends sensitively on Ω , and on the initial atomic state, as will be seen in section 3.4.

3.4. Model system in a PBG material

We now turn our attention to the case when the three-level atom is located within a PBS. First, we introduce a model dispersion relation for the PBG material from which we evaluate the corresponding Green function according to equation (29). The Laplace transform of this Green function is then used in equations (30a) and (30b) to evaluate $\tilde{c}_j(s)$ which, in turn, is inverted to find analytic expressions for the amplitudes $c_j(t)$ from which the relevant populations and coherences can be evaluated.

3.4.1. Model dispersion relation. In a PBG one finds a modified dispersion relation for the photons in the radiation reservoir, with a gap(s) in the photon density of states. We begin by considering an isotropic *effective mass* approximation [5, 6] for the photon dispersion relation in a PBG material:

$$\omega_{\mathbf{k}} \approx \omega_c + A(k - k_0)^2. \quad (44)$$

Here ω_c is the upper band edge frequency, k is the modulus of the wavevector \mathbf{k} , k_0 is a constant characteristic of the periodic structure, and the constant $A = (1/2)(\partial^2\omega/\partial k^2)_{k=k_0}$ measures the curvature of the dispersion curve $\omega(k)$ at $k = k_0$ [65]. For an isotropic dispersion relation $A \approx \omega_c/k_0^2 \approx c^2/\omega_c$. The dispersion relation (44) is valid for frequencies close to the upper photonic band edge. If the PBG is large, and if the relevant atomic transitions are near the upper band edge, it is a very good approximation to completely neglect the effects of the lower band.

The dispersion relation (44) is isotropic since it depends only on the magnitude k of the wavevector \mathbf{k} . While there is no physical PBG material with an isotropic gap, this provides an instructive toy model for studying quantum optical effects. Such a dispersion relation associates the band edge wavevector with a sphere in k space, $|\mathbf{k}| = k_0$ (spherical Brillouin zone). By associating the band edge with the entire sphere $|\mathbf{k}| = k_0$, the isotropic model (44) artificially increases the true phase space available for photon propagation near the band edge. This results in a photonic density of states $\rho(\omega)$ which, near the band edge ω_c , behaves as $(\omega - \omega_c)^{-1/2}$ for $\omega > \omega_c$, the square-root singularity being characteristic of a 1D phase space [5, 6].

In a real 3D dielectric crystal with an allowed point-group symmetry, the gap is highly anisotropic and the band edge is associated with a point $\mathbf{k} = \mathbf{k}_0$ (or a finite collection of symmetry-related points) in k space [67], rather than with the entire sphere $|\mathbf{k}| = |\mathbf{k}_0|$. In other words, the magnitude of the band edge wavevector varies as \mathbf{k} is rotated throughout

the Brillouin zone. Thus, a more realistic picture of the band edge behaviour requires the incorporation of the Brillouin-zone anisotropy. In the effective mass approximation, the photon dispersion relation takes the vector form

$$\omega_{\mathbf{k}} \approx \omega_c + A(\mathbf{k} - \mathbf{k}_0)^2. \quad (45)$$

In this case, however, we cannot use the approximation $A \approx c^2/\omega_c$ because the dispersion curve, in general, exhibits different slopes in different directions. Instead, we use $A \approx fc^2/\omega_c$ where f is a dimensionless scaling factor, whose value depends on the nature of the dispersion relation near the band edge ω_c . The anisotropic effective mass dispersion (45) relation leads to a photonic density of states at a band edge ω_c which behaves as $\rho(\omega) \sim (\omega - \omega_c)^{1/2}$ for $\omega > \omega_c$, characteristic of a 3D phase space [5, 6].

The isotropic dispersion relation (44) leads to qualitatively correct physics. However, the anisotropic model (45) introduces important quantitative corrections [5]. The most significant difference between the anisotropic and isotropic models comes out more explicitly when considering an undriven two-level atom with frequency near the edge of a PBG. In this case the isotropic model leads to a non-zero steady-state population on the upper level, even when the transition frequency is slightly outside the gap [65]. On the other hand, the anisotropic model leads to a fractionalized steady-state population on the upper level only when the transition frequency is inside the gap [67] (see appendix E).

Using the anisotropic effective mass dispersion relation (45) in equation (29) we can evaluate the corresponding Green function. For $(t - t')$ large enough to satisfy $\omega_c(t - t') \gg 1$, we obtain (see appendix B)

$$G(t - t') = -\alpha \frac{e^{i[\delta(t-t') + \pi/4]}}{\sqrt{4\pi(t-t')^3}}, \quad \omega_c(t - t') \gg 1, \quad (46)$$

where

$$\delta = \omega_{20} - \omega_c \quad (47)$$

represents the detuning of the atomic transition frequency ω_{20} from the upper band edge frequency ω_c . The full expression for $G(t - t')$, including its short-time behaviour, is rather complicated [158] but differs from the approximate expression (46) only in the region $(t - t') \rightarrow 0_+$, which is not of much interest to us [158], as we are mainly interested in long-time memory effects.

The constant α in equation (46) is given by (see appendix B)

$$\alpha^2 \approx \frac{1}{16f^3} \left(\frac{\gamma_{20}}{\omega_{20}} \right)^2 \omega_c, \quad (48)$$

where γ_{j0} (given by equation (34)) is half the vacuum spontaneous emission rate Γ_{j0} for the transition $|2\rangle \rightarrow |0\rangle$, and f is the dimensionless scaling factor mentioned above. At optical frequencies $\gamma_{20} \sim 10^8$ Hz and $\omega_{20} \sim 2\pi \times 10^{15}$ Hz so that $\alpha^2 \sim 10^{-17} f^{-3} \omega_c$. For $f = 10^3$, we have $\alpha^2 \sim 10^{-8} \omega_c$ which translates to $\alpha^2 \sim 10^7$ Hz when ω_c is in the optical regime.

Equation (46) shows that, for an anisotropic PBG in the effective mass approximation, the memory kernel $G(t - t')$ decays with time as $(t - t')^{-3/2}$. This is unlike the free-space case (33), where $G(t - t')$ exhibits a delta function time

dependence. Thus, equation (46) describes long-time memory effects in atom–photon interaction due to the presence of the PBG material, indicating that atom–photon interaction within a PBG material is highly non-Markovian [158]. For the isotropic dispersion relation (44) the memory kernel $G(t - t')$ decays in time more slowly as $(t - t')^{-1/2}$ (see appendix B). This enhanced memory for the isotropic model is an artifact of the singular phase space occupied by the band edge photons of vanishing group velocity.

3.4.2. Populations and coherences. From equation (46) we obtain

$$\tilde{G}(s) = \alpha e^{i\pi/4} \sqrt{s - i\delta}, \quad (49)$$

and using this in equations (30a) and (30b) we obtain

$$\tilde{c}_2(s + i\delta) = \frac{(s + i\delta) \cos \theta - \Omega e^{i\phi} \sin \theta}{D(s)}, \quad (50a)$$

$$\tilde{c}_1(s + i\delta) = \frac{(s + \alpha e^{i\pi/4} \sqrt{s + i\delta}) e^{i\phi_p} \sin \theta + \Omega e^{i\phi_c} \cos \theta}{D(s)}, \quad (50b)$$

where

$$D(s) = (s + i\delta)^2 + \alpha e^{i\pi/4} (s + i\delta) \sqrt{s} + \Omega^2 = \prod_{j=1}^4 (\sqrt{s} - e^{i\pi/4} u_j). \quad (51)$$

Here $u_j (j = 1, \dots, 4)$ are the roots of the quartic equation

$$x^4 + \alpha x^3 + 2\delta x^2 + \alpha \delta x - (\Omega^2 - \delta^2) = 0 \quad (52)$$

found by substituting $x = e^{-i\pi/4} \sqrt{s}$ in the equation $D(s) = 0$. These roots are given by [159]

$$u_{1,3} = -\sigma_1 \pm [A - r/2 + \sigma_1^2]^{1/2}, \quad (53a)$$

$$u_2 = u_4^* = -\sigma_2 - i[A + r/2 - \sigma_2^2]^{1/2}, \quad (53b)$$

where

$$A = (r^2/4 + \Omega^2 - \delta^2)^{1/2}, \quad (54a)$$

$$\sigma_{1,2} = \frac{1}{4} \left(\alpha \pm \sqrt{\alpha^2 - 8\delta + 4r} \right), \quad (54b)$$

$$r = (B - q/2)^{1/3} - (B + q/2)^{1/3} + \eta_1/3, \quad (54c)$$

$$B = \left[\left(\frac{p}{3} \right)^3 + \left(\frac{q}{2} \right)^2 \right]^{1/2}, \quad (54d)$$

$$p = -\frac{\eta_1^2}{3} + \eta_2, \quad q = -2 \left(\frac{\eta_1}{3} \right)^3 + \frac{\eta_1 \eta_2}{3} + \eta_3, \quad (54e)$$

$$\eta_1 = 2\delta, \quad \eta_2 = \alpha^2 \delta + 4(\Omega^2 - \delta^2), \quad (54f)$$

$$\eta_3 = (\alpha^2 - 8\delta)(\Omega^2 - \delta^2) - \alpha^2 \delta^2. \quad (54g)$$

Numerical analysis shows that the roots $u_{1,3}$ are real (u_1 is positive but u_3 is negative) whereas the roots $u_{2,4}$ are complex conjugates of each other with a negative real part (u_2 and u_4 lie in the third and second quadrants, respectively).

The amplitude $c_j(t)$ is found by inverting $\tilde{c}_j(s + i\delta)$ using the complex inversion formula [157] which involves a contour integration in the complex s plane (see appendix C). We obtain

$$c_2(t) = \sum_{j=1}^2 P_j Q_j e^{i(u_j^2 + \delta)t} + \frac{\alpha e^{i\pi/4}}{\pi} \int_0^\infty \frac{g_2(x) e^{-(x-i\delta)t}}{Z(x)} dx, \quad (55a)$$

$$c_1(t) = \sum_{j=1}^2 P_j R_j e^{i(u_j^2 + \delta)t} + \frac{\alpha \Omega e^{i(\phi_c + \pi/4)}}{\pi} \int_0^\infty \frac{g_1(x) e^{-xt}}{Z(x)} dx, \quad (55b)$$

where

$$P_j = \frac{2u_j}{(u_j - u_l)(u_j - u_m)(u_j - u_n)}, \quad (56a)$$

$$(l, m, n = 1, \dots, 4, j \neq l \neq m \neq n),$$

$$Q_j = (u_j^2 + \delta) \cos \theta + i\Omega e^{i\phi} \sin \theta, \quad (56b)$$

$$R_j = (u_j^2 + \alpha u_j + \delta) e^{i\phi_p} \sin \theta - i\Omega e^{i\phi_c} \cos \theta, \quad (56c)$$

$$g_2(x) = [(-x + i\delta) \cos \theta - \Omega e^{i\phi} \sin \theta] (-x + i\delta) \sqrt{x}, \quad (56d)$$

$$g_1(x) = [(-x + i\delta) \cos \theta - \Omega e^{i\phi} \sin \theta] \sqrt{x}, \quad (56e)$$

$$Z(x) = [(-x + i\delta)^2 + \Omega^2]^2 + i\alpha^2 (-x + i\delta)^2. \quad (56f)$$

Since u_1 is real, and u_2 is complex (with negative real and imaginary parts), the first term in the right-hand side of equation (55a) is a non-decaying oscillatory term, whereas the second term is also oscillatory but decays exponentially to zero as $t \rightarrow \infty$. The last term containing the integral represents the branch cut contribution (arising from the deformation of the contour of integration around a branch point in the complex inversion formula). This also decays to zero as $t \rightarrow \infty$, albeit faster than the second term.

Equation (55a) shows that level $|2\rangle$ is split into two dressed states. This dressed-state splitting is the combined effect of vacuum-field Rabi splitting by the gap [43] and the Autler–Townes splitting [71] by the external field. The dressed states occur at frequencies (noting that root u_1 is real, whereas $\text{Re}\{u_2^2\} < 0$)

$$\begin{aligned} \omega_{20} - (\delta + \text{Im}\{iu_1^2\}) &= \omega_c - \text{Im}\{iu_1^2\} = \omega_c - u_1^2, \\ \omega_{20} - (\delta + \text{Im}\{iu_2^2\}) &= \omega_c - \text{Im}\{iu_2^2\} \\ &= \omega_c - \text{Re}\{u_2^2\} = \omega_c + |\text{Re}\{u_2^2\}|. \end{aligned} \quad (57)$$

The dressed state at frequency $\omega_c - u_1^2$ lies inside the gap and corresponds to the photon–atom bound dressed state with no decay in time. A photon emitted by an atom in such a dressed state will exhibit tunnelling on a length scale given by the localization length ξ_{loc} before being Bragg reflected back to the emitting atom to re-excite it. For a band gap to centre frequency ratio of $\Delta\omega/\omega_0 \sim 5\%$, the photon localization length $\xi_{\text{loc}} \geq L$, where L is the lattice constant of the dielectric [5, 6]. The photon–atom bound state is the optical analogue of an electron–impurity level bound state in the gap of a semiconductor.

The dressed state at the frequency $\omega_c + |\text{Re}\{u_2^2\}|$ lies outside the gap and decays at a rate of $\text{Im}\{u_2^2\}$. It results in highly non-Markovian decay of the atomic population $n_2(t)$. As ω_{20} is detuned further into the gap (i.e. as δ becomes more negative), a greater fraction of the light is localized in the gap dressed state. Conversely, as ω_{20} is moved out of the gap, total emission intensity from the decaying dressed state is increased [65, 158]. As a result of interference between the three terms in equation (55a), the spontaneous emission dynamics displays oscillatory behaviour [65]. As can be seen from equations (55a) and (55b), the dynamics of spontaneous emission strongly depends on the detuning $\delta = \omega_{20} - \omega_c$ of level $|2\rangle$ from the upper band edge, the initial coherent superposition state as defined by the parameter θ , the intensity

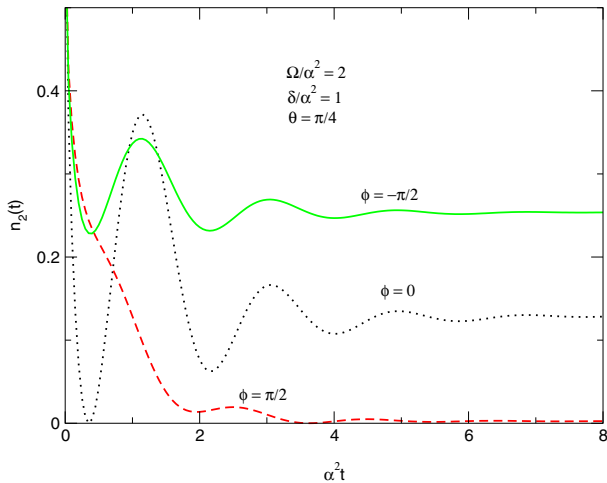


Figure 11. Atomic population $n_2(t)$ in a PBG material as a function of the scaled time $\alpha^2 t$ for $\Omega/\alpha^2 = 2$, $\delta/\alpha^2 = 1$, $\theta = \pi/4$, and for various values of the relative phase ϕ . The photon dispersion is described by the anisotropic effective mass approximation (45). The steady-state population of level $|2\rangle$ is largest for the relative phase $\phi = -\pi/2$. The results are obtained in the leading approximation making them applicable to both the Λ and V configurations.

Ω of the control laser driving the transition between the upper levels, and the relative phase $\phi = \phi_p - \phi_c$ between the cw control laser field and the pumping laser pulse.

In figure 11 we plot the atomic population $n_2(t)$ as a function of the scaled time $\alpha^2 t$ for various values of the relative phase ϕ . This figure shows that, all other conditions being equal, the fractionalized steady-state population on the excited states is maximum or minimum when the relative phase is $\phi = -\pi/2$ or $\pi/2$, respectively. Figure 12 depicts the population $n_2(t)$ for various values of Ω . From this figure we note that, as Ω is increased, $n_2(t)$ oscillates faster and reaches its steady-state value more quickly. Moreover, the steady-state value n_{2s} increases with Ω .

In the long-time limit, only the first terms in equations (55a) and (55b) remain dominant, since u_1 is real whereas u_2 is complex with a negative real part. The steady-state populations n_{js} on the upper levels $|2\rangle$ and $|1\rangle$ are thus given by

$$n_{2s} = |P_1 Q_1|^2, \quad n_{1s} = |P_1 R_1|^2. \quad (58)$$

This phenomenon of population trapping is due to the presence of a PBG material and is absent in free space. It is apparent from equations (54a)–(54g), and (56a)–(56f) that the steady-state populations n_{js} depend strongly on the parameters θ , $\phi = \phi_p - \phi_c$, $\delta = \omega_{20} - \omega_c$, and Ω .

Figure 13 shows the variation of the steady-state population n_{2s} of level $|2\rangle$ with respect to the detuning δ . We see that as δ increases from zero (that is, as level $|2\rangle$ is pushed farther away from the band edge into the continuum) the steady-state population n_{2s} initially increases and attains its maximum value of about 0.295 at about $\delta \approx 0.5\alpha^2$ before it begins to decrease very rapidly. In other words, there is a fractionalized steady-state atomic population on the excited state $|2\rangle$ even when the bare excitation frequency of this level lies outside of the PBG, but not far from the band edge. Remarkably, spontaneous emission is partially

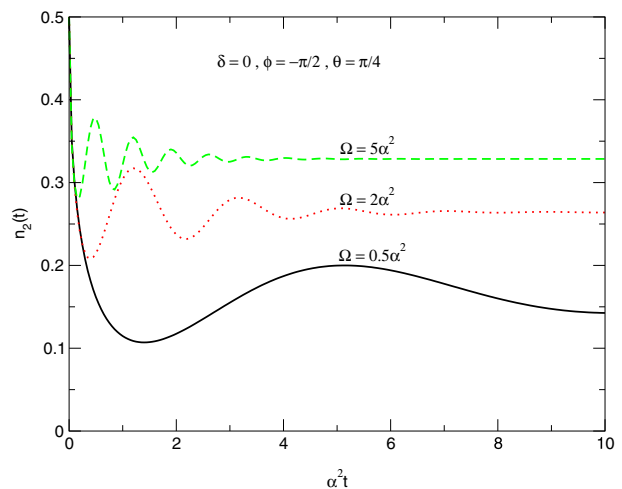


Figure 12. Atomic population $n_2(t)$ as a function of the scaled time $\alpha^2 t$ for $\delta = 0$ (i.e. when the transition $|2\rangle \rightarrow |0\rangle$ coincides with the anisotropic band edge), for the relative phase $\phi = -\pi/2$, for $\theta = \pi/4$, and for different values of Ω . Note that as Ω is increased, $n_2(t)$ oscillates faster and reaches its steady-state value more quickly. Moreover, the steady-state value n_{2s} increases with Ω . The results are obtained in the leading approximation making them applicable to both the Λ and V configurations.

inhibited even within the allowed electromagnetic continuum as a consequence of quantum interference with the driving field which couples level $|2\rangle$ to the photon–atom bound state associated with level $|1\rangle$. When there is no driving field, our model system can be viewed as a two-level system consisting of levels $|2\rangle$ and $|0\rangle$, with the transition frequency ω_{20} near the edge of a PBG. As shown in appendix E, for such a two-level atom and the anisotropic dispersion relation (45), the steady-state population on the excited level $|2\rangle$ vanishes when the level is at the band edge or outside the gap. However, population trapping in a V system, on level $|2\rangle$ outside the PBG, in the absence of a control laser field, may be recaptured by going beyond the leading approximation and including the spontaneous emission channel $|1\rangle \rightarrow |0\rangle$.

Figure 14 depicts the variation of n_{2s} with respect to the strength Ω of the driving field for various values of the relative phase ϕ . This figure shows that n_{2s} can be an increasing or decreasing function of Ω depending on the value of the relative phase ϕ .

For a driving laser field so strong that $\Omega \gg \alpha^2, \delta$, the steady-state populations n_{js} are given approximately by (see appendix C)

$$n_{2s} \approx n_{1s} \approx \frac{1}{4}(1 - \sin 2\theta \sin \phi), \quad \Omega \gg \alpha^2, \delta. \quad (59)$$

Thus, when $\theta = 0$ (when the atom is initially on level $|2\rangle$) or when $\theta = \pi/2$ (when the atom is initially on level $|1\rangle$), we have $n_{2s} = n_{1s} = 1/4$. In other words, for the case of a strong laser field, the steady-state atomic populations n_{2s} and n_{1s} are independent of the initial relative phase ϕ (if the system is not initially prepared as a coherent superposition of the upper states). However, if the atom is initially prepared in a coherent superposition of the two upper states $|2\rangle$ and $|1\rangle$, so that $\sin(2\theta) \neq 0$ in equation (59), the steady-state atomic populations will also depend on ϕ . For instance, when $\theta = \pi/4$, spontaneous emission is strongly enhanced

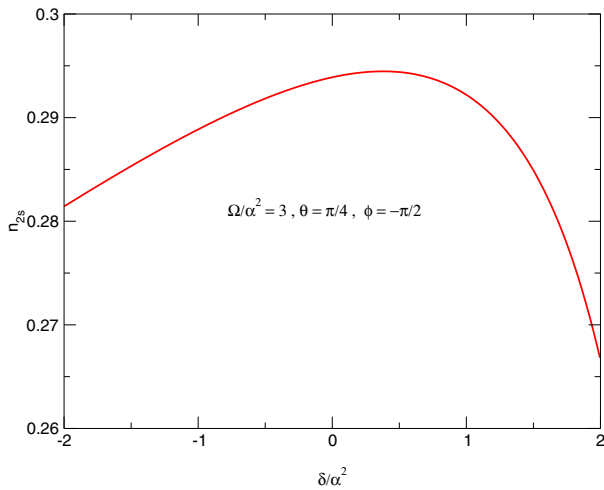


Figure 13. Steady-state population n_{2s} of level $|2\rangle$ as a function of the detuning δ from the anisotropic 3D band edge for $\Omega/\alpha^2 = 3$, $\theta = \pi/4$, and for the relative phase $\phi = -\pi/2$ (which, as seen in figure 11, leads to a large steady-state population). Note that n_{2s} is non-zero even for $\delta > 0$ (that is, even when ω_{20} lies outside the gap). In fact n_{2s} attains its maximum value outside the gap at $\delta \approx 0.5\alpha^2$.

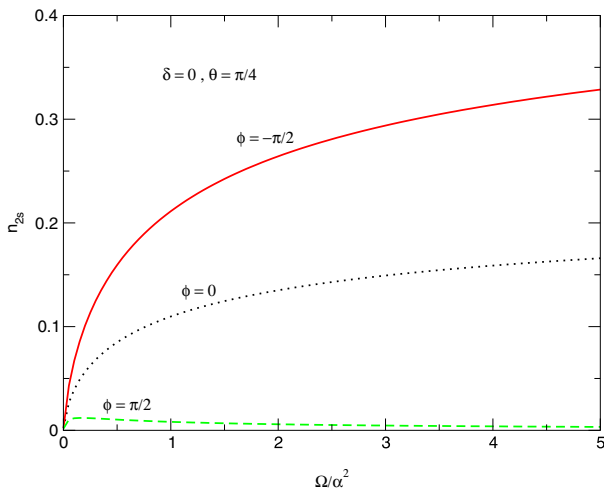


Figure 14. Steady-state population n_{2s} of level $|2\rangle$ as a function of Ω for $\delta = 0$, $\theta = \pi/4$, and for different values of ϕ . n_{2s} can be an increasing or decreasing function of Ω depending on the relative phase ϕ . Results for the Λ and V configurations are the same in the leading approximation.

($n_{2s} + n_{1s} \approx 0$) for $\phi = \pi/2$, whereas it is totally suppressed ($n_{2s} + n_{1s} \approx 1$) for $\phi = -\pi/2$. Clearly, the steady-state atomic population keeps memory of the initial relative phase ϕ . It can be controlled by changing the optical paths of the pumping and controlling lasers. Moreover, due to the effects of photon localization, the atom keeps memory of the intensity and phase of the pump (input) laser pulse. This suggests that *our model system can serve as an optical memory device on the atomic scale*.

Next we evaluate the coherences between the upper levels $|2\rangle$ and $|1\rangle$ as defined by equations (23) and (24). From equations (55a) and (55b) we obtain

$$n_{cs} = \lim_{t \rightarrow \infty} c_2(t)c_1^*(t) = |P_1|^2 Q_1 R_1^*, \quad (60)$$

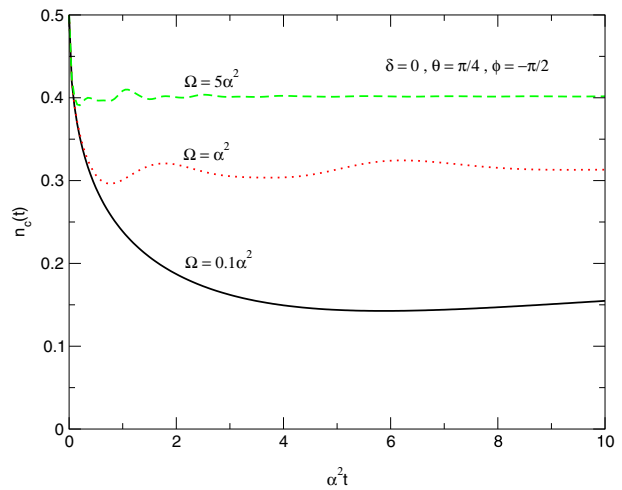


Figure 15. The magnitude $|n_c(t)| = |c_2(t)c_1^*(t)|$ of the coherence between levels $|2\rangle$ and $|1\rangle$ as a function of the scaled time $\alpha^2 t$ for $\delta = 0$, $\theta = \pi/4$, $\phi = -\pi/2$, and for different values of Ω . Results apply to both Λ and V systems.

and for a very strong control laser field ($\Omega \gg \alpha^2, \delta$) this reduces to (see appendix C)

$$n_{cs} \approx \frac{ie^{-i\phi_c}}{4} (1 - \sin 2\theta \sin \phi), \quad \Omega \gg \alpha^2, \delta. \quad (61)$$

Thus, not only do the upper levels $|2\rangle$ and $|1\rangle$ have non-zero populations (n_{2s} and n_{1s}) in the steady-state limit, as required for a classical memory device, but the coherences are non-zero in the steady-state limit, as required for quantum memory. In essence, coherence is forced on the atomic system by means of the external laser field. Like the populations $n_{1,2}(t)$, the coherence $n_c(t) = c_2(t)c_1^*(t)$ depends strongly on the parameters θ , $\phi = \phi_p - \phi_c$, $\delta = \omega_{20} - \omega_c$ and Ω . Equation (61) shows that for large Ω and when the system is initially prepared in a coherent superposition of the upper states (that is, when $\theta \neq 0, \pi/2$), the coherence $n_c(t)$ between levels $|2\rangle$ and $|1\rangle$ can be controlled by the relative phase ϕ and attains its maximum value when $\phi = -\pi/2$. In figure 15 we plot the magnitude $|n_c(t)| = |c_2(t)c_1^*(t)|$ of the coherence as a function of the scaled time $\alpha^2 t$ for different values of Ω . We see that, for the chosen conditions, $n_c(t)$ increases with increasing Ω . In section 4 we discuss how the coherence $n_c(t)$ is influenced by other spontaneous emission and non-radiative effects that are not considered within the leading approximation.

The above considerations suggest that quantum information can be ‘written’ onto a single three-level atom by choosing the ‘area’ of the incident laser pulse, the intensity of the cw laser, and the relative optical path lengths of the cw and pulse laser beams. In other words, the precise nature of the information written onto the quantum bit or ‘qubit’ can be controllably altered by varying these external parameters. Furthermore, the phase and intensity of the control laser field can be adjusted so that spontaneous emission can be totally suppressed in our model system. That is to say, at steady state, the system can be in a coherent superposition of the upper states $|2\rangle$ and $|1\rangle$ as $|\phi\rangle = a_2|2\rangle + a_1|1\rangle$ with $|a_2|^2 + |a_1|^2 = 1$, the amplitudes a_2 and a_1 being dependent on the phase and intensity of the pump laser pulse. *Since this superposition state is immune to*

single-photon radiative decay it is a promising candidate for a two-level quantum bit to encode information in quantum computations. In section 4 we discuss some possible decoherence mechanisms which may alter the above picture. Decoherence is the greatest obstacle to quantum computation since it causes a pure quantum state to evolve into a mixture of states and to thereby lose two of its key properties: interference and entanglement [162].

4. Effects of other spontaneous emission terms

4.1. Model Hamiltonian and equation of motion

In the leading approximation for our model system of figure 9 we have assumed that spontaneous emission on the transitions $|2\rangle \rightarrow |1\rangle$ and $|1\rangle \rightarrow |0\rangle$ is inhibited, either by symmetry consideration or by the presence of the PBG. We next relax this assumption to see its effects on the system dynamics. To this end we consider the V configuration of figure 9(b), where the upper levels $|1\rangle$ and $|2\rangle$ are of the same symmetry and are both coupled by dipole transitions to the ground level $|0\rangle$. In this case the unperturbed Hamiltonian H_0 is still the same as that of equation (4), whereas H_I has an additional term due to the now allowed $|1\rangle \rightarrow |0\rangle$ transition. It is given by (see appendix A)

$$H_I = i\hbar\Omega[e^{i(\omega_c t + \phi_c)}\sigma_{12} - e^{-i(\omega_c t + \phi_c)}\sigma_{21}] + i\hbar \sum_{k\lambda} [g_{k\lambda}^{20}(a_{k\lambda}^\dagger\sigma_{02} - \sigma_{20}a_{k\lambda}) + g_{k\lambda}^{10}(a_{k\lambda}^\dagger\sigma_{01} - \sigma_{10}a_{k\lambda})], \quad (62)$$

where Ω is the Rabi frequency of the driving field given by equation (10), $\omega_c = 2\omega_L$ and

$$g_{k\lambda}^{ij} = \frac{\omega_{ij}d_{ij}}{\hbar} \left(\frac{\hbar}{2\epsilon_0\omega_k V} \right)^{1/2} \hat{e}_{k\lambda} \cdot \hat{d}_{ij} \quad (63)$$

is the coupling constant between the atomic transition $|i\rangle \rightarrow |j\rangle$ and the mode $\{k\lambda\}$ of the radiation field. The various factors in equation (63) are defined in section 3.2 in connection with equation (6).

With interaction Hamiltonian (62), equations (25a)–(25c) are now replaced by

$$\dot{c}_{k\lambda}(t) = g_{k\lambda}^{20}c_2(t)e^{i\mu_k^{20}t} + g_{k\lambda}^{10}c_1(t)e^{i\mu_k^{10}t}, \quad (64a)$$

$$\dot{c}_1(t) = \Omega e^{i\phi_c}c_2(t) - \sum_{k\lambda} g_{k\lambda}^{10}c_{k\lambda}(t)e^{-i\mu_k^{10}t}, \quad (64b)$$

$$\dot{c}_2(t) = -\Omega e^{-i\phi_c}c_1(t) - \sum_{k\lambda} g_{k\lambda}^{20}c_{k\lambda}(t)e^{-i\mu_k^{20}t}, \quad (64c)$$

where

$$\mu_k^{ij} = \omega_k - \omega_{ij}, \quad (65)$$

is the detuning of the radiation mode frequency ω_k from the atomic transition frequency ω_{ij} . Formal integration (in time) of equation (64a), with the initial condition $c_{k\lambda}(0) = 0$ of equation (19), yields

$$c_{k\lambda}(t) = g_{k\lambda}^{20} \int_0^t c_2(t')e^{i\mu_k^{20}t'} dt' + g_{k\lambda}^{10} \int_0^t c_1(t')e^{i\mu_k^{10}t'} dt'. \quad (66)$$

Substituting this expression for $c_{k\lambda}(t)$ in equation (64b) and (64c) we obtain

$$\dot{c}_1(t) = \Omega e^{i\phi_c}c_2(t) - \int_0^t G_{11}(t-t')c_1(t') dt' - e^{-i\omega_{21}t} \int_0^t G_{12}(t-t')c_2(t') dt', \quad (67a)$$

$$\dot{c}_2(t) = -\Omega e^{-i\phi_c}c_1(t) - \int_0^t G_{22}(t-t')c_2(t') dt' - e^{i\omega_{21}t} \int_0^t G_{21}(t-t')c_1(t') dt', \quad (67b)$$

where

$$G_{ij}(t-t') = \sum_{k\lambda} g_k^{i0} g_{k\lambda}^{j0} e^{-i\mu_{k\lambda}^{ij}(t-t')} \quad (68)$$

are the delay Green functions. Equations (67a) and (67b) are the generalized versions of equations (28a) and (28b) for a V system including spontaneous emission on the transition $|1\rangle \rightarrow |0\rangle$. As in section 3, we are interested in solving these generalized equations for the amplitudes $c_{1,2}(t)$ which can then be used to evaluate the populations and coherences of the atomic levels.

In order to explicitly see the effects of the laser field driving the transition $|2\rangle \rightarrow |1\rangle$ on the system dynamics, we consider the case without a driving field separately from the case with a driving field. We refer to the case without a driving field ($\Omega = 0$) as the *quantum beats* case. The case when the driving field is in the form of continuous wave laser so that Ω is a non-zero constant independent of time is referred to as the *coherent control* case. The quantum beats case, besides being an interesting case in its own right, will be a valuable reference case for interpreting the results of the coherent control cases.

4.2. Model system in vacuum

When the three-level atom in the V configuration is in free space, we use the dispersion relation (32) in equation (68) to obtain (see appendix B)

$$G_{ij}(t-t') = \eta_{ij} \sqrt{\gamma_{i0}\gamma_{j0}} \delta(t-t'), \quad (69)$$

where γ_{m0} is half the spontaneous emission rate for the transition $|m\rangle \rightarrow |0\rangle$ given by equation (34), $\delta(t-t')$ is the Dirac delta function, and

$$\eta_{ij} = \delta_{ij} + \eta(1 - \delta_{ij}). \quad (70)$$

Here δ_{ij} is the Kronecker delta function and η is a constant (defined in appendix B) which satisfies $|\eta| \leq 1$, the equality sign holding when the dipoles associated with the transitions $|i\rangle \rightarrow |0\rangle$ and $|j\rangle \rightarrow |0\rangle$ are parallel or antiparallel so that $\hat{d}_{i0} = \pm \hat{d}_{j0}$. The factor η_{ij} measures the ‘strength’ of the scattering processes in which a quantum is first emitted in the transition $|0\rangle \rightarrow |i\rangle$ and then reabsorbed in the transition $|0\rangle \rightarrow |j\rangle$, or vice versa. We refer to this factor as the ‘scattering coefficient’.

Using equation (69) in the general equations (67a) and (67b), we obtain

$$\dot{c}_1(t) = -\gamma_{10}c_1(t) + [\Omega e^{i\phi_c} - \eta\bar{\gamma}e^{-i\omega_{21}t}]c_2(t), \quad (71a)$$

$$\dot{c}_2(t) = -\gamma_{20}c_2(t) - [\Omega e^{-i\phi_c} + \eta\bar{\gamma}e^{i\omega_{21}t}]c_1(t), \quad (71b)$$

where

$$\bar{\gamma} = \sqrt{\gamma_{10}\gamma_{20}}. \quad (72)$$

If we neglect spontaneous emission on the transition $|1\rangle \rightarrow |0\rangle$ so that both γ_{10} and η are zero, equations (71a) and (71b) reduce to equations (28a) and (28b) when we use equation (69). In other words, the leading approximation of section 3 is a special case of the general problem considered in this section when both γ_{10} and η are set to zero.

4.2.1. Quantum beats in vacuum. In the quantum beats problem ($\Omega = 0$), equations (71a) and (71b), have closed analytical solutions given by (see appendix D.1)

$$c_2(t) = e^{-\gamma_{20}t} \sum_{j=1}^2 A_j e^{q_j t}, \quad (73)$$

$$c_1(t) = e^{-(\gamma_{20} + i\omega_{21})t} \sum_{j=1}^2 B_j e^{q_j t},$$

where

$$q_{1,2} = \frac{\lambda}{2} \pm \sqrt{\left(\frac{\lambda}{2}\right)^2 + (\eta\bar{\gamma})^2}, \quad (74a)$$

$$\lambda = \gamma_{20} - \gamma_{10} + i\omega_{21}, \quad (74b)$$

$$A_j = \frac{q_k c_2(0) + \eta\bar{\gamma} c_1(0)}{q_k - q_j}, \quad (k \neq j), \quad (74c)$$

$$B_j = -q_j A_j / \eta\bar{\gamma}. \quad (74d)$$

A special case of the quantum beat problem ($\Omega = 0$) is when multiple scattering events are ignored so that $\eta = 0$, such as when the dipole moments associated with the two allowed transitions are perpendicular. In this special case, equations (71a) and (71b) have simple exponentially decaying solutions

$$c_j(t) = c_j(0)e^{-\gamma_{j0}t}, \quad \text{for } \eta = 0, \quad (75)$$

where $c_j(0)$ represents the initial value of $c_j(t)$ as given by equation (19). Comparing these solutions with the general solutions (73) we see that

$$\begin{aligned} A_1 &= 0, & A_2 &= c_2(0), \\ B_1 &= c_1(0), & B_2 &= 0, \end{aligned} \quad \text{for } \eta = 0. \quad (76)$$

The phenomenon of quantum beats in the absence of multiple scattering events (that is, when both Ω and η are set to zero in equations (71a) and (71b)) is now a standard text book problem [14]. The case when $\eta = 1$, that is when the dipoles associated with the two allowed transitions are parallel or antiparallel, has been discussed in detail in [163]. The general model considered here, which is valid for $0 \leq \eta \leq 1$, recaptures these specialized results [164].

Since the roots $q_{1,2}$ are in general complex, equation (73) shows that the decay of the amplitudes $c_{1,2}(t)$ (and hence of the populations $n_{1,2}(t)$) are not purely exponential and may display oscillatory behaviour depending on the initial coherent superposition state defined by $c_1(0)$ and $c_2(0)$, on the decay rates γ_{10} and γ_{20} , and on the frequency separation ω_{21} between the two upper levels [163]. If, for instance, the system is initially prepared in the state $|\Psi(0)\rangle = |2\rangle$, then, in the course

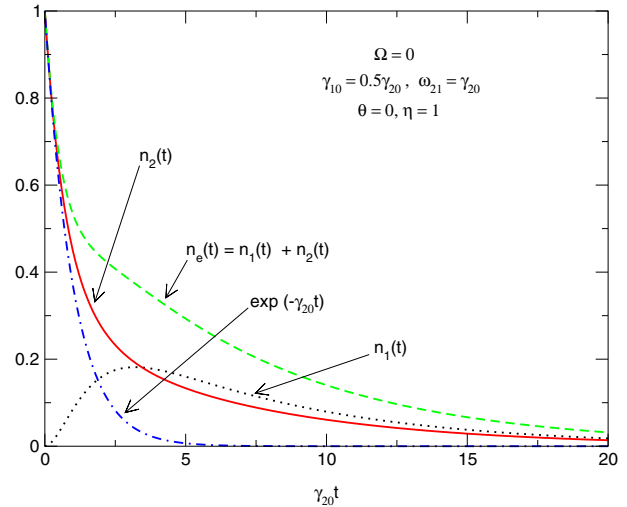


Figure 16. Atomic populations $n_1(t)$, $n_2(t)$, and total excited-state population $n_e(t) = n_1(t) + n_2(t)$ functions of the scaled time $\gamma_{20}t$ in the vacuum quantum beat problem ($\Omega = 0$) for $\gamma_{10} = 0.5\gamma_{20}$ and $\omega_{21} = \gamma_{20}$. We have assumed that dipoles associated with the two allowed transitions are parallel so that $\eta = 1$ and have used the initial condition $\theta = 0$ (that is, the atom is initially on level $|2\rangle$). The dot-dashed curve is the simple exponential curve $e^{-\gamma_{20}t}$ drawn for reference.

of time, the population of level $|1\rangle$ increases from zero to a maximum and then decreases to zero, while that of level $|2\rangle$ monotonically decreases to zero (see figure 16).

The detected signal resulting from spontaneous emission from the three-level system is proportional to

$$\mathcal{J}(t) = \left| \sum_{k\lambda} c_{k\lambda}(t) \exp\{i(\mathbf{k} \cdot \mathbf{r} - \omega_k t)\} \right|^2 \quad (77)$$

where \mathbf{r} is the position of the detector relative to the emitting atom [14]. According to equation (66), the amplitude $c_{k\lambda}(t)$ contains contributions from $c_1(t')$ and $c_2(t')$ ($0 \leq t' \leq t$) which will, in general, interfere with each other. The temporal interference of the two possible transitions $|2\rangle \rightarrow |0\rangle$ and $|1\rangle \rightarrow |0\rangle$ gives rise to a fluorescence signal that *has a component modulated at the difference frequency ω_{21}* . This is the phenomenon of *quantum beats* and is the basis of a spectroscopic technique used to determine the difference in frequency between two atomic levels [14]. When $\eta = 0$, no quantum beats are observed [14] if either $c_1(0)$ or $c_2(0)$ vanishes (i.e. if the system is not initially prepared in a coherent superposition of the upper states). However, quantum beats do indeed occur when $\eta \neq 0$, even if either $c_1(0)$ or $c_2(0)$ is zero. In other words, *when multiple scattering events are taken into account, quantum beats do indeed occur even if the system is not initially prepared in a coherent superposition of the upper states.*

Thus, in the free-space quantum beats problem, the ‘scattering coefficient’ η plays a prominent role in the system dynamics and it is important to include multiple scattering events. This is especially true when the allowed transitions $|2\rangle \rightarrow |0\rangle$ and $|1\rangle \rightarrow |0\rangle$ are very close to each other so that $\omega_{21} \ll \omega_{20}, \omega_{10}$. The interference between the two possible transitions accounts for the dark line in the spontaneous emission spectrum of a three-level atom in the V configuration

observed in [163]. In the absence of interference between the two spontaneous emission decay processes, one expects the spectrum of the three-level atom to consist of two Lorentzian distributions peaked at the two transition frequencies. Instead, what is obtained is a single distribution with a dark band, whose width depends on the decay rates γ_{10} and γ_{20} .

4.2.2. Coherent control in vacuum. In the coherent control problem ($\Omega \neq 0$), equations (71a) and (71b) must, in general, be solved numerically. However, in the special case when $\eta = 0$, the equations can be solved using the method shown in appendix D to solve equations (71a) and (71b) in the quantum beats case. We obtain

$$c_j(t) = e^{-\gamma_j t} f_j(t), \quad (j = 1, 2), \quad (78)$$

where

$$f_2(t) = \sum_{j=1}^2 D_j e^{r_j t}, \quad f_1(t) = e^{-\lambda t} \sum_{j=1}^2 E_j e^{r_j t}, \quad (79)$$

with

$$\lambda = \gamma_{20} - \gamma_{10}, \quad (80a)$$

$$r_{1,2} = \frac{\lambda}{2} \pm i \sqrt{\Omega^2 - \left(\frac{\lambda}{2}\right)^2}, \quad (80b)$$

$$D_j = \frac{r_k c_2(0) + e^{i\phi_c} \Omega c_1(0)}{r_k - r_j} \quad (k \neq j), \quad (80c)$$

$$E_j = -e^{-i\phi_c} r_j D_j / \Omega. \quad (80d)$$

In both the coherent control case and the quantum beat case, the population dynamics depends on the initial coherent superposition state (as defined by θ and ϕ_p) as well as on the parameters $\gamma_{10}, \gamma_{20}, \omega_{21}$, and η . In the coherent control case, the atomic population has an additional dependence on the intensity Ω and phase ϕ_c of the control laser field. The driving field causes transfer of populations from $|2\rangle$ to $|1\rangle$, as shown in figure 17 by the oscillations in $n_1(t)$ for various values of Ω . The stronger the driving field, the higher the frequency of oscillation of the populations $n_{1,2}(t)$. For free space, the steady-state atomic populations on the upper levels are zero, irrespective of the strength Ω of the control laser field. In other words there is no population trapping in free space.

4.3. Model system in a PBG material

For the anisotropic effective mass dispersion relation (45), the Green functions (68) take the form (see appendix B)

$$G_{ij}(t-t') = -\eta_{ij} \alpha \frac{e^{i[\delta_{j1}(t-t') + \pi/4]}}{\sqrt{\pi(t-t')^3}}, \quad \omega_c(t-t') \gg 1 \quad (81)$$

where η_{ij} and α^2 are given, respectively, by equations (70) and (48), and

$$\delta_{ij} = \omega_{ij} - \omega_c \quad (82)$$

is the detuning of the atomic transition frequency ω_{ij} from the upper band-edge frequency ω_c . Substituting equation (81) into equations (67a) and (67b) we can find the coupled equations for the amplitudes $c_{1,2}(t)$ appropriate for a PBG analogous to

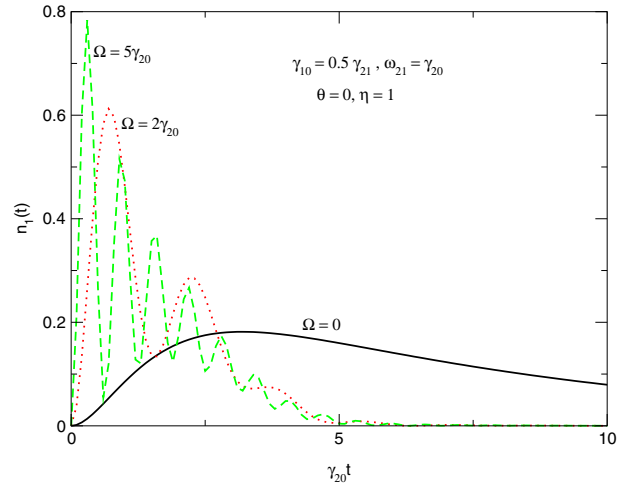


Figure 17. Atomic population $n_1(t)$ as a function of the scaled time $\gamma_{20}t$ in the vacuum quantum beats ($\Omega = 0$) and coherent control ($\Omega \neq 0$) problems, for various values of Ω . In all cases we have assumed that $\theta = 0$, $\phi = -\pi/2$, $\gamma_{10} = 0.5\gamma_{20}$, $\omega_{21} = \gamma_{20}$, and $\eta = 1$. Note that the stronger the driving field, the faster the oscillations, but the steady-state population is always zero, irrespective of the value of Ω .

equations (71a) and (71b) for vacuum. However, in the PBG case, it is convenient to introduce the new amplitudes $h_{1,2}(t)$:

$$c_j(t) = h_j(t) e^{i\delta_j t}, \quad (j = 1, 2). \quad (83)$$

In terms of these new amplitudes and the Green functions (81), equations (64a) and (64b) can be rewritten as

$$\begin{aligned} \dot{h}_1(t) &= -i\delta_{10}h_1(t) + \Omega e^{i(\omega_{21}t + \phi_c)} h_2(t) \\ &\quad - \int_0^t G(t-t') [h_1(t') + \eta h_2(t')] dt', \end{aligned} \quad (84a)$$

$$\begin{aligned} \dot{h}_2(t) &= -i\delta_{20}h_2(t) - \Omega e^{-i(\omega_{21}t + \phi_c)} h_1(t) \\ &\quad - \int_0^t G(t-t') [h_2(t') + \eta h_1(t')] dt', \end{aligned} \quad (84b)$$

where

$$G(t-t') = -\alpha e^{i\pi/4} / \sqrt{4\pi(t-t')^3}. \quad (85)$$

4.3.1. Quantum beats near the edge of a PBG. The quantum beats problem corresponds to the case when $\Omega = 0$ in equations (84a) and (84b). This case has also been investigated in [160], using the ‘effective mass’ isotropic dispersion model (44). In this section we discuss the problem using the more realistic anisotropic dispersion model (45).

For $\Omega = 0$, equations (84a) and (84b) can be solved to give closed analytic expressions for the amplitudes $h_{1,2}(t)$. These expressions take particularly simple forms when the band-edge ω_c is midway between the two upper of levels of the V system so that $\delta_{20} = -\delta_{10} = \delta$ (thus $\delta \geq 0$), and when the atomic dipoles associated with the transitions $|2\rangle \rightarrow |0\rangle$ and $|1\rangle \rightarrow |0\rangle$ are parallel (or antiparallel) so that $\eta = 1$. In this special case the solutions to equations (84a) and (84b) are given by (see appendix D.2)

$$c_2(t) = \sum_{j=1}^2 S_j T_j e^{i(\omega_j^2 + \delta)t} + \frac{e^{i\pi/4}}{\pi} \int_0^\infty \frac{f_2(x) e^{-(x-i\delta)t} dx}{W(x)}, \quad (86a)$$

$$c_1(t) = \sum_{j=1}^2 S_j U_j e^{i(v_j+\delta)t} + \frac{e^{i\pi/4}}{\pi} \int_0^\infty \frac{f_1(x) e^{-(x-i\delta)t} dx}{W(x)}, \quad (86b)$$

where

$$S_j = \frac{2v_j}{(v_j - v_l)(v_j - v_m)(v_j - v_n)}, \quad (87a)$$

$$(l, m, n = 1, \dots, 4, j \neq l \neq m \neq n),$$

$$\rho = \alpha[c_2(0) - c_1(0)], \quad (87b)$$

$$T_j = (v_j^2 - \delta)c_2(0) + v_j \rho$$

$$= (v_j^2 + \alpha v_j - \delta)c_2(0) - \alpha v_j c_1(0), \quad (87c)$$

$$U_j = (v_j^2 + \delta)c_1(0) - v_j \rho$$

$$= (v_j^2 + \alpha v_j + \delta)c_1(0) - \alpha v_j c_2(0), \quad (87d)$$

$$f_2(x) = [-\rho(x^2 + \delta^2) + 2\alpha c_2(0)(x + i\delta)x]\sqrt{x}, \quad (87e)$$

$$f_1(x) = [\rho(x^2 + \delta^2) + 2\alpha c_1(0)(x - i\delta)x]\sqrt{x}, \quad (87f)$$

$$W(x) = (x^2 + \delta^2)^2 + i4\alpha^2 x^3. \quad (87g)$$

Here v_j ($j = 1, \dots, 4$) are the roots of the quartic $x^4 + 2\alpha x^3 - \delta^2 = 0$ given by [159]

$$v_{1,3} = -\sigma_1/2 \pm \sqrt{(\sigma_1/2)^2 - \xi_2}, \quad (88a)$$

$$v_2 = v_4^* = -\sigma_2/2 - i\sqrt{\xi_1 - (\sigma_2/2)^2}, \quad (88b)$$

$$\sigma_{1,2} = \alpha \pm \sqrt{\alpha^2 + u}, \quad (88c)$$

$$\xi_{1,2} = u/2 \pm \sqrt{(u/2)^2 + \delta^2}, \quad (88d)$$

$$u = -(2\alpha^2 \delta^2)^{1/3} [(A+1)^{1/3} - (A-1)^{1/3}], \quad (88e)$$

$$A = [1 + (4/27)(2\delta/\alpha^2)^2]^{1/2}. \quad (88f)$$

Roots v_1 and v_3 are both real, whereas roots v_2 and v_4 are complex conjugates of each other. We have dropped the global phase factor $e^{i\delta t}$ from the right-hand sides of equations (86a) and (86b), since such a phase factor does not play a role in physical predictions.

The solutions (86a) and (86b) for the amplitudes $c_{1,2}(t)$ show that (a) the spontaneous emission is oscillatory and (b) each of the upper levels splits into two dressed states analogous to vacuum-field Rabi splitting in a high- Q cavity [43]. The splitting is solely due to the interaction of the atom with the photon reservoir, since there is no driving field. Furthermore, (c) there is a fractionalized steady-state population on each of the upper levels as a result of the localization of light in the vicinity of the emitting atom, and (d) quantum interference leads to non-zero steady-state population on level |2) even when it lies outside the PBG (but not far from the band edge). This reveals an important distinction between the realistic anisotropic PBG model and the isotropic dispersion model [160]. In the anisotropic model, spontaneous emission from level |2) (outside of the PBG) can be inhibited by quantum interference with level |1) (inside the PBG). This inhibition does not occur in the absence of the coupling to level |1). In the isotropic model, inhibition of spontaneous emission from level |2) occurs even in the absence of coupling to level |1).

In figure 18 we plot, using the expressions (86a) and (86b), the atomic populations $n_{1,2}(t)$ as functions of the scaled time

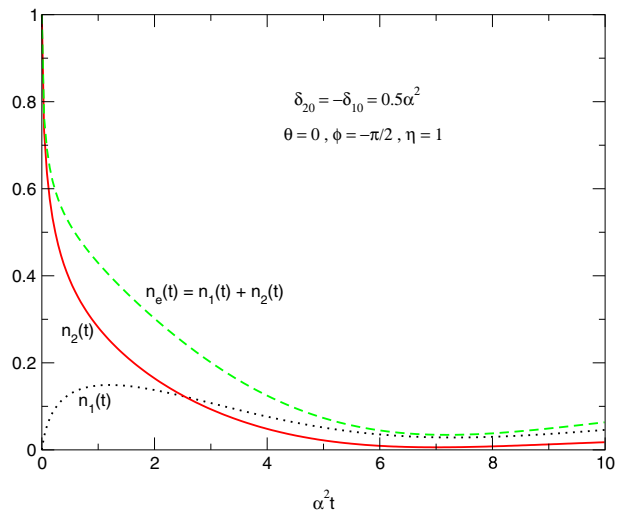


Figure 18. V -system atomic populations $n_2(t)$, $n_1(t)$, and total excited-state population $n_e(t) = n_2(t) + n_1(t)$ as functions of the scaled time $\alpha^2 t$ in the PBG quantum beats problem ($\Omega = 0$) for the initial condition $\theta = 0$ (i.e. atom initially on level |2)) and for $\phi = -\pi/2$ and $\eta = 1$. The anisotropic band edge is midway between the two upper levels with detuning $\delta_{20} = -\delta_{10} = 0.5\alpha^2$. Note that, as a result of quantum interference between the two allowed transitions, the population of level |1) (which was initially zero) increases from zero to a maximum before it settles down to a steady-state value of about 0.05.

$\alpha^2 t$ assuming that, initially, the atom was on level |2). As a result of quantum interference between the two allowed transitions, the population of level |1) (which was initially zero) increases from zero to a maximum before it settles down to a steady-state value. Similar oscillations occur in free-space quantum beats (equations (73)). The major difference is the non-zero steady-state populations in the PBG case. These steady-state populations are given by

$$n_{2s} = |S_1 T_1|^2, \quad n_{1s} = |S_1 U_1|^2, \quad (89)$$

and depend on the parameters θ , ϕ and δ . Figure 19 shows n_{2s} as a function of the detuning δ , for different values of θ . We notice that, even in the absence of a driving field which couples level |2) to the photon atom bound state associated with level |2), there is a steady-state population on level |2), provided that it is not far from the upper band edge ω_c . In other words, *quantum interference allows the partial inhibition of spontaneous emission even in the normally allowed continuum.*

In order to see the detailed differences between the isotropic and anisotropic model dispersion relations (equations (44) and (45), respectively), we plot in figure 20 the populations $n_{1,2}(t)$ in the PBG quantum beats problem for the isotropic dispersion model, assuming that the atom was initially on level |2). Apart from the difference in timescales, the main distinction between the two models is that interference of spontaneous emission between the two allowed transitions and the localization effects of the PBG are considerably enhanced for the isotropic model relative to the anisotropic model. This enhancement is an artifact of the singular photon density of states at the isotropic band edge.

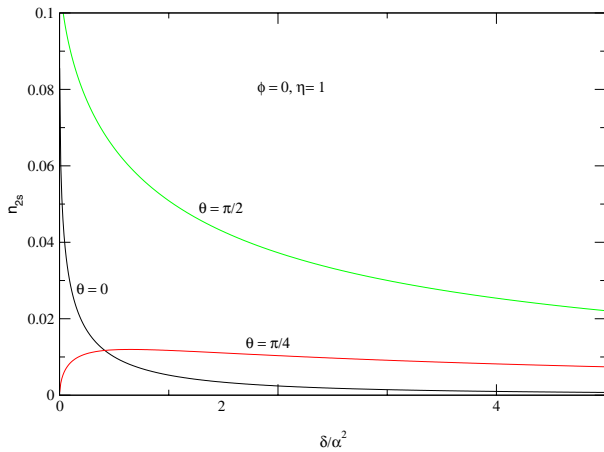


Figure 19. Steady-state population n_{2s} of level $|2\rangle$ as a function of the detuning δ from the anisotropic 3D band edge in the quantum beats problem ($\Omega = 0$), for $\phi = 0$, $\eta = 1$ and for different values of θ . That $n_{2s} \neq 0$ for $\delta > 0$ (that is, when level $|2\rangle$ lies outside the gap) shows that quantum interference with the transition $|1\rangle \rightarrow |0\rangle$ (which lies inside the gap) leads to partial inhibition of spontaneous emission even in the normally allowed continuum.

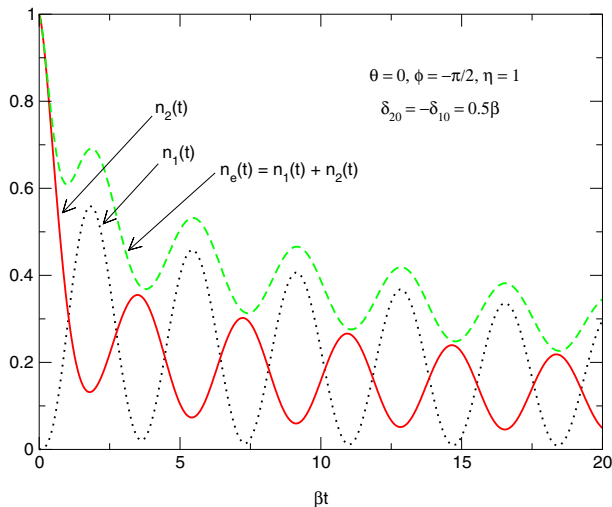


Figure 20. V -system atomic populations $n_2(t)$, $n_1(t)$, and total excited-state population $n_e(t) = n_2(t) + n_1(t)$ as functions of the scaled time βt in the PBG quantum beats problem ($\Omega = 0$) for the isotropic dispersion model (44). The quantities θ , ϕ , δ_{20} , δ_{10} , and η are the same as those in figure 18, which is the corresponding figure for the anisotropic dispersion model (45). Clearly visible are the vacuum Rabi oscillations and the fractional localization near the photonic band edge. These oscillations and localization are considerably enhanced for the isotropic model relative to the anisotropic model.

In the isotropic model, the populations oscillate for hundreds of cycles before decaying to their final larger steady-state values. The amplitudes of these oscillations depend on the initial values $c_2(0)$ and $c_1(0)$.

4.3.2. Coherent control near the edge of a PBG. The coherent control problem corresponds to the case when $\Omega \neq 0$ in equations (84a) and (84b). In this case the equations do not have simple analytic solutions. They must be solved numerically. For illustration purpose it is simpler to use the isotropic rather than the anisotropic model. The Green

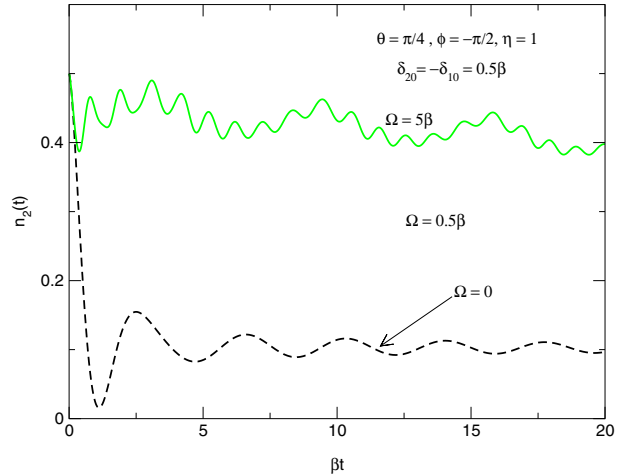


Figure 21. V -system atomic population $n_2(t)$ as a function of the scaled time βt in the PBG (including spontaneous emission channels which go beyond the leading approximation) for $\theta = \pi/4$, $\phi = -\pi/2$, and for various values of Ω . The isotropic band edge is midway between the two upper levels with detuning $\delta_{20} = -\delta_{10} = 0.5\beta$, and $\eta = 1$. For $\Omega \neq 0$, $n_2(t)$ displays rapid oscillations within a slowly varying envelope. The frequency of the oscillations within the envelope increases with Ω .

function $G_{lm}(t - t')$ of the isotropic model (equation (B.19)) exhibits an integrable square root singularity [165] at $t = t'$, whereas the complete Green function in the anisotropic model, which also has an integrable square root singularity at $t = t'$, is rather cumbersome [158].

Figure 21 depicts the PBG coherent control problem for the isotropic dispersion model (44), with the additional spontaneous emission effects included. Note that, for $\Omega \neq 0$, $n_2(t)$ displays rapid oscillations within a relatively slowly varying envelope. When $\Omega \neq 0$, there are two causes for the oscillations of $n_2(t)$. The first one (slow oscillations) is the quantum interference between the two allowed transitions ($|2\rangle \rightarrow |0\rangle$ and $|1\rangle \rightarrow |0\rangle$), as in the quantum beats problem. Superimposed on this is the exchange of populations between levels $|2\rangle$ and $|1\rangle$ caused by the driving field (rapid oscillations). As Ω increases the amplitude of the envelope oscillations decreases but the frequency of the oscillations within the envelope increases. Moreover, the steady-state value n_{2s} increases with Ω . In fact for large Ω , $n_2(t)$ changes little from its initial value $n_2(0)$ even though ω_{20} lies slightly outside the gap ($\delta_{20} = 0.5\beta$). This is because, when Ω is large, level $|2\rangle$ will be strongly coupled to level $|1\rangle$ which lies inside the gap ($\delta_{10} = -0.5\beta$).

In figure 22 we plot the magnitude $|n_c(t)|$ of the coherence $n_c(t)$ as a function of the scaled time βt for different values of Ω . The scale factor β , given by equation (B.22), is of the order $\beta \sim 10^{10} s^{-1}$ at optical frequencies, and, therefore, is larger than the normal vacuum Lamb shift of ($\sim 10^9$ Hz) of the $2p_{1/2}$ level of hydrogen relative to the $2s_{1/2}$ level. Comparing figure 22 with figure 15, we see that, just as in the case of the populations $n_{1,2}(t)$, the spontaneous emission channel $|1\rangle \rightarrow |0\rangle$ introduces further oscillations to the coherence $n_c(t)$ over and above those induced by the driving field. Nevertheless, we obtain non-zero steady-state coherences (and populations) as long as level $|2\rangle$ is not detuned far outside the gap.

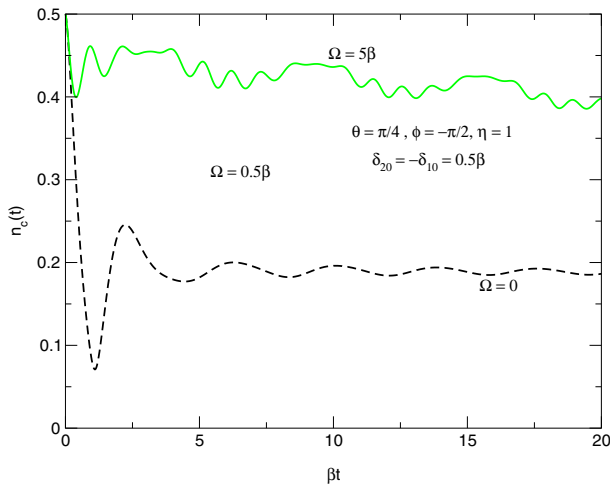


Figure 22. V -system coherence $|n_c(t)| = |c_2(t)c_1^*(t)|$ between levels $|2\rangle$ and $|1\rangle$ as functions of the scaled time βt for $\theta = \pi/4$, $\phi = -\pi/2$, and for various values of Ω . The isotropic band edge is midway between the two upper levels with detuning $\delta_{20} = -\delta_{10} = 0.5\beta$, and $\eta = 1$.

The results in this section are qualitatively similar to those in section 3.4.2 where spontaneous emission on the transition $|1\rangle \rightarrow |0\rangle$ is neglected. The incorporation of the decay channel $|1\rangle \rightarrow |0\rangle$, together with the use of the isotropic dispersion relation, leads to additional oscillations in the transient dynamics. However, it does not alter the presence of non-zero steady-state populations and coherences on the upper levels nor does it alter the ability to control these steady-state populations and coherences by the intensity and phase of the driving field.

4.4. Higher-order radiative and non-radiative interactions

As discussed in section 3.4.2, an excited atom in a PBG interacts strongly with its own radiation field, leading to the formation of the photon–atom bound state, in which the photon emitted by the excited atom can tunnel through the dielectric host on a length scale given by the localization length ξ_{loc} before being Bragg-reflected back to the emitting atom. The result is a stationary-state superposition of a localized photon and a partially excited atom as manifested by the non-zero fractionalized steady-state population given by equations (58) and (89).

Inside a PBG, single-photon spontaneous emission is inhibited. Thus the photon–atom bound state can decay only by other relaxation mechanisms [166, 167]. One such mechanism is spontaneous two-photon emission. This may be relevant for the case of a cold atom which has been optically trapped in the void regions of the PBG material and, therefore, is not in mechanical contact with the vibrational degrees of freedom of the dielectric host. For a dipole-allowed transition such as the $|1\rangle \rightarrow |0\rangle$ transition in a V system (figure 9(a)), two-photon decay yields a lifetime for the photon–atom bound state on the scale of days [6], if the transition lies in the visible spectrum. On the other hand, for a dipole-forbidden transition such as the $|1\rangle \rightarrow |0\rangle$ in the Λ configuration (figure 9(b)), two-photon emission may occur by means of a pair of dipole transitions

which occurs considerably faster. For instance, the $2s \rightarrow 1s$ transition in hydrogen occurs in $1/7$ s.

For an impurity atom embedded in a solid dielectric host, the vibrational modes of the host can provide an alternative relaxation mechanism for the photon–atom bound state by altering the electronic spectrum of the impurity [6]. Next we give a simple semi-quantitative discussion of phonon relaxation for the V system depicted in figure 9(a). In a semiclassical picture, phonon interactions cause the energy levels of an atom to experience small, random, time-varying, Stark shifts. In our simplified picture, we assume that this phenomenon can be modelled by adding random shifts $\delta\omega_{j0}(t)$ to the transition frequencies ω_{j0} . The random functions $\delta\omega_{j0}(t)$ are as often positive as negative and hence the ensemble averages $\langle\delta\omega_{j0}(t)\rangle$ are zero. Thus we can simulate phonon interaction by Gaussian random variables $\delta\omega_{j0}$ of zero mean and variance γ , whose value depends on the strength of these interactions. We assume that the phonon reservoir is Markovian [14] so that the averages of the products $\langle\delta\omega_{j0}(t)\delta\omega_{j0}(t')\rangle$ are zero unless $t \approx t'$. We also assume that variations in $\delta\omega_{j0}(t)$ are very rapid compared to other changes in the system which occur on the timescale $1/\gamma_{j0}$ (where γ_{j0} is the free-space spontaneous emission rate for the transition $|j\rangle \rightarrow |0\rangle$), and take

$$\langle\delta\omega_{j0}(t)\delta\omega_{j0}(t')\rangle = \gamma_{j0d}\delta(t-t'), \quad (j = 1, 2) \quad (90)$$

where γ_{j0d} are the dephasing rates. These dephasing rates are of the order of the Debye frequency ω_D of the crystal which is a measure of the maximum photon frequency in the crystal [17]. For silicon $\omega_D \approx 1.25 \times 10^{13}$ Hz whereas for germanium $\omega_D \approx 7.2 \times 10^{12}$ Hz. Thus, when phonon interactions are taken into account, equations (84a) and (84b) have to be rewritten with δ_{j0} and ω_{21} replaced by, respectively, $\delta_{j0} + \delta\omega_{j0}(t)$ and $\omega_{21} + \delta\omega_{20}(t) - \delta\omega_{10}(t)$, where δ_{j0} , and ω_{21} are the corresponding quantities in the absence of random Stark shifts. For example, if δ_{20} is set to zero, it means that, in the absence of Stark shifts, the transition frequency ω_{20} coincides with the photonic band edge ω_c and, therefore, the shifts $\delta\omega_{20}(t)$ slightly detune level $|2\rangle$ in and out of the band gap in a random fashion.

Figure 23 depicts the excited-state population $n_2(t)$ on level $|2\rangle$ as a function of the scaled time βt for $\delta_{20} = -\delta_{10} = 0.5\beta$, and for different values of Ω , when $\delta\omega_{20}(t)$ and $\delta\omega_{10}(t)$ are taken as Gaussian random variables of zero mean and 0.5β variance. These and other numerical simulations show that, even when the dephasing rate γ_{20d} is comparable to β , the phase-sensitive memory effects which we obtained without including dephasing effects can be recaptured provided that the external Rabi frequency Ω is large compared to the dephasing rate. In other words, *dephasing effects simply determine the minimum required intensity of the external laser field for achieving coherent control of radiative dynamics*. The effect of the random shifts of the atomic levels $|1\rangle$ and $|2\rangle$ on the coherence $n_c(t)$ between the levels is shown in figure 24. We see that, just in the case of the populations, these effects can be offset by intense driving fields.

4.5. Physical realization of the model system

Our model system consist of a three-level atom located inside a PBG material. There are several ways of placing

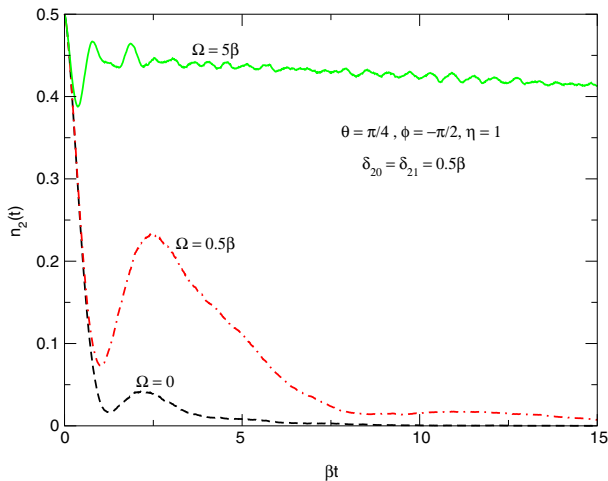


Figure 23. V -system excited-state population $n_2(t)$ on level $|2\rangle$ near the isotropic photonic band edge as a function of the scaled time βt for $\theta = \pi/4$, $\phi = -\pi/2$, and for different values of Ω , in the presence of dipolar dephasing Gaussian random Stark shifts $\delta\omega_{20}(t)$ and $\delta\omega_{10}(t)$ (each of zero mean and 0.5β variance) of the transition frequencies ω_{20} and ω_{10} . In the absence of the random Stark shifts, the band edge is assumed to be midway between the two upper levels with detuning $\delta_{20} = -\delta_{10} = 0.5\beta$. Compare this figure with the corresponding figure (figure 21) in the absence of phonon-mediated dephasing.

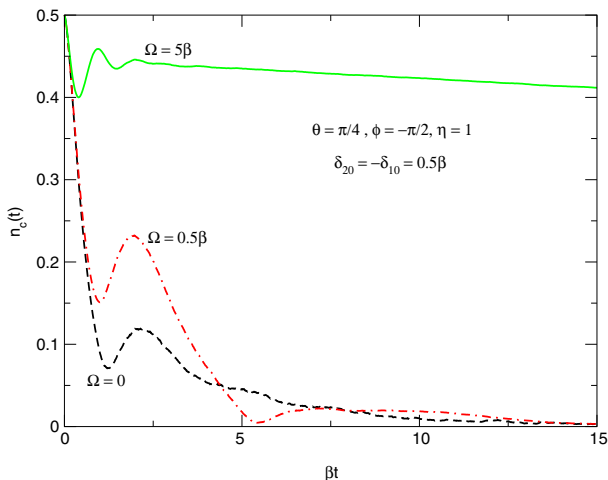


Figure 24. V -system coherence $n_c(t) = |c_2(t)c_1^*(t)|$ between levels $|2\rangle$ and $|1\rangle$ near the isotropic photonic band edge as a function of the scaled time βt for $\theta = \pi/4$, $\phi = -\pi/2$, and for different values of Ω , in the presence of dipolar dephasing Gaussian random Stark shifts $\delta\omega_{20}(t)$ and $\delta\omega_{10}(t)$ (each of zero mean and 0.5β variance) of the transition frequencies ω_{20} and ω_{10} . In the absence of the random Stark shifts, the band edge is assumed to be midway between the two upper levels with detuning $\delta_{20} = -\delta_{10} = 0.5\beta$. Compare this figure with the corresponding figure (figure 22) in the absence of phonon-mediated dephasing.

such an atom inside a PC. From a material standpoint, it is possible to dope an existing PBG material using ion beam implantation methods. For instance, it has recently been shown that Er^{3+} ions implanted into bulk silicon exhibit sharp free-atom-like spectra [173–176]. Intense PL at $1.54 \mu\text{m}$ is observed in the system at low temperatures (when the host material is crystalline, Er-related PL is quenched at temperatures above 80 K so that it cannot be detected at room

temperatures). This wavelength is particularly significant because it corresponds to the minimum absorption of silica fibre-based optical communication system. Because the PL at $1.54 \mu\text{m}$ is due to the spin-orbit split $^4I_{13/2} \rightarrow ^4I_{15/2}$ of 4f electrons in the Er^{3+} ions which are shielded by outer $5s^25p^6$ shells, the influence of the host lattice on the luminescence wavelength is weak. (The key to the success of erbium is that the upper level of the amplifying transition $^4I_{13/2}$ is separated by a large energy gap from the next-lowest level $^4I_{15/2}$ so that its lifetime is very long and mostly radiative. The value of the lifetime is around 10 ms and varies depending on the host and erbium concentration.) It would be of considerable interest to study the radiative properties of Er^{3+} ions implanted into a 3D silicon PBG material in which a PBG is engineered to occur at $1.54 \mu\text{m}$. In spite of the screening of the atomic transition by the outer shells, it is likely that thermal phonons in the silicon host would cause significant dephasing of the quantum degrees of freedom within the erbium 4f shell. Consequently, such a system must be cooled to liquid helium temperatures.

Alternatively, our model system may be realized by trapping cold atoms in the void regions of a PC. The trapping may be achieved by using the properties of the electromagnetic eigenmodes of a 3D PBG material. If the PBG material is illuminated by an intense laser field with frequency near the bottom of the ‘air’ band, a nearly standing wave electromagnetic field will arise with strong electric field gradients and peak intensities that lie in the void fraction of the material. This field distribution will act as an optical trapping potential for a dilute atomic vapour pumped into the void region of the crystal [107]. This will trap atoms in the void regions of the PC where the field is most intense and prevent the atoms from colliding with the dielectric backbone of the PBG material. In a typical 3D PBG material, the void fraction forms a connected network that accounts for nearly 75% of the volume of the material. Atoms which are optically trapped in this extensive void network will be immune to collisional dephasing and decoherence phenomena arising from direct interaction with atoms in the solid dielectric backbone. Doppler broadening due to the random motion of the gas molecules may be partially alleviated by laser cooling techniques [177].

A third approach to realize our model system is by means of an ‘artificial atom’ or QD structure embedded in the solid fraction of the PBG material. Semiconductor QDs are nanoscale quantum structures that allow electronic properties to be tailored through quantum confinement. They exhibit distinctive features similar to atoms such as atomic-like excitation spectra with discrete and extremely sharp spectral lines [178]. With their well-defined localized states, QDs offer the possibility of coherent manipulation of a single localized quantum system in a way similar to that achieved in atoms but with the technological advantages of a solid-state system.

5. Conclusions

In this paper the quantum electrodynamic properties of a three-level atom embedded in a PBG material were investigated. Specifically, the combined effects of coherent control by an external driving field and photon localization facilitated by a PBG on spontaneous emission from a three-level atom

embedded in a PBG material were investigated. It was demonstrated that quantum information is stored in the model system considered, and that the nature of this information is strongly dependent on the detuning of the atomic levels from the upper band edge, on the initial coherent superposition state, on the intensity of the control laser driving the transition $|2\rangle \leftrightarrow |1\rangle$, and the relative phase between the control laser field and the pumping laser pulse used to prepare the initial state. In particular, the steady-state populations and coherences keep memory of the relative phase as well as the intensity and phase of the pumping laser pulse suggesting a possible application as an *atomic-scale optical memory device*. Moreover, since both populations and coherences can be maintained between the two upper atomic levels $|1\rangle$ and $|2\rangle$, these levels can be used as a *qubit* (two-state quantum system) to encode information for quantum computation. Two or more such systems can be used to construct quantum logic gates [171, 172].

The influences of other spontaneous emission terms and non-radiative effects on the results found in section 3 were investigated in section 4, using the V configuration as an example. The inclusion of the spontaneous emission channel $|1\rangle \rightarrow |0\rangle$ leads to quantum interference between the two allowed transitions $|2\rangle \rightarrow |0\rangle$ and $|1\rangle \rightarrow |0\rangle$ which induces further oscillations to the populations and coherences over and above those induced by the driving field. Moreover, in the absence of a driving field coupling levels $|2\rangle$ and $|1\rangle$, quantum interference between the two allowed transitions $|2\rangle \rightarrow |0\rangle$ and $|1\rangle \rightarrow |0\rangle$ leads to the partial inhibition of spontaneous emission even in the normally allowed continuum. However, the inclusion of the spontaneous emission channel $|1\rangle \rightarrow |0\rangle$ does not alter the presence of non-zero steady-state populations and coherences on the upper levels, nor does it alter the ability to control these steady-state populations and coherences by the intensity and phase of the driving field.

Phonon dephasing is a relevant decay mechanism for the photon atom bound state in the case of impurity atoms embedded in the solid fraction of the PBG material. Such dephasing effects can be offset by making the Rabi frequency of the control laser field large compared to the dephasing rates.

In both sections 3 and 4 we employed the effective mass dispersion relation (45) or (44). While the effective mass approximation gives qualitatively correct physics [6], an investigation of our model system using a full anisotropic dispersion relation of a realistic band structure is a worthy undertaking [12, 170]. This would involve a realistic evaluation of the Green function [67] using the full dispersion relation ω_k appropriate to a real PC (see for instance equation (B.5)). The resulting equations of motion for radiative dynamics would then need to be solved numerically.

An experimental realization of a quantum computer requires both

- (a) isolated quantum systems that act as qubits, and
- (b) the presence of controlled interaction between the qubits that allows for construction of *quantum logic gates*.

Thus, it is useful to investigate the coherent control of spontaneous emission, not from a single three-level atom, but from two neighbouring three-level atoms coupled via resonant dipole–dipole interaction. Quantitative results on the energy transfer between the two atoms found from such an

investigation may give us a qualitative picture on the effects of the presence of many atoms within a cubic wavelength of the atom of interest.

Acknowledgments

I (MW) owe deep gratitude to my PhD supervisor, Professor Sajeev John, for giving me the opportunity to explore and explain a small part of the rich and exciting field of PBG materials. I would like to gratefully acknowledge Dr Tran Quang who contributed significantly to this paper by ways of collaboration, suggestions, and comments. Special thanks are also due to my colleagues N Vats, O Toader and M Florescu. This work was supported in part by grants to S John from the Natural Sciences and Engineering Research Council (NSERC) of Canada, Photonics Research Ontario (PRO), and the New Energy and Industrial Technology Development Organization (NEDO) of Japan. MW received financial support from the Department of Physics in the form of a University of Toronto Open Fellowship.

Appendix A. Hamiltonian of a three-level atom interacting with a quantized radiation field

In this appendix we derive the Hamiltonian of a three-level atom interacting with a quantized electromagnetic field in the electric dipole and in the RWAs.

A.1. Operator description of isolated atoms

Consider an isolated atom with no radiation present. Such an atom is described by a Hamiltonian operator H_a which is a function of both the position \mathbf{r} , and the momentum \mathbf{p} of the constituent particles of the atom, and has no explicit time dependence. This Hamiltonian satisfies the eigenvalue equation

$$H_a|i\rangle = \hbar\omega_i|i\rangle, \quad (\text{A.1})$$

where $\hbar\omega_i$ are the energy eigenvalues and $|i\rangle$ are the eigenvectors. The states $|i\rangle$ span the Hilbert space of the atomic system. Since H_a is an observable, its basis vectors $\{|i\rangle\}$ form a complete orthonormal set [156] as expressed by the *closure* (*completeness*) and *orthonormality* relations

$$\sum_i |i\rangle\langle i| = 1, \quad \langle i|j\rangle = \delta_{ij}, \quad (\text{A.2})$$

where 1 represents the identity operator, and δ_{ij} is the Kronecker delta function ($\delta_{ij} = 1$ for $i = j$, and $\delta_{ij} = 0$ for $i \neq j$). We define the atomic operator σ_{ij} by

$$\sigma_{ij} \equiv |i\rangle\langle j|. \quad (\text{A.3})$$

These operators provide the multilevel generalization of Dicke's spin operators for two-level atoms [168, 169]. From the orthonormality relation (A.2) we obtain

$$\sigma_{ij}|k\rangle = \delta_{jk}|i\rangle, \quad (\text{A.4})$$

which, in turn, leads to the commutation relation

$$[\sigma_{ij}, \sigma_{lk}] = \sigma_{ik}\delta_{jl} - \sigma_{lj}\delta_{ki}. \quad (\text{A.5})$$

The operator σ_{ij} acting on level $|j\rangle$ transforms it to level $|i\rangle$, and, therefore, is a raising (lowering) operator for $i > j$ ($i < j$). On the other hand, the operator $\sigma_{ii} = |i\rangle\langle i|$ gives the population of level $|i\rangle$, that is, the probability to find the atom on level $|i\rangle$.

Using equation (A.1) and the closure relation (A.2), we can expand the atomic Hamiltonian H_a in terms of the atomic operators σ_{ij} as

$$H_a = H_a \sum_i |i\rangle\langle i| = \sum_i H_a |i\rangle\langle i| = \hbar \sum_l \omega_l \sigma_{li}. \quad (\text{A.6})$$

Similarly, by using the closure relation twice, any operator $Q(\mathbf{p}, \mathbf{r})$ which is a function of \mathbf{p} and \mathbf{r} can be expanded in terms of the atomic operators σ_{ij} as

$$Q = \left(\sum_i |i\rangle\langle i| \right) Q \left(\sum_j |j\rangle\langle j| \right) = \sum_{i,j} Q_{ij} \sigma_{ij}, \quad (\text{A.7})$$

where the expansion coefficients $Q_{ij} = \langle i|Q|j\rangle$ are just the matrix elements of Q in the energy representation. If Q is Hermitian (as any observable should be), we have $Q_{ij} = Q_{ji}^*$.

A.2. Minimal coupling Hamiltonian

Consider an atom interacting with a radiation field represented by a vector potential \mathbf{A} . For simplicity, the source of the radiation field (charges and currents) is not considered. We also assume the atom to have a single electron of charge e and mass m in a potential $V(\mathbf{r})$, where \mathbf{r} is the position vector of the electron. The momentum conjugate to \mathbf{r} is [32]

$$\mathbf{p} = m \frac{d\mathbf{r}}{dt} + e\mathbf{A}. \quad (\text{A.8})$$

We choose to work in the Coulomb gauge which is defined by the condition

$$\nabla \cdot \mathbf{A} = 0, \quad (\text{A.9})$$

and has particular advantages for slowly moving particles in bound states [32].

The non-relativistic *minimal coupling* Hamiltonian for a one-electron atom interacting with the electromagnetic radiation field may be written in mks units as [32, 35]

$$H = \frac{1}{2m} (\mathbf{p} - e\mathbf{A})^2 + eV(\mathbf{r}) + H_r. \quad (\text{A.10})$$

In the Coulomb gauge (A.9), we may write (A.10) as

$$H = \frac{\mathbf{p}^2}{m} + eV(\mathbf{r}) + H_r - \frac{e}{m} \mathbf{A} \cdot \mathbf{p} + \frac{e^2}{2m} \mathbf{A}^2. \quad (\text{A.11})$$

The first two terms in the right-hand side of equation (A.11) give the Hamiltonian H_a of the free atom

$$H_a = \frac{\mathbf{p}^2}{2m} + eV(\mathbf{r}), \quad (\text{A.12})$$

which is also given by equation (A.6) in terms of its stationary states $\{|i\rangle\}$. The third term H_r in equation (A.11) represents the energy of the quantized (source-free) radiation field in the absence of the atom. It is given by

$$H_r = \sum_{\mathbf{k}, \lambda} \hbar \omega_{\mathbf{k}} (a_{\mathbf{k}\lambda}^\dagger a_{\mathbf{k}\lambda} + 1/2), \quad (\text{A.13})$$

where \mathbf{k} and $\lambda (= 1, 2)$ represent, respectively, the wavevector and the polarization index for the mode $\{\mathbf{k}\lambda\}$ of the radiation field. The operators $a_{\mathbf{k}\lambda}$ and $a_{\mathbf{k}\lambda}^\dagger$ are, respectively, the Schrödinger-picture annihilation and creation operators for mode $\{\mathbf{k}\lambda\}$ of the field obeying the commutation rules

$$\begin{aligned} [a_{\mathbf{k}\lambda}, a_{\mathbf{k}'\lambda'}] &= 0, & [a_{\mathbf{k}\lambda}^\dagger, a_{\mathbf{k}'\lambda'}^\dagger] &= 0, \\ [a_{\mathbf{k}\lambda}, a_{\mathbf{k}'\lambda'}^\dagger] &= \delta_{\mathbf{k}\mathbf{k}'} \delta_{\lambda\lambda'}. \end{aligned} \quad (\text{A.14})$$

In equation (A.13), the term $1/2 \sum_{\mathbf{k}, \lambda} \hbar \omega_{\mathbf{k}}$ accounts for the ground state or *zero-point* energy of the quantized radiation field. This energy is a constant, albeit infinite, and therefore has no effect whatsoever on the system dynamics. Thus it can be dropped out of the Hamiltonian H_r , which is tantamount to shifting the energy origin. Accordingly we write

$$H_0 \equiv H_a + H_r = \sum_i \hbar \omega_i \sigma_{ii} + \sum_{\mathbf{k}, \lambda} \hbar \omega_{\mathbf{k}} a_{\mathbf{k}\lambda}^\dagger a_{\mathbf{k}\lambda} \quad (\text{A.15})$$

as the Hamiltonian of the *unperturbed* system.

The fourth term in equation (A.11), which is of first order in the coupling constant e , we denote by

$$H_1 = -\frac{e}{m} \mathbf{A} \cdot \mathbf{p}. \quad (\text{A.16})$$

This term represents the interaction between the electron momentum \mathbf{p} and the radiation field \mathbf{A} . It is small compared with H_a and H_r , but is large compared with the last term which is of order e^2 . This last term is denoted by

$$H_2 = \frac{e^2}{2m} \mathbf{A}^2. \quad (\text{A.17})$$

It represents the energy of mutual interaction between different modes of the radiation field through the coupling of the electron to the field. In this paper we neglect the small term H_2 , and take the total Hamiltonian of the atom–field system to be

$$H = H_0 + H_1 = \sum_i \hbar \omega_i \sigma_{ii} + \sum_{\mathbf{k}, \lambda} \hbar \omega_{\mathbf{k}} a_{\mathbf{k}\lambda}^\dagger a_{\mathbf{k}\lambda} + H_1. \quad (\text{A.18})$$

The Hamiltonian (A.11) is given in the Schrödinger picture, where observables are represented by stationary (time-independent) operators. In this picture, the vector potential $\mathbf{A}(\mathbf{r})$ may be expanded in plane waves of mode $\{\mathbf{k}\lambda\}$ as [32]

$$\mathbf{A}(\mathbf{r}) = \sum_{\mathbf{k}, \lambda} \left(\frac{\hbar}{2\epsilon_0 \omega_{\mathbf{k}} V} \right)^{1/2} \hat{\mathbf{e}}_{\mathbf{k}\lambda} (a_{\mathbf{k}\lambda} e^{i\mathbf{k}\cdot\mathbf{r}} + a_{\mathbf{k}\lambda}^\dagger e^{-i\mathbf{k}\cdot\mathbf{r}}). \quad (\text{A.19})$$

Here V represents the quantization volume, ϵ_0 the Coulomb constant, and $\hat{\mathbf{e}}_{\mathbf{k}\lambda}$ are the two transverse (polarization) unit vectors satisfying

$$\hat{\mathbf{k}} \cdot \hat{\mathbf{e}}_{\mathbf{k}\lambda} = 0, \quad \hat{\mathbf{e}}_{\mathbf{k}\lambda} \cdot \hat{\mathbf{e}}_{\mathbf{k}\lambda'} = \delta_{\lambda\lambda'}, \quad (\lambda = 1, 2), \quad (\text{A.20})$$

where $\hat{\mathbf{k}}$ is the unit vector in the direction of \mathbf{k} . The transversality condition $\hat{\mathbf{k}} \cdot \hat{\mathbf{e}}_{\mathbf{k}\lambda} = 0$ expresses the fact that the mode amplitudes are perpendicular to the propagation direction and is a direct consequence of the Coulomb gauge (A.9). On the other hand, condition $\hat{\mathbf{e}}_{\mathbf{k}\lambda} \cdot \hat{\mathbf{e}}_{\mathbf{k}\lambda'} = \delta_{\lambda\lambda'}$ shows that unit vectors $\{\hat{\mathbf{e}}_{\mathbf{k}1}, \hat{\mathbf{e}}_{\mathbf{k}2}, \hat{\mathbf{k}}\}$ form a right-handed triad.

According to equation (A.7), the electron momentum operator \mathbf{p} can be expanded as

$$\mathbf{p} = \sum_{i,j} \mathbf{p}_{ij} \sigma_{ij}, \quad (\text{A.21})$$

where $\mathbf{p}_{ij} = \langle i | \mathbf{p} | j \rangle$. From the commutation relation

$$[H_a, \mathbf{r}] = -\frac{i\hbar}{m} \mathbf{p}, \quad (\text{A.22})$$

we obtain

$$\mathbf{p}_{ij} \equiv \langle i | \mathbf{p} | j \rangle = -\frac{m}{i\hbar} \langle i | [H_a, \mathbf{r}] | j \rangle = \frac{im}{e} \omega_{ij} \mathbf{d}_{ij}, \quad (\text{A.23})$$

where

$$\omega_{ij} = \omega_i - \omega_j \quad (\text{A.24})$$

is the atomic transition frequency between levels $|i\rangle$ and $|j\rangle$, and

$$\mathbf{d}_{ij} = \langle i | e\mathbf{r} | j \rangle \quad (\text{A.25})$$

is the electric dipole moment transition matrix element between states $|i\rangle$ and $|j\rangle$. We have $\mathbf{d}_{ij} \neq 0$, only if levels $|i\rangle$ and $|j\rangle$ are of opposite symmetry so that the transition $|i\rangle \leftrightarrow |j\rangle$ is dipole allowed. In particular, $\mathbf{d}_{ii} = 0$. Using (A.23) in (A.21), we obtain

$$\mathbf{p} = \frac{im}{e} \sum_{i,j} \omega_{ij} \mathbf{d}_{ij} \sigma_{ij}. \quad (\text{A.26})$$

Using (A.26) and (A.19) in (A.16) we obtain

$$H_1 = -\frac{e}{m} \mathbf{A}(\mathbf{r}) \cdot \mathbf{p} = -i\hbar \sum_{\mathbf{k}, \lambda} \sum_{i,j} g_{\mathbf{k}\lambda}^{ij} \sigma_{ij} (a_{\mathbf{k}\lambda} e^{i\mathbf{k}\cdot\mathbf{r}} + a_{\mathbf{k}\lambda}^\dagger e^{-i\mathbf{k}\cdot\mathbf{r}}). \quad (\text{A.27})$$

Here

$$g_{\mathbf{k}\lambda}^{ij} = \frac{\omega_{ij} \mathbf{d}_{ij}}{\hbar} \left(\frac{\hbar}{2\epsilon_0 \omega_{\mathbf{k}} V} \right)^{1/2} \hat{\mathbf{e}}_{\mathbf{k}\lambda} \cdot \hat{\mathbf{d}}_{ij} \quad (\text{A.28})$$

represents the frequency-dependent *coupling constant* between the atomic transition $|i\rangle \rightarrow |j\rangle$ and the mode $\{\mathbf{k}\lambda\}$ of the radiation field. Also \mathbf{d}_{ij} and $\hat{\mathbf{d}}_{ij}$ represent the magnitude and unit vector of the atomic dipole moment \mathbf{d}_{ij} for the transition $|i\rangle \rightarrow |j\rangle$.

In the optical regime of the spectrum where photon wavelengths are long compared to atomic dimensions ($\lambda_{\text{photon}} \sim 10^3 \text{ \AA}$, whereas $r_{\text{atom}} \sim 1 \text{ \AA}$), it is useful to make the *electric dipole approximation* ($\mathbf{k} \cdot \mathbf{r} \approx 0$) in equation (A.27). Using this approximation in equation (A.18) we obtain

$$H = \sum_i \hbar \omega_i \sigma_{ii} + \sum_{\mathbf{k}, \lambda} \hbar \omega_{\mathbf{k}} a_{\mathbf{k}\lambda}^\dagger a_{\mathbf{k}\lambda} - i\hbar \sum_{\mathbf{k}, \lambda} \sum_{i,j} g_{\mathbf{k}\lambda}^{ij} \sigma_{ij} (a_{\mathbf{k}\lambda} + a_{\mathbf{k}\lambda}^\dagger). \quad (\text{A.29})$$

This equation applies to a general n -level atom interacting with a quantized electromagnetic field in the electric dipole approximation. The special case of a three-level atom is considered in the next section.

A.3. The Ξ , Λ , and V configurations

A three-level atom (consisting of the ground level $|0\rangle$ and excited levels $|1\rangle$ and $|2\rangle$) can be in one of three distinct configurations. These are the Ξ (xi) or cascade configuration, the Λ (lambda) configuration, and the V configuration (see figure A.1). Direct dipole transitions are forbidden between levels $|2\rangle$ and $|0\rangle$ for the Ξ system, between levels $|1\rangle$ and $|0\rangle$ for the Λ system, and between levels $|2\rangle$ and $|1\rangle$ for the V system. Thus, each of the three configurations of figure A.1 has two dipole-allowed transitions, and two associated coupling constants. These coupling constants are $g_{\mathbf{k}\lambda}^{21}$ and $g_{\mathbf{k}\lambda}^{10}$ for the Ξ system, $g_{\mathbf{k}\lambda}^{20}$ and $g_{\mathbf{k}\lambda}^{21}$ for the Λ system, and $g_{\mathbf{k}\lambda}^{20}$ and $g_{\mathbf{k}\lambda}^{10}$ for the V system.

The dipole operator is an odd vector operator with vanishing matrix elements between states of the same parity. Thus, $\mathbf{d}_{ij} = 0$ for $i = j$. It follows from equation (A.28) that $g_{\mathbf{k}\lambda}^{ii} = 0$. Thus, for the Ξ configuration, the interaction Hamiltonian (A.27) assumes the form

$$H_1 = -i\hbar \sum_{\mathbf{k}, \lambda} (g_{\mathbf{k}\lambda}^{21} \sigma_{21} + g_{\mathbf{k}\lambda}^{12} \sigma_{12} + g_{\mathbf{k}\lambda}^{10} \sigma_{10} + g_{\mathbf{k}\lambda}^{01} \sigma_{01}) (a_{\mathbf{k}\lambda} + a_{\mathbf{k}\lambda}^\dagger). \quad (\text{A.30})$$

Since the dipole operator $\mathbf{d} = e\mathbf{r}$ is Hermitian we have, $\mathbf{d}_{ij} = \mathbf{d}_{ji}^*$. We also assume that the dipole transition matrix elements \mathbf{d}_{ij} are real, as it is always possible to make them so by choosing the relative phases of the state vectors properly [70]. Then, the coupling constants $g_{\mathbf{k}\lambda}^{ij}$ will also be real, and equation (A.28) shows that $g_{\mathbf{k}\lambda}^{ij} = -g_{\mathbf{k}\lambda}^{ji}$ since, according to equation (A.24), $\omega_{ij} = -\omega_{ji}$. Thus

$$H_1 = -i\hbar \sum_{\mathbf{k}, \lambda} [g_{\mathbf{k}\lambda}^{21} (\sigma_{21} - \sigma_{12}) + g_{\mathbf{k}\lambda}^{10} (\sigma_{10} - \sigma_{01})] (a_{\mathbf{k}\lambda} + a_{\mathbf{k}\lambda}^\dagger). \quad (\text{A.31})$$

Next we invoke the RWA. This approximation admits only processes corresponding to the emission of a photon and the simultaneous lowering of an atomic state, or vice versa. Thus, in the RWA, terms (such as $\sigma_{01} a_{\mathbf{k}\lambda}$ and $\sigma_{10} a_{\mathbf{k}\lambda}^\dagger$) which describe virtual processes of excitation (de-excitation) of the atom with simultaneous creation (annihilation) of a photon are neglected [70]. Under the RWA, equation (A.31) reduces to

$$H_1 = i\hbar \sum_{\mathbf{k}, \lambda} [g_{\mathbf{k}\lambda}^{21} (a_{\mathbf{k}\lambda}^\dagger \sigma_{12} - \sigma_{21} a_{\mathbf{k}\lambda}) + g_{\mathbf{k}\lambda}^{10} (a_{\mathbf{k}\lambda}^\dagger \sigma_{01} - \sigma_{10} a_{\mathbf{k}\lambda})] \quad (\Xi \text{ system}). \quad (\text{A.32})$$

This interaction Hamiltonian is written in a *normal order*, that is to say, in each operator product, the field annihilation and creation operators are placed, respectively, to the extreme right- and left-hand sides. This is possible because of our assumption that the atomic operators always commute with the field operators. The interaction Hamiltonians for the Λ and V configurations are obtained in a similar way:

$$H_1 = i\hbar \sum_{\mathbf{k}, \lambda} [g_{\mathbf{k}\lambda}^{20} (a_{\mathbf{k}\lambda}^\dagger \sigma_{02} - \sigma_{20} a_{\mathbf{k}\lambda}) + g_{\mathbf{k}\lambda}^{21} (a_{\mathbf{k}\lambda}^\dagger \sigma_{12} - \sigma_{21} a_{\mathbf{k}\lambda})] \quad (\Lambda \text{ system}), \quad (\text{A.33a})$$

$$H_1 = i\hbar \sum_{\mathbf{k}, \lambda} [g_{\mathbf{k}\lambda}^{20} (a_{\mathbf{k}\lambda}^\dagger \sigma_{02} - \sigma_{20} a_{\mathbf{k}\lambda}) + g_{\mathbf{k}\lambda}^{10} (a_{\mathbf{k}\lambda}^\dagger \sigma_{01} - \sigma_{10} a_{\mathbf{k}\lambda})] \quad (V \text{ system}). \quad (\text{A.33b})$$

A two-level atom can be treated as a special limiting case of each of the three-level systems, by eliminating one of the

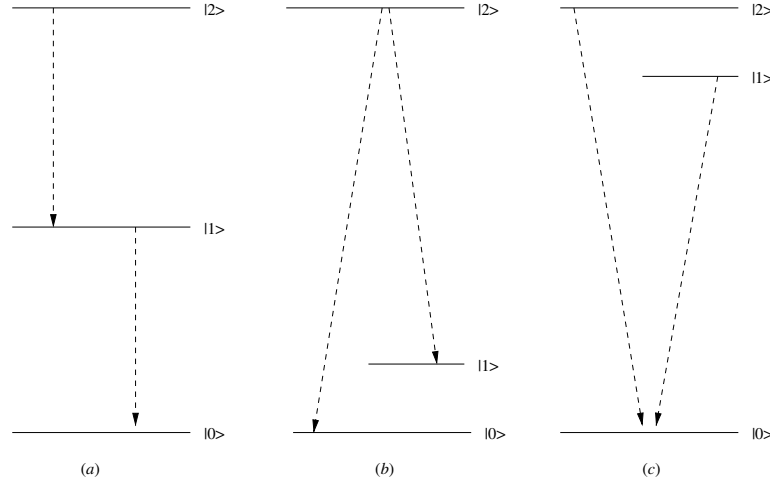


Figure A.1. Schematic representations of a three-level atom (a) in the Ξ or cascade, (b) in the Λ , and (c) in the V configurations. Dashed lines with arrows denote dipole-allowed transitions.

three atomic levels. This can be done, in the Ξ -system for instance, simply by letting the coupling constant $g_{k\lambda}^{21}$ vanish ($g_{k\lambda}^{21} \rightarrow 0$) resulting in a two-level system consisting of $|1\rangle$ and $|0\rangle$. The corresponding interaction Hamiltonian is then

$$H_1 = i\hbar \sum_{k\lambda} g_{k\lambda}^{10} (a_{k\lambda}^\dagger \sigma_{01} - \sigma_{10} a_{k\lambda}). \quad (\text{A.34})$$

Appendix B. Non-Markovian memory kernels

In this appendix the various expressions for the Green functions used in sections 3 and 4 are derived. We start from equation (68)

$$G_{lm}(t-t') = \sum_{k\lambda} g_{k\lambda}^{l0} g_{k\lambda}^{m0} e^{-i\mu_k^{m0}(t-t')}, \quad (l, m = 1, 2), \quad (\text{B.1})$$

where μ_k^{m0} is given by equation (65). When $l = m$, equation (B.1) reduces to (29). Substituting for $g_{k\lambda}^{l0}$ and $g_{k\lambda}^{m0}$ from equation (63) we obtain

$$G_{lm}(t-t') = \frac{\zeta}{V} \sum_{k\lambda} (\hat{e}_{k\lambda} \cdot \hat{d}_{l0}) (\hat{e}_{k\lambda} \cdot \hat{d}_{m0}) \frac{1}{\omega_k} e^{-i\mu_k^{m0}(t-t')}, \quad (\text{B.2})$$

where

$$\zeta = \sqrt{\left(\frac{\omega_{l0}^2 d_{l0}^2}{2\hbar \epsilon_0} \right) \left(\frac{\omega_{m0}^2 d_{m0}^2}{2\hbar \epsilon_0} \right)}. \quad (\text{B.3})$$

Assuming that the modes of the field are closely spaced in frequency, we make the continuum approximation for the field modes and replace the summation over \mathbf{k} by an integral:

$$\sum_{\mathbf{k}} \rightarrow \frac{V}{(2\pi)^3} \int d^3 \mathbf{k}, \quad (\text{B.4})$$

where $d^3 \mathbf{k} \equiv k^2 dk d\Omega$, $d\Omega$ being the space angle element. Thus

$$G_{lm}(t-t') = \frac{\zeta}{(2\pi)^3} \frac{8\pi}{3} \int \left[\frac{3}{8\pi} \sum_{\lambda} (\hat{e}_{k\lambda} \cdot \hat{d}_{l0}) (\hat{e}_{k\lambda} \cdot \hat{d}_{m0}) \right] \times \frac{1}{\omega_k} e^{-i(\omega_k - \omega_{m0})(t-t')} d^3 \mathbf{k}. \quad (\text{B.5})$$

This is a general result valid for any dispersion relation ω_k . When the dispersion relation is isotropic (i.e. when ω_k depends only on the magnitude k of \mathbf{k}), equation (B.5) reduces to

$$G_{lm}(t-t') = \frac{\zeta}{(2\pi)^3} \frac{8\pi}{3} \eta_{lm} \int_0^\Lambda \frac{1}{\omega_k} e^{-i(\omega_k - \omega_{m0})(t-t')} k^2 dk, \quad (\text{B.6})$$

where

$$\eta_{lm} = \frac{3}{8\pi} \int \sum_{\lambda} (\hat{e}_{k\lambda} \cdot \hat{d}_{l0}) (\hat{e}_{k\lambda} \cdot \hat{d}_{m0}) d\Omega, \quad (\text{B.7})$$

and $\Lambda = mc/\hbar$ is the Compton wavenumber of the electron. We have introduced the cutoff Λ in the photon wavevector [180] as the contributions of extremely high energy photons cannot be important. The non-relativistic approximation for the electron is not valid for photons of energy $\hbar\omega \sim mc^2$.

We consider a coordinate system defined by the unit vectors $\{\hat{e}_{k1}, \hat{e}_{k2}, \hat{\mathbf{k}}\}$. Defining $\{\alpha_{j0}, \beta_{j0}, \theta_{j0}\}$ as the direction angles of the dipole moment unit vector \hat{d}_{j0} , we obtain

$$\eta_{lm} = \frac{3}{8\pi} \int (\cos \alpha_{l0} \cos \alpha_{m0} + \cos \beta_{l0} \cos \beta_{m0}) d\Omega. \quad (\text{B.8})$$

If the dipoles \hat{d}_{l0} and \hat{d}_{m0} are parallel or antiparallel (so that $\alpha_{l0} = \pm \alpha_{m0} = \alpha$, $\beta_{l0} = \pm \beta_{m0} = \beta$, and $\theta_{l0} = \pm \theta_{m0} = \theta$), the law of direction cosines gives

$$\cos \alpha_{l0} \cos \alpha_{m0} + \cos \beta_{l0} \cos \beta_{m0} = \cos^2 \alpha + \cos^2 \beta = 1 - \cos^2 \theta. \quad (\text{B.9})$$

Using this in equation (B.8) we obtain $\eta_{lm} = 1$. It follows that

$$\eta_{lm} = \delta_{lm} + \eta(1 - \delta_{lm}), \quad (\text{B.10})$$

where δ_{lm} is the Kronecker delta function, and

$$\eta = \frac{3}{8\pi} \int (\cos \alpha_{20} \cos \alpha_{10} + \cos \beta_{20} \cos \beta_{10}) d\Omega. \quad (\text{B.11})$$

Thus $\eta = 1$ for $\hat{d}_{l0} = \pm \hat{d}_{m0}$ (that is, when the dipoles associated with the transitions $|l\rangle \rightarrow |0\rangle$ and $|m\rangle \rightarrow |0\rangle$ are parallel or antiparallel).

For vacuum we use the isotropic dispersion relation $\omega_k = ck$. The emitted radiation is centred about the atomic transition frequency $\omega_k = \omega_{m0}$, and the quantity ω_k varies very little around $\omega_k = \omega_{m0}$. We can, therefore, replace k^2/ω_k in equation (B.6) by ω_{m0}/c^2 and extend the upper limit of integration to ∞ to obtain

$$G_{lm}(t-t') = \frac{\zeta \omega_{m0}}{(2\pi c)^3} \frac{8\pi}{3} \eta_{lm} \int_0^\infty e^{-i(\omega_k - \omega_{m0})(t-t')} d\omega_k. \quad (\text{B.12})$$

On the other hand, we have

$$\delta(t) = \frac{1}{2\pi} \int_{-\infty}^\infty d\omega e^{i\omega t} \quad (\text{B.13})$$

as the integral expression for the Dirac delta function. Thus

$$G_{lm}(t-t') = \eta_{lm} \sqrt{\gamma_{l0} \gamma_{m0} (\omega_{m0}/\omega_{l0})} \delta(t-t'), \quad (\text{B.14})$$

where

$$\gamma_{j0} = \frac{1}{4\pi \epsilon_0} \frac{4\omega_{j0}^3 d_{j0}^2}{6\hbar c^3}, \quad (j = 1, 2) \quad (\text{B.15})$$

is half the vacuum spontaneous emission rate $\Gamma_{j0} = 2\gamma_{j0}$ for the transition $|j\rangle \rightarrow |0\rangle$. Assuming that the upper levels $|2\rangle$ and $|1\rangle$ are close together so that $\omega_{m0}/\omega_{l0} \approx 1$, we finally obtain

$$G_{lm}(t-t') = \eta_{lm} \sqrt{\gamma_{l0} \gamma_{m0}} \delta(t-t'). \quad (\text{B.16})$$

The dipole moment of a hydrogenic (one-electron) atom can be approximated by $d_{20} \sim ea_0$, where e is the magnitude of the electronic charge, and $a_0 \sim 0.5 \text{ \AA}$ is the Bohr radius. Moreover, for optical transition frequencies $\omega_{20} \sim 5 \times 10^{15} \text{ Hz}$. Using these in equation (B.15) we obtain $\gamma_{j0} \sim 10^8 \text{ s}^{-1}$.

For a PBG material described by the isotropic ‘effective mass’ dispersion relation (44), equation (B.5) takes the form

$$G_{lm}(t-t') = \frac{\zeta}{(2\pi)^3} \frac{8\pi}{3} \eta_{lm} e^{i\delta_{m0}(t-t')} \int_{k_0}^\Lambda \frac{k^2 e^{-iA(k-k_0)^2(t-t')}}{\omega_c + A(k-k_0)^2} dk, \quad (\text{B.17})$$

where $\delta_{m0} = \omega_{m0} - \omega_c$ is the detuning of the atomic transition frequency ω_{m0} from the band edge frequency ω_c . The integral in equation (B.17) can be approximated by replacing k by k_0 outside of the exponential and extending the wavevector integration to infinity, which then reduces to a complex Fresnel integral given by [181]

$$\int_0^\infty e^{-iAu^2(t-t')} du = \frac{e^{-i\pi/4}}{2\sqrt{A}} \sqrt{\frac{\pi}{t-t'}}. \quad (\text{B.18})$$

Using equations (B.3) and (B.18) in equation (B.17) we obtain

$$G_{lm}(t-t') = \eta_{lm} \sqrt{\beta_{l0}^{3/2} \beta_{m0}^{3/2}} \frac{e^{i[\delta_{m0}(t-t') - \pi/4]}}{\sqrt{\pi(t-t')}}}, \quad (\text{B.19})$$

where

$$\beta_{j0}^{3/2} = \frac{1}{4} \left(\frac{\gamma_{j0}}{\omega_{j0}} \right) \left(\frac{c \omega_c}{A^{1/2}} \right). \quad (\text{B.20})$$

This expression may be further simplified by assuming that the upper levels $|2\rangle$ and $|1\rangle$ are close together so that $\omega_{20} \approx \omega_{10}$. We then have

$$\sqrt{\beta_{l0}^{3/2} \beta_{20}^{3/2}} \approx \beta^{3/2} \equiv \frac{1}{4} \left(\frac{\gamma_{20}}{\omega_{20}} \right) \left(\frac{c \omega_c}{A^{1/2}} \right). \quad (\text{B.21})$$

Finally, using the approximation $A \approx c^2/\omega_c$, we obtain

$$\beta^{3/2} \approx \frac{1}{4} \left(\frac{\gamma_{20}}{\omega_{20}} \right) \omega_c^{3/2}. \quad (\text{B.22})$$

At optical frequencies $\gamma_{20} \sim 10^8 \text{ Hz}$ and $\omega_{20} \sim 2\pi \times 10^{15} \text{ Hz}$ so that $\beta \sim 10^{-6} \omega_c$. Thus, if the band edge ω_c is also in the optical regime, we have $\beta \sim 10^{10} \text{ Hz}$.

As shown in appendix E, for a two-level atom placed inside a PC of band edge frequency nearly resonant with the atomic transition frequency, the upper level splits into a doublet because of the strong interaction between the atom and its own localized radiation. β gives the magnitude of this frequency splitting for the isotropic dispersion relation (44). Thus for a band gap in the optical regime, $\beta \sim 10^{10} \text{ Hz}$ is larger than the ordinary vacuum Lamb shift ($\sim 10^9 \text{ Hz}$) of the $2p_{1/2}$ level of hydrogen relative to the $2s_{1/2}$ level.

For a PBG material described by the anisotropic ‘effective mass’ dispersion relation (45), the general expression (B.5) takes the form

$$G_{lm}(t-t') = \frac{\zeta}{(2\pi)^3} \frac{8\pi}{3} e^{i\delta_{m0}(t-t')} \int \left[\frac{3}{8\pi} \sum_\lambda (\hat{e}_{k\lambda} \cdot \hat{d}_{l0}) \times (\hat{e}_{k\lambda} \cdot \hat{d}_{m0}) \right] \frac{e^{-iA(k-k_0)^2(t-t')}}{\omega_c + A(\mathbf{k} - \mathbf{k}_0)^2} d^3k. \quad (\text{B.23})$$

Making the substitution $\mathbf{q} = \mathbf{k} - \mathbf{k}_0$ (so that $d^3q = q^2 dq d\Omega$), performing the angular integration, and extending the wavevector integration to infinity we obtain

$$G_{lm}(t-t') = \frac{\zeta}{(2\pi)^3} \frac{8\pi}{3} \eta_{lm} e^{i\delta_{m0}(t-t')} \frac{1}{A} \int_0^\infty \frac{e^{-iAq^2(t-t')}}{\omega_c/A + q^2} q^2 dq, \quad (\text{B.24})$$

where η_{lm} is given by equation (B.8). For large $t-t'$, the integral in equation (B.24) is dominated by the stationary phase point $q = 0$. Thus, the integral can be approximated by putting $q = 0$ in the denominator, and using

$$\int_0^\infty x^2 e^{-ax^2} dx = \sqrt{\pi} a^{-3/2}/4, \quad (\text{B.25})$$

to obtain

$$G_{lm}(t-t') = -\eta_{lm} \sqrt{\alpha_{l0} \alpha_{m0}} \frac{e^{i[\delta_{m0}(t-t') + \pi/4]}}{\sqrt{4\pi(t-t')^3}}, \quad (\text{B.26})$$

$$\omega_c(t-t') \gg 1,$$

where

$$\alpha_{j0} = \frac{1}{4} \left(\frac{\gamma_{j0}}{\omega_{j0}} \right) \left(\frac{c^3}{\omega_c A^{3/2}} \right), \quad (\text{B.27})$$

and we have used equation (B.15). Equation (B.26) may be further simplified by assuming that the upper levels $|2\rangle$ and $|1\rangle$ are close together so that $\omega_{20} \approx \omega_{10}$. We then have

$$\sqrt{\alpha_{l0} \alpha_{20}} \approx \alpha \equiv \frac{1}{4} \left(\frac{\gamma_{20}}{\omega_{20}} \right) \left(\frac{c^3}{\omega_c A^{3/2}} \right). \quad (\text{B.28})$$

The full expression of $G_{lm}(t-t')$, including its short-time behaviour, is given in [158].

Equation (B.28) shows that the value of α_{j0} strongly depends on the curvature $A = (1/2)(\partial^2\omega/\partial k^2)_{k=k_0}$ of the dispersion curve $\omega(k)$ at the band edge, $k = k_0$.

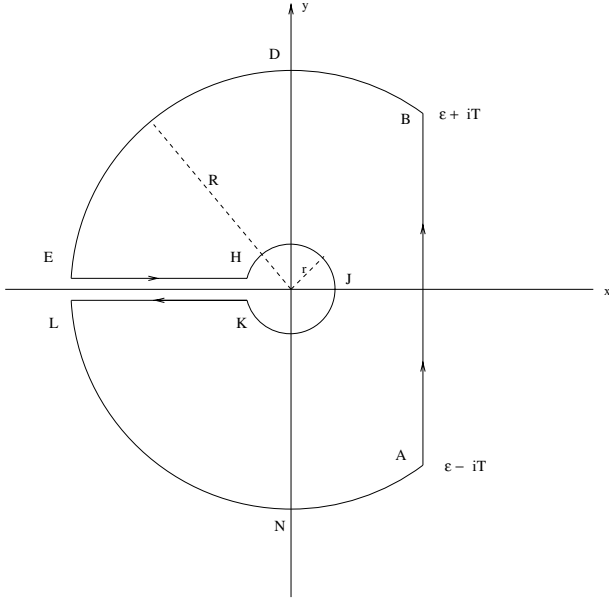


Figure C.1. The contour used in the complex inversion formula (C.1).

For the anisotropic dispersion relation we cannot use the approximation $A \approx c^2/\omega_c$ because the dispersion curve, in general, exhibits different curvatures in different directions. Instead we can use $A \approx f c^2/\omega_c$ where f is a dimensionless number, whose value depends on the nature of the dispersion relation near the band edge ω_c . This reduces equation (B.28) to

$$\alpha^2 = \frac{1}{16f^3} \left(\frac{\gamma_{20}}{\omega_{20}} \right)^2 \omega_c. \quad (\text{B.29})$$

Appendix C. Time dependence of the atomic amplitudes and the strong-field limit

In this appendix we solve the coupled integro-differential equations (28a) and (28b) for the amplitudes $c_{1,2}(t)$ in the case of a PBG described by the anisotropic dispersion relation (45). These solutions are then used to evaluate the steady-state populations on the upper levels $|1\rangle$ and $|2\rangle$ in the presence of a strong driving field coupling these levels.

In the case of a PBG, the amplitudes $c_{1,2}(t)$ are obtained from the inverse Laplace transforms of $\tilde{c}_{1,2}(s + i\delta)$ given by equations (50a) and (50b). These inverse Laplace transforms are evaluated via the complex inversion formula

$$e^{-i\delta t} c_j(t) = \frac{1}{2\pi i} \int_{\epsilon - i\infty}^{\epsilon + i\infty} e^{st} \tilde{c}_j(s + i\delta) ds, \quad (\text{C.1})$$

where the real number ϵ is chosen so that $s = \epsilon$ lies to the right of all the singularities (poles and branch points) of the functions $\tilde{c}_{1,2}(s + i\delta)$. It is apparent from equation (51) that $s = 0$ is a branch point of both $\tilde{c}_{1,2}(s + i\delta)$. In order to evaluate (C.1), we consider the contour C shown in figure C.1 where the branch cut of the integrand is chosen to lie along the negative real axis.

According to the residue theorem

$$\frac{1}{2\pi i} \oint_C e^{st} \tilde{c}_j(s + i\delta) ds = R_{\text{sum}}, \quad (\text{C.2})$$

where R_{sum} is the sum of the residues of the integrand at the poles enclosed by the contour C . Omitting the integrand, we obtain

$$R_{\text{sum}} = \frac{1}{2\pi i} \oint_C = \frac{1}{2\pi i} \left(\int_{AB} + \int_{BDE} + \int_{EH} + \int_{HJK} + \int_{KLN} + \int_{LNA} \right). \quad (\text{C.3})$$

In the limit $r \rightarrow 0$ and $R \rightarrow \infty$ (so that $T \rightarrow \infty$), the second, the fourth and the sixth integrals on the RHS of equation (C.3) approach zero and, according to equation (C.1), the first integral gives $e^{-i\delta t} c_j(t)$. Thus

$$e^{-i\delta t} c_j(t) = R_{\text{sum}} - \lim_{R \rightarrow \infty, r \rightarrow 0} \frac{1}{2\pi i} \left(\int_{EH} + \int_{KL} \right). \quad (\text{C.4})$$

First we calculate $c_2(t)$. Along EH, $s = xe^{i\pi} = -x$; and using this in equation (50a) we obtain

$$\lim_{R \rightarrow \infty, r \rightarrow 0} \int_{EH} e^{st} \tilde{c}_2(s + i\delta) ds = \int_0^\infty \frac{[(-x + i\delta) \cos \theta - \Omega e^{i\phi} \sin \theta] e^{-xt}}{(-x + i\delta)^2 - \alpha e^{-i\pi/4} (-x + i\delta) \sqrt{x} + \Omega^2} dx. \quad (\text{C.5})$$

Similarly, along KL, $s = xe^{-i\pi} = -x$; and using this in equation (50a) we obtain

$$\lim_{R \rightarrow \infty, r \rightarrow 0} \int_{KL} e^{st} \tilde{c}_2(s + i\delta) ds = - \int_0^\infty \frac{[(-x + i\delta) \cos \theta - \Omega e^{i\phi} \sin \theta] e^{-xt}}{(-x + i\delta)^2 + \alpha e^{-i\pi/4} (-x + i\delta) \sqrt{x} + \Omega^2} dx.$$

Using equations (C.5) and (C.6) in equation (C.4) we obtain

$$e^{-i\delta t} c_2(t) = R_{\text{sum}} + \frac{\alpha e^{i\pi/4}}{\pi} \int_0^\infty \frac{g_2(x) e^{-(x-i\delta)t}}{Z(x)} dx \quad (\text{C.6})$$

where

$$g_2(x) = [(-x + i\delta) \cos \theta - \Omega e^{i\phi} \sin \theta] (-x + i\delta) \sqrt{x}, \quad (\text{C.7a})$$

$$Z(x) = [(-x + i\delta)^2 + \Omega^2]^2 + i\alpha^2 (-x + i\delta)^2 x. \quad (\text{C.7b})$$

Next we evaluate the total residue R_{sum} . From equations (50a) and (51) we have

$$e^{st} \tilde{c}_2(s + i\delta) = [(s + i\delta) \cos \theta - \Omega e^{i\phi} \sin \theta] \times e^{st} \prod_{j=1}^4 \frac{\sqrt{s} + e^{i\pi/4} u_j}{s - iu_j^2}. \quad (\text{C.8})$$

Clearly, the function $e^{st} \tilde{c}_2(s + i\delta)$ has simple poles at $s = iu_j^2$, ($j = 1, \dots, 4$). The residue R_k at $s = iu_k^2$ is then

$$R_k \equiv \lim_{s \rightarrow iu_k^2} (s - iu_k^2) e^{st} \tilde{c}_2(s + i\delta) = [(u_k^2 + \delta) \cos \theta + i\Omega e^{i\phi} \sin \theta] e^{iu_k^2 t} \times \frac{(\sqrt{u_k^2 + u_1}) \cdots (\sqrt{u_k^2 + u_4})}{(u_k^2 - u_l^2)(u_k^2 - u_m^2)(u_k^2 - u_n^2)} \quad (k \neq l \neq m \neq n). \quad (\text{C.9})$$

Numerical examinations show that the roots $u_{1,3}$ are real (u_1 is positive but u_3 is negative). The roots $u_{2,4}$ are complex conjugates of each other with a negative real part (u_2 and u_4 lie in the third and second quadrants, respectively). Thus, the

negative root u_3 lies outside the contour C so that the residue at u_3 is $R_3 = 0$. For the complex root u_4 (which has a positive imaginary part), the factor $e^{iu_4^2 t}$ increases exponentially in time and therefore is unphysical. Thus, for this root we choose the negative branch of the square root function and set $\sqrt{u_4^2 + u_4} = 0$ so that the residue at u_4 is $R_4 = 0$. On the other hand, for the positive root u_1 and the complex root u_2 we choose the positive branch of the square root function and set $\sqrt{u_j^2} = u_j$, ($j = 1, 2$). The residues at u_1 and u_2 are

$$R_j = P_j Q_j e^{iu_j^2 t} \quad (j = 1, 2), \quad (\text{C.10})$$

where

$$P_j = \frac{2u_j}{(u_j - u_l)(u_j - u_m)(u_j - u_n)}, \quad (\text{C.11a})$$

$$(l, m, n = 1, \dots, 4, j \neq l \neq m \neq n),$$

$$Q_j = (u_j^2 + \delta) \cos \theta + i\Omega e^{i\phi} \sin \theta. \quad (\text{C.11b})$$

The sum of the residues of the function $e^{st} \tilde{c}_2(s + i\delta)$ is then

$$R_{\text{sum}} = \sum_{k=1}^4 R_k = \sum_{j=1}^2 P_j Q_j e^{iu_j^2 t}. \quad (\text{C.12})$$

Using this in equation (C.6) we finally arrive at the desired result (55a):

$$c_2(t) = \sum_{j=1}^2 P_j Q_j e^{i(u_j^2 + \delta)t} + \frac{\alpha e^{i\pi/4}}{\pi} \int_0^\infty \frac{g_2(x) e^{-(x-i\delta)t}}{Z(x)} dx. \quad (\text{C.13})$$

Following exactly the same procedure we also find that

$$c_1(t) = \sum_{j=1}^2 P_j R_j e^{i(u_j^2 + \delta)t} + \frac{\alpha \Omega e^{i(\phi_c - \pi/4)}}{\pi} \int_0^\infty \frac{g_1(x) e^{-(x-i\delta)t}}{Z(x)} dx \quad (\text{C.14})$$

where P_j and $Z(x)$ are the same as those for $c_2(t)$ and

$$R_j = (u_j^2 + \alpha u_j + \delta) e^{i\phi_c} \sin \theta - i\Omega e^{i\phi_c} \cos \theta, \quad (\text{C.15a})$$

$$g_1(x) = [(-x + i\delta) \cos \theta - \Omega e^{i\phi} \sin \theta] \sqrt{x}. \quad (\text{C.15b})$$

For a control laser field so strong that $\Omega \gg \alpha^2, \delta$, the roots given by equations (53a) and (53b) are approximately given by

$$u_1 \sim \sqrt{\Omega}, \quad u_2 \sim -\sqrt{\Omega}, \quad (\text{C.16})$$

$$u_2 = u_4^* \sim -\sigma_2 - i\sqrt{\Omega}, \quad \text{for } \Omega \gg \alpha^2.$$

Using these in equations (C.11a), (C.11b), and (C.15a) we obtain

$$P_1 \sim 1/2\Omega \quad (\text{C.17a})$$

$$Q_1 \sim \Omega [\cos \theta + i e^{i\phi} \sin \theta], \quad (\text{C.17b})$$

$$R_1 \sim -i\Omega e^{i\phi_c} [\cos \theta + i e^{i\phi} \sin \theta], \quad (\text{C.17c})$$

which can then be used in equations (58) and (60) to obtain

$$n_{2s} \approx n_{1s} \approx \frac{1}{4} (1 - \sin 2\theta \sin \phi), \quad (\text{C.18})$$

$$n_{cs} \approx \frac{i e^{-i\phi_c}}{4} (1 - \sin 2\theta \sin \phi)$$

for the steady-state values of populations and coherences in the limit of a strong driving field.

Appendix D. Quantum beat solutions

D.1. The vacuum case

This appendix gives the derivation of equation (73) which is the solution of the coupled equations (71a) and (71b) in the quantum beats case ($\Omega = 0$). When $\Omega = 0$, equations (71a) and (71b) reduce to

$$\dot{c}_1(t) = -\gamma_{10} c_1(t) - \eta \bar{\gamma} e^{-i\omega_{21} t} c_2(t), \quad (\text{D.1a})$$

$$\dot{c}_2(t) = -\gamma_{20} c_2(t) - \eta \bar{\gamma} e^{i\omega_{21} t} c_1(t). \quad (\text{D.1b})$$

The solution of these homogeneous linear differential equations with time-dependent coefficients is facilitated if we introduce new functions $f_j(t)$ by

$$c_j(t) = e^{-\gamma_j t} f_j(t), \quad (j = 1, 2) \quad (\text{D.2})$$

in terms of which the equations can be rewritten as

$$\dot{f}_1(t) = -\eta \bar{\gamma} e^{-i\lambda t} f_2(t), \quad (\text{D.3a})$$

$$\dot{f}_2(t) = -\eta \bar{\gamma} e^{i\lambda t} f_1(t), \quad (\text{D.3b})$$

where λ is a complex constant given by

$$\lambda = \gamma_{20} - \gamma_{10} + i\omega_{21}. \quad (\text{D.4})$$

Taking the derivative with respect to time of equation (D.3a) and using equation (D.3b) we obtain

$$\ddot{f}_2(t) - \lambda \dot{f}_2(t) - (\eta \bar{\gamma})^2 f_2(t) = 0. \quad (\text{D.5})$$

This is a second-order ordinary linear differential equation with constant coefficients. Its characteristic equation is

$$q^2 - \lambda q - (\eta \bar{\gamma})^2 = 0 \quad (\text{D.6})$$

with solutions

$$q_{1,2} = \frac{\lambda}{2} \pm \sqrt{\left(\frac{\lambda}{2}\right)^2 + (\eta \bar{\gamma})^2}. \quad (\text{D.7})$$

The general solution of equation (D.5) is thus

$$f_2(t) = A_1 e^{q_1 t} + A_2 e^{q_2 t}, \quad (\text{D.8})$$

where $A_{1,2}$ are arbitrary constants. Going back to equation (D.3b) we obtain

$$f_1(t) = -\frac{1}{\eta \bar{\gamma}} \dot{f}_2(t). \quad (\text{D.9})$$

Substituting the derivative of equation (D.8) into (D.9), we obtain

$$f_1(t) = -\frac{1}{\eta \bar{\gamma}} (A_1 q_1 e^{q_1 t} + A_2 q_2 e^{q_2 t}) e^{-\lambda t}. \quad (\text{D.10})$$

We now use the given initial values for the amplitudes $c_j(t)$ to determine the constants $A_{1,2}$. From equation (D.2) we see that $f_j(0) = c_j(0)$. Using this in equations (D.8) and (D.10), and solving the resulting coupled equations for $A_{1,2}$ we obtain

$$A_j = \frac{q_k c_2(0) + \eta \bar{\gamma} c_1(0)}{q_k - q_j}, \quad (k \neq j). \quad (\text{D.11})$$

Now that we have the solutions for $f_j(t)$, we use equation (D.2) to obtain

$$c_2(t) = e^{-\gamma_{20}t} \sum_{j=1}^2 A_j e^{q_j t}, \quad (D.12)$$

$$c_1(t) = e^{-(\gamma_{20} + i\omega_{21})t} \sum_{j=1}^2 B_j e^{q_j t},$$

where

$$B_j = -q_j A_j / \eta \bar{\gamma}. \quad (D.13)$$

This completes the solution of equations (D.1a) and (D.1b).

When $\eta = 0$, equations (D.1a) and (D.1b) have the exponentially decaying solutions given by

$$c_j(t) = c_j(0) e^{-\gamma_{j0}t}, \quad (j = 1, 2). \quad (D.14)$$

Comparing these solutions with the general solutions (D.12), we see that

$$\begin{aligned} A_1 &= 0, & A_2 &= c_2(0), & B_1 &= c_1(0), \\ B_2 &= 0; & & & & \text{for } \eta = 0. \end{aligned} \quad (D.15)$$

Next we show that the amplitudes $c_j(t)$ given by equation (D.12) decay to zero in the long-time limit:

$$\lim_{t \rightarrow \infty} c_j(t) = 0. \quad (D.16)$$

From equation (D.12), we see that equation (D.16) will be satisfied only if

$$\text{Re}\{q_{1,2}\} < \gamma_{20}, \quad (D.17)$$

where $\text{Re}\{\}$ denotes the real part of the quantity in braces. Condition (D.17) can easily be proved if we assume that $\gamma_{10} \approx \gamma_{20}$ so that $\bar{\gamma} \approx \gamma_{20}$. This is a reasonable assumption, especially if the upper levels $|2\rangle$ and $|1\rangle$ are close to each other but far from the ground level $|0\rangle$ so that $\omega_{21} \ll \omega_{20}, \omega_{10}$, as is usually the case in the V configuration. In this approximation, equation (D.4) shows that $\lambda = i\omega_{32}$ so that equation (D.7) gives

$$q_{1,2} = \begin{cases} i\omega_{21}/2 \pm x & \text{if } \eta\gamma_{20} \geq \omega_{21}/2, \\ i\omega_{21}/2 \pm ix & \text{if } \eta\gamma_{20} < \omega_{21}/2, \end{cases} \quad (D.18)$$

where

$$x = \sqrt{\left| (\eta\gamma_{20})^2 - \left(\frac{\omega_{21}}{2}\right)^2 \right|}. \quad (D.19)$$

Since $\eta \leq 1$, it follows that $x < \gamma_{20}$. From equation (D.18) we see that $\text{Re}\{q_{1,2}\} = \pm x$ if $\eta\gamma_{20} \geq \omega_{21}/2$ or $\text{Re}\{q_{1,2}\} = 0$ if $\eta\gamma_{20} < \omega_{21}/2$. Thus in both cases condition (D.17) is easily satisfied.

D.2. The PBG case

This appendix gives the derivation of equations (86a) and (86b) which are solutions to the coupled equations (84a) and (84b) in the quantum beats case ($\Omega = 0$) with $\eta = 1$, and $\delta_{20} = -\delta_{10} = \delta \geq 0$. In this special case, equations (84a) and (84b) reduce to

$$\dot{h}_1(t) = i\delta h_1(t) - \int_0^t G(t-t')[h_1(t') + h_2(t')] dt', \quad (D.20a)$$

$$\dot{h}_2(t) = -i\delta h_2(t) - \int_0^t G(t-t')[h_1(t') + h_2(t')] dt'. \quad (D.20b)$$

Upon taking the Laplace transforms of these equations, we obtain

$$\tilde{h}_1(s) = \frac{(s + i\delta)c_1(0) - \rho e^{i\pi/4} \sqrt{s}}{D(s)}, \quad (D.21a)$$

$$\tilde{h}_2(s) = \frac{(s - i\delta)c_2(0) + \rho e^{i\pi/4} \sqrt{s}}{D(s)}, \quad (D.21b)$$

where

$$\rho = \alpha[c_2(0) - c_1(0)], \quad (D.22a)$$

$$D(s) = s^2 + 2\alpha e^{i\pi/4} s \sqrt{s} - \delta^2 \prod_{j=1}^4 (\sqrt{s} - e^{i\pi/4} v_j), \quad (D.22b)$$

and α is defined in equation (48). Here v_j ($j = 1, \dots, 4$) are the roots of the quartic equation

$$x^4 + 2\alpha x^3 - \delta^2 = 0, \quad (D.23)$$

given by [159]

$$v_{1,3} = -\sigma_1/2 \pm \sqrt{(\sigma_1/2)^2 - \xi_2}, \quad (D.24a)$$

$$v_2 = v_4^* = -\sigma_2/2 - i\sqrt{\xi_1 - (\sigma_2/2)^2}, \quad (D.24b)$$

$$\sigma_{1,2} = \alpha \pm \sqrt{\alpha^2 + u}, \quad (D.24c)$$

$$\xi_{1,2} = u/2 \pm \sqrt{(u/2)^2 + \delta^2}, \quad (D.24d)$$

$$u = -(2\alpha^2 \delta^2)^{1/3} [(A+1)^{1/3} - (A-1)^{1/3}], \quad (D.24e)$$

$$A = [1 + (4/27)(2\delta/a^2)^6]^{1/2}. \quad (D.24f)$$

Equation (D.24e) shows that the quantity u is always negative. Thus ξ_1 and $\sigma_{1,2}$ are positive whereas ξ_2 is negative. Thus, the roots

$$v_{1,3} = -|\sigma_1|/2 \pm \sqrt{(\sigma_1/2)^2 + |\xi_2|} \quad (D.25)$$

are both real. Moreover, numerical analysis shows that $\xi_1 - (\sigma_1/2)^2 \geq 0$ for all δ , the equality sign holding for $\delta = 0$, that is, when the upper levels $|2\rangle$ and $|1\rangle$ are degenerate (the effective mass approximation means that δ cannot be too large). Thus, equation (D.24b) can be rewritten as

$$v_2 = v_4^* = -\sigma_2/2 - i\sqrt{|\xi_1 - (\sigma_2/2)^2|}. \quad (D.26)$$

This shows that the roots v_2 and v_4 are complex conjugates of each other. Equations (D.21a) and (D.21b) can now be inverted (following the procedure described in appendix C) to give

$$c_2(t) = \sum_{j=1}^2 S_j T_j e^{i(v_j^2 + \delta)t} + \frac{e^{i\pi/4}}{\pi} \int_0^\infty \frac{f_2(x) e^{-(x+i\delta)t} dx}{W(x)}, \quad (D.27a)$$

$$c_1(t) = \sum_{j=1}^2 S_j U_j e^{i(v_j^2 - \delta)t} + \frac{e^{i\pi/4}}{\pi} \int_0^\infty \frac{f_1(x) e^{-(x+i\delta)t} dx}{W(x)}, \quad (D.27b)$$

where

$$S_j = \frac{2v_j}{(v_j - v_l)(v_j - v_m)(v_j - v_n)}, \quad (\text{D.28a})$$

$$(l, m, n = 1, \dots, 4, j \neq l \neq m \neq n),$$

$$T_j = (v_j^2 - \delta)c_2(0) + v_j\rho = (v_j^2 + \alpha v_j - \delta)c_2(0) - \alpha v_j c_1(0), \quad (\text{D.28b})$$

$$U_j = (v_j^2 + \delta)c_2(0) - v_j\rho = (v_j^2 + \alpha v_j + \delta)c_1(0) - \alpha v_j c_2(0), \quad (\text{D.28c})$$

$$f_2(x) = [-\rho(x^2 + \delta^2) + 2\alpha c_2(0)(x + i\delta)x]\sqrt{x}, \quad (\text{D.28d})$$

$$f_1(x) = [\rho(x^2 + \delta^2) + 2\alpha c_1(0)(x - i\delta)x]\sqrt{x}, \quad (\text{D.28e})$$

$$W(x) = (x^2 + \delta^2)^2 + i4\alpha^2 x^3. \quad (\text{D.28f})$$

Appendix E. Two-level atom in the anisotropic model

In this appendix we consider a special case of our model three-level system when single-photon spontaneous emission for the transition $|1\rangle \rightarrow |0\rangle$ is assumed forbidden. This means that the population of level $|1\rangle$ cannot decay directly to level $|0\rangle$. Its only decay mechanism is indirectly through level $|2\rangle$ via the coupling Ω . Now, if the upper levels $|2\rangle$ and $|1\rangle$ are not driven by a control laser field so that $\Omega = 0$, level $|1\rangle$ will be completely decoupled from the rest of the system and our model system of figure 9 is effectively a two-level system consisting of levels $|2\rangle$ and $|0\rangle$.

In this case equations (30a) and (30b) reduce (assuming that the atom is initially on the upper level $|2\rangle$ so that $\theta = 0$) to $\tilde{c}_1(s) = 0$ and

$$\tilde{c}_2(s) = \frac{1}{s + \tilde{G}(s)}. \quad (\text{E.1})$$

Using equation (49) for $\tilde{G}(s)$ we obtain

$$\tilde{c}_2(s + i\delta) = 1/D(s), \quad (\text{E.2})$$

where

$$D(s) = s + \alpha e^{i\pi/4} \sqrt{s} + i\delta = \prod_{j=1}^2 (\sqrt{s} - e^{i\pi/4} v_j). \quad (\text{E.3})$$

Here v_j ($j = 1, 2$) are the roots of the quadratic equation

$$x^2 + \alpha x + \delta = 0 \quad (\text{E.4})$$

given by

$$v_{1,2} = -\frac{\alpha}{2} \pm \sqrt{\left(\frac{\alpha}{2}\right)^2 - \delta}. \quad (\text{E.5})$$

The amplitude $c_2(t)$ is found from the inverse Laplace transform of $\tilde{c}_2(s + i\delta)$ through the inversion integral of equation (C.1). Following the method of appendix C and using the contour of figure C.1 yields the following results:

- (a) If $\delta < 0$ (upper level $|2\rangle$ is inside the gap), the roots (E.5) are given by

$$r_{1,2} = -\frac{\alpha}{2} \pm \sqrt{\left(\frac{\alpha}{2}\right)^2 + |\delta|}. \quad (\text{E.6})$$

Thus r_1 is positive, whereas r_2 is negative and lies outside the contour of integration. In this case we obtain

$$c_2(t) = c_1 e^{i(r_1^2 + \delta)t} + I(\delta, t), \quad \delta < 0, \quad (\text{E.7})$$

where

$$c_1 = 2r_1/(r_1 - r_2), \quad (\text{E.8a})$$

$$I(\delta, t) = \frac{\alpha e^{i\pi/4}}{\pi} \int_0^\infty \frac{\sqrt{x} e^{(-x+i\delta)t}}{(-x+i\delta)^2 + i\alpha^2 x} dx. \quad (\text{E.8b})$$

- (b) If $0 \leq \delta \leq (\alpha/2)^2$, both roots $v_{1,2}$ are negative and lie outside the contour of integration. In this case we obtain

$$c_2(t) = I(\delta, t), \quad 0 \leq \delta \leq (\alpha/2)^2, \quad (\text{E.9})$$

where $I(\delta, t)$ is given by equation (E.8b).

- (c) If $\delta > (\alpha/2)^2$, the roots (E.5) are complex conjugates of each other given by

$$q_1 = q_2^* = -\frac{\alpha}{2} - i\sqrt{|\delta| - \left(\frac{\alpha}{2}\right)^2}. \quad (\text{E.10})$$

In this case the residue corresponding to q_2 is zero, and we obtain

$$c_2(t) = d_1 e^{i(q_1^2 + \delta)t} + I(\delta, t), \quad \delta > (\alpha/2)^2, \quad (\text{E.11})$$

where

$$d_1 = \frac{2q_1 \cos \theta}{q_1 - q_2}. \quad (\text{E.12})$$

Since the root r_1 is positive while the root q_1 is complex with a negative real part, the first term on the RHS of equation (E.7) is a non-decaying oscillatory term while that of equation (E.11) decays in time and tends to zero as $t \rightarrow \infty$. The term $I(\delta, t)$ also decays in time and tends to zero as $t \rightarrow \infty$. The steady-state population on the upper level $|2\rangle$ is then given by

$$n_{2s} \equiv \lim_{t \rightarrow \infty} |c_2(t)|^2 = \begin{cases} 4r_1^2/(r_1 - r_2)^2 & \text{if } \delta < 0 \\ 0 & \text{if } \delta \geq 0. \end{cases} \quad (\text{E.13})$$

Thus, for the two-level system (consisting of the ground level $|0\rangle$ and the excited-level $|2\rangle$) placed inside a PBG structure described by the ‘effective mass’ anisotropic dispersion relation equation (45), *fractionalized steady-state inversion occurs only for $\delta < 0$* , that is for $\omega_{20} < \omega_c$. On the other hand, for such a two-level system in the isotropic model equation (44), fractionalized inversion was shown [65] to occur even when ω_{20} is slightly greater than ω_c (that is, even when the excited state lies *outside* (but not far from) the band gap).

References

- [1] John S 1984 Electromagnetic absorption in a disordered medium near a photon mobility edge *Phys. Rev. Lett.* **53** 2169
- [2] John S 1987 Strong localization of photons in certain disordered dielectric superlattices *Phys. Rev. Lett.* **58** 2486
- [3] Yablonoitch E 1987 Inhibited spontaneous emission in solid-state physics and electronics *Phys. Rev. Lett.* **58** 2059
- [4] Bykov V P 1975 Spontaneous emission from a medium with a band spectrum *Sov. J. Quantum Electron.* **4** 861

- [5] John S and Wang J 1990 Quantum electrodynamics near a photonic band gap: photon bound states and dressed atoms *Phys. Rev. Lett.* **64** 2418
- [6] John S and Wang J 1991 Quantum optics of localized light *Phys. Rev. B* **43** 12772
- [7] Leung K M and Liu Y F 1990 Full vector wave calculation of photonic band structures in face-centred-cubic dielectric media *Phys. Rev. Lett.* **65** 2646
- [8] Zhang Z and Satpathy S 1990 Electromagnetic wave propagation in periodic structures: Bloch wave solution of Maxwell's equations *Phys. Rev. Lett.* **65** 2650
- [9] Ho K M, Chan C T and Soukoulis C M 1990 Existence of a photonic band gap in periodic dielectric structures *Phys. Rev. Lett.* **65** 3152
- [10] Joannopoulos J D, Meade R D and Winn J N 1995 *Photonic Crystals. Molding the Flow of Light* (Princeton, NJ: Princeton University Press)
- [11] Ho K M, Chan C T, Soukoulis C M, Biswas R and Sigalas M 1994 Photonic bandgaps in three dimensions: new layer-by-layer structures *Solid State Commun.* **89** 413
- [12] Busch K and John S 1998 Photonic band gap formation in certain self-organizing systems *Phys. Rev. E* **58** 3896
- [13] Kittel C 1980 *Introduction to Solid State Physics* (New York: Wiley)
- [14] Meystre P and Sargent M 1991 *Elements of Quantum Optics* (New York: Springer)
- Scully M O and Zubairy S 1997 *Quantum Optics* (Cambridge: Cambridge University Press)
- [15] John S 1991 Localization of light *Phys. Today* **44** 32
- [16] Yablouovitch E 1993 Photonic band-gap structures *J. Opt. Soc. Am. B* **10** 283
- [17] Ashcroft N W and Mermin N D 1976 *Solid State Physics* (San Diego, CA: Harcourt Brace College Publishers)
- [18] Satpathy S, Zhang Z and Salehpour M R 1990 Theory of photon bands in three-dimensional periodic dielectric structures *Phys. Rev. Lett.* **64** 1239
- [19] Leung K M and Liu Y F 1990 Photon band structures: the plane-wave method *Phys. Rev. B* **41** 10188
- [20] Bowden C M, Dowling J P and Everitt H O 1993 Development and applications of materials exhibiting photonic band gaps *J. Opt. Soc. Am. B* **10** 280
- [21] Kurizki G and Haus J W 1994 Special issue on photonic band structures *J. Mod. Opt.* **41** 171
- [22] Scherer A, Doll T, Yablouovitch E, Everitt H O and Higgins J A 1999 Electromagnetic crystal structures, design, synthesis, and applications *J. Lightwave Technol.* **17** 1928
- [23] Soukoulis C M (ed) 1992 Photonic band gaps and localization *Proc. NATO Advanced Research Workshop on Localization and Propagation of Classical Waves in Random and Periodic Media (Heraklion, Crete, Greece, May 1992)*
see also,
Soukoulis C M (ed) 1993 *NATO ASI Series B: Physics vol 308* (New York: Plenum)
- [24] Soukoulis C M (ed) 1995 Photonic band gap materials *Proc. Photonic Band Gap Materials (Elounda, Crete, Greece, June 1995)*
see also,
Soukoulis C M 1996 *NATO ASI Series E: Applied Sciences vol 315* (Kluwer: Academic)
- [25] Burstein E and Weisbuch C 1993 Confined electrons and photons: new physics and applications *Proc. NATO ASI Series on Confined Electrons and Photons: New Physics and Applications (Italy, July 1993)*
see also,
Burstein E and Weisbuch C 1995 *NATO ASI Series B: Physics vol 340* (New York: Plenum)
- [26] Rarity J and Weisbuch C (ed) 1995 Microcavities and photonic bandgaps: physics and applications *Proc. NATO ASI Series on Quantum Optics in Wavelength-Scale Structures (Cargese, Corsica, Aug. 1995)*
see also,
Rarity J and Weisbuch C 1996 *NATO ASI Series* (Amsterdam: Kluwer)
- [27] Dowling J, Everitt H and Yablouovitch E Photonic and sonic band-gap bibliography available at <http://www.ee.ucla.edu/labs/photon/biblio.html>
- [28] Figotin A and Klein A 1998 Localization of light in lossless inhomogeneous dielectrics *J. Opt. Soc. Am. A* **15** 1423
- [29] Hui P M and Johnson N F 1995 Photonic band gap materials *Solid State Physics* vol 49, ed H Ehrenreich and F Spaepen (New York: Academic)
- [30] Villaneuve P R and Piché M 1994 Photonic band gaps in periodic dielectric structures *Prog. Quantum Electron.* **18** 153
- [31] Joannopoulos J D, Villaneuve P R and Fan S 1997 Photonic crystals: putting a new twist on light *Nature* **386** 143
- [32] Craig D P and Thirunamachandran T 1984 *Molecular Quantum Electrodynamics* (New York: Academic)
- [33] Milonni P W 1994 *The Quantum Vacuum: an Introduction to Quantum Electrodynamics* (Boston, MA: Academic)
- [34] Mandel L and Wolf E 1995 *Optical Coherence and Quantum Optics* (New York: Cambridge University Press)
- [35] Louisell H W 1964 *Radiation and Noise in Quantum Electronics* (New York: McGraw-Hill)
- [36] Walls D F and Milburn G J 1995 *Quantum Optics* (New York: Springer)
- [37] Milonni P W and Eberly J H 1988 *Lasers* (New York: Wiley)
- [38] Haken H and Wolf H C 1996 *The Physics of Atom and Quanta: Introduction to Experiments and Theory* (Berlin: Springer)
- [39] Louisell W H 1973 *Quantum Statistical Properties of Radiation* (New York: Wiley)
- [40] Weisskopf V and Wigner E 1930 *Z. Phys.* **63** 54
- [41] Lewenstein M, Zakrzewski J and Mossberg T W 1988 Spontaneous emission of atoms coupled to frequency-dependent reservoirs *Phys. Rev. A* **38** 808
- [42] Lewenstein M, Zakrzewski J, Mossberg T W and Mostowski J 1988 Non-exponential spontaneous decay in cavities and waveguides *J. Phys. B: At. Mol. Opt. Phys.* **21** L9
- [43] Raizen M G, Thomson R J, Brecha R J, Kimbel H J and Carmichael H J 1989 Normal-mode splitting and linewidth averaging for two-state atoms in an optical cavity *Phys. Rev. Lett.* **63** 240
- [44] Purcell E M 1946 Spontaneous emission probabilities at radio frequencies *Phys. Rev.* **69** 681
- [45] Haroche S and Kleppner D 1989 Cavity quantum electrodynamics *Phys. Today* **24**
- [46] Berman P R (ed) 1994 *Cavity Quantum Electrodynamics* (New York: Academic)
- [47] Hinds EA 1991 *Adv. At. Mol. Opt. Phys.* **28** 237
- [48] Kleppner D 1981 Inhibited spontaneous emission *Phys. Rev. Lett.* **47** 233
- [49] Milonni P W and Knight P L 1973 Spontaneous emission between mirrors *Opt. Commun.* **9** 119
- [50] Gérard J, Sermage B, Gayral B, Legrand B, Costard E and Thierry-Mieg V 1998 Enhanced spontaneous emission by quantum boxes in a monolithic optical microcavity *Phys. Rev. Lett.* **91** 110
- [51] Wangsness R K 1979 *Electromagnetic Fields* (New York: Wiley)
- [52] Vredenberg A M, Hunt N E J, Schubert E F, Jacobson D C, Poate J M and Zydick G J 1993 Controlled atomic spontaneous emission for Er^{3+} in a transparent Si/SiO₂ microcavity *Phys. Rev. Lett.* **71** 517
- [53] Tanaka K, Nakamura T, Takamatsu W, Yamanishi M, Lee Y and Ishihara T 1995 Cavity-induced changes of spontaneous emission lifetime in one-dimensional semiconductor microcavities *Phys. Rev. Lett.* **74** 3380
- [54] Graham L A, Huffaker D L, Deng Q and Deppe D G 1998 Controlled spontaneous lifetime in microcavity confined InGaAlAs/GaAs quantum dots *Appl. Phys. Lett.* **72** 1670
- [55] Dowling J P and Bowden C M 1992 Atomic emission rates in

- inhomogeneous media with applications to photonic band structures *Phys. Rev. A* **46** 612
- [56] Martorell J and Lawandy N M 1990 Observation of inhibited spontaneous emission in a periodic dielectric structure *Phys. Rev. Lett.* **65** 1877
- [57] Tong B Y, John P K, Zhu Y, Liu Y S, Wong S K and Ware W R 1993 Fluorescence-lifetime measurements in monodispersed suspensions of polystyrene particles *J. Opt. Soc. Am. B* **10** 356
- [58] Petrov E P, Bogomolov V N, Kalosha I I and Gaponenko S V 1998 Spontaneous emission of organic molecules in a photonic crystal *Phys. Rev. Lett.* **81** 77
- [59] Yamasaki T and Tsutsui T 1998 Spontaneous emission from fluorescent molecules embedded in photonic crystals of polystyrene microspheres *Appl. Phys. Lett.* **72** 1957
- [60] Yoshino K, Lee S B, Tatsuhara S, Kawagishi Y, Ozaki M and Zakhidov A A 1998 Observation of inhibited spontaneous emission and stimulated emission of rhodamine 6G in polymer replica of synthetic opal *Appl. Phys. Lett.* **73** 3506
- [61] López C, Blanco A, Míguez H and Meseguer F 1999 Photonic crystals for laser action *Opt. Mater.* **13** 187
- [62] Megens M, Wijnhoven J E G J, Lagendijk A and Vos W L 1999 Fluorescence lifetimes and linewidths of dye in photonic crystals *Phys. Rev. A* **59** 4727
- [63] Blanco A, López C, Mayoral R, Míguez H, Meseguer F, Mifsud A and Herrero J 1998 CdS photoluminescence inhibition by a photonic crystal *Appl. Phys. Lett.* **73** 1781
- Romanov S G, Fokin A V, Alperovich V I, Johnson N P and De La Rue R M 1997 The effect of the photonic stop-band upon the photoluminescence of CdS in opal *Phys. Status Solidi a* **164** 169
- [64] Gaponenko S V, Bogomolov V N, Petrov E P, Kapitonov A M, Yarotsky D A, Kalosha I I, Eychmueller A A, Rogach A L, McGilp J, Woggon U and Gindele F 1999 Spontaneous emission of dye molecules, semiconductor nanocrystals, and rare-earth ions in opal-based photonic crystals *J. Lightwave Technol.* **17** 2128
- [65] John S and Quang T 1994 Spontaneous emission near the edge of a photonic band gap *Phys. Rev. A* **50** 1764
- [66] Quang T, Woldeyohannes M, John S and Agarwal G S 1997 Coherent control of spontaneous emission near a photonic band edge: a single-atom optical memory device *Phys. Rev. Lett.* **79** 5238
- [67] Woldeyohannes M and John S 1999 Coherent control of spontaneous emission near a photonic band edge: a qubit for quantum computation *Phys. Rev. A* **60** 5046
- [68] Mollow B R 1969 Power spectrum of light scattered by two-level systems *Phys. Rev.* **188** 1969
- [69] For a review of work on strong-field resonance fluorescence, see Knight P L and Milonni P W 1980 The Rabi frequency in optical spectra *Phys. Rep.* **66** 21
- [70] Allen L and Eberly J H 1975 *Optical Resonance and Two-level atoms* (New York: Wiley)
- [71] Autler H and Townes C H 1955 Stark effect in rapidly varying fields *Phys. Rev.* **100** 703
- [72] Picqué J L and Pinard J 1976 Direct observation of the Autler–Townes effect in the optical range *J. Phys. B: At. Mol. Phys.* **9** L77
- [73] Deslart C and Keller J-C 1976 Observation of the optical Autler–Townes splitting in neon gas with a cascade level scheme *J. Phys. B: At. Mol. Phys.* **9** 2769
- [74] Lewenstein M, Mossberg T W and Glauber R J 1987 Dynamical suppression of spontaneous emission *Phys. Rev. Lett.* **59** 775
- Lewenstein M and Mossberg T W 1988 Spectral and statistical properties of strongly driven atoms coupled to frequency-dependent photon reservoirs *Phys. Rev. A* **37** 2048
- [75] Schultz S and Smith D R Measurements of localization and photonic band gap systems in two dimensions, in [24]
- [76] Smith D R, Dalichaouch R, Kroll N and Schultz S 1993 Photonic band structure and defects in one and two dimensions *J. Opt. Soc. Am. B* **10** 314
- [77] Pendry J B and Mackinnon A 1992 Calculation of photon dispersion relation *Phys. Rev. Lett.* **69** 2772
- Pendry J B 1994 Photonic band structures *J. Mod. Opt.* **41** 209
- [78] Chan C T, Yu Q L and Ho K M 1995 Order-N spectral method for electromagnetic waves *Phys. Rev. B* **51** 16635
- [79] Moglievtsev D, Birks T A and St Russel P J 1999 Localized function for modeling defect modes in 2D photonic crystals *J. Lightwave Technol.* **17** 2078
- [80] Painter O J, Husain A, Scherer A, O'Brien J D, Kim I and Dapkus P D 1999 Room temperature photonic crystal defect lasers at near-infrared wavelengths in InGaAsP *J. Lightwave Technol.* **17** 2082
- [81] Yablonovitch E, Gimtter T J and Leung K M 1991 Photonic band structure: the face-centred case employing nonspherical atoms *Phys. Rev. Lett.* **67** 2295
- Yablonovitch E and Leung K M 1991 Hope for photonic bandgaps *Nature* **351** 278
- [82] Leung K M Plane-Wave calculation of photonic band structure, in [24]
- [83] Sözüer H S and Dowling J P 1994 Photonic band calculations for woodpile structures *J. Mod. Opt.* **41** 231
- [84] Fan S, Villeneuve P R, Meade R D and Joannopoulos J D 1994 Design of three-dimensional photonic crystals at submicron length scales *Appl. Phys. Lett.* **65** 1466
- [85] Ozbay E, Abeyta A, Tuttle G, Tringides M, Biswas R, Chan C T, Soukoulis C M and Ho K M 1994 Measurement of three-dimensional photonic band gap in a crystal structure made of dielectric rods *Phys. Rev. B* **50** 1945
- [86] Yamamoto N, Noda S and Chutinan A 1998 Development of one period of a three-dimensional photonic crystal in the 5 μm wavelength region by wafer fusion and laser beam diffraction pattern observation techniques *Japan. J. Appl. Phys.* **37** L1052
- [87] Lin S Y, Fleming J G, Hetherington D L, Smith B K, Biswas R, Ho K M, Sigalas M M, Zubrzycki W, Kurtz S R and Bur J 1998 A three-dimensional photonic crystal operating at infrared wavelengths *Nature* **394** 251
- [88] Fleming J G and Lin S-Y 1999 Three-dimensional photonic crystal with a stop band from 1.35–1.95 μm *Opt. Lett.* **24** 49
- [89] Noda S, Yamamoto N, Imada M, Kobayahi H and Okano M 1999 Alignment and stacking of semiconductor photonic band gaps by wafer-fusion *J. Lightwave Technol.* **17** 1948
- [90] Economu E N and Sigalas M M 1993 Classical wave propagation in periodic structures: cermet versus network topology *Phys. Rev. B* **48** 13434
- [91] Mann S and Ozin G A 1996 *Nature* **382** 313
- [92] Cheng C C and Scherer A 1995 Fabrication of photonic band-gap crystals *J. Vac. Sci. Technol. B* **13** 2696
- [93] Tarhan I I and Watson G H 1996 Photonic band structure of fcc colloidal crystal *Phys. Rev. Lett.* **76** 315
- [94] Pradhan R D, Bloodgood J A and Watson G H 1997 Photonic band structure of bcc colloidal crystals *Phys. Rev. B* **55** 9503
- [95] Vos W L, Sprik R, van Blaaderen A, Imhof A, Langendijk A and Weydam G H 1996 Strong effects of photonic band structures on the diffraction of colloidal crystals *Phys. Rev. B* **53** 16231
- Vos W L, Megens M, van Kats C M and Bosecke P 1996 Transmission and diffraction by photonic colloidal crystals *J. Phys.: Condens. Matter* **8** 9503
- [96] Vlasov Yu A, Astratov V N, Karimov O Z, Kaplyanskii A A, Bogomolov V N and Prokofiev A V 1997 Existence of a photonic pseudogap for visible light in synthetic opals *Phys. Rev. B* **55** R13357 (rapid communications)
- [97] Bogomolov V N, Gaponenko S V, Gemnanenko I N, Kapitonov A M, Petrov E P, Gaponenko N V, Prokofiev A V, Ponyavina A N, Silvanovitch N I and Samoilovitch S M

- 1997 Photonic band gap phenomenon and optical properties of artificial opals *Phys. Rev. E* **55** 7619
- [98] Míguez H, Lopez C, Meseguer F, Blanco A, Vazquez L, Mayoral R, Ocana M, Fornes V and Mifsud A 1997 Photonic crystal properties of packed submicrometric SiO₂ spheres *Appl. Phys. Lett.* **71** 1148
- [99] Míguez H, Blanco B, López C, Meseguer F, Yates H M, Pemble M E, López-Tejiera F, García-Vidal F J and Sánchez-Dehesa J 1999 Face centred cubic photonic band gap materials based on opal–semiconductor composites *J. Lightwave Technol.* **17**
- [100] Mayoral R, Requena J, Moya J S, López C, Cintas A, Míguez H, Meseguer F, Vázquez L, Holgado M and Blanco A 1997 3D long range ordering in a SiO₂ submicrometric–sphere sintered superstructure *Adv. Matter.* **9** 257
- [101] Wijnhoven J E G J and Vos W L 1998 Preparation of photonic crystals made of air spheres in titania *Science* **281** 802
- [102] Imhof A and Pine D J 1997 Ordered macroporous materials by emulsion templating *Nature* **389** 948
- [103] Velev A, Jede T A, Lobo R F and Lenhoff A M 1997 Porous silica via colloidal crystallization *Nature* **389** 448
- [104] Holland B T, Blanford C F and Stein A 1998 Synthesis of macroporous minerals with highly ordered three-dimensional arrays of spheroidal voids *Science* **281** 538
- [105] Zakhidov A and Baughman R H 1998 Carbon structures with three-dimensional periodicity at optical wavelengths *Science* **282** 897
- [106] Vlasov Yu A, Yao N and Norris D J 1999 Synthesis of photonic crystals for optical wavelengths from semiconductor quantum dots *Adv. Matter.* **11** 165
- [107] Toader O, John S and Busch K 2001 Optical trapping, Field Enhancement, and Laser cooling in photonic crystals *Opt. Exp.* **8** 217–22
- [108] Xia Y, Gates B and Park S H 1999 Fabrication of three-dimensional photonic crystals for use in the spectral region from ultraviolet to near-infrared *J. Lightwave Technol.* **17** 1956
- [109] Blanco A, Chomski E, Grabtchak S, Ibisate M, John S, Leonard S W, Lopez C, Meseguer F, Míguez H, Mondia J P, Ozin G A, Toader O and van Driel H M 2000 Large-scale synthesis of a silicon photonic crystal with a complete three-dimensional band gap near 1.5 micrometres *Nature* **405** 437
- [110] Boroditsky M, Vrijen R, Krauss T F, Coccioli R, Bhat R and Yablonovitch E 1999 Spontaneous emission extraction and Purcell enhancement from thin-film 2D photonic crystals *J. Lightwave Technol.* **17** 2096
- [111] Baba T, Inoshita K, Tanaka H, Yoenkura J, Ariga M, Matsutani A, Miyamoto T, Koyama F and Iga K 1999 Strong enhancement of light extraction efficiency in GaInAsP 2D-arranged micro-columns *J. Lightwave Technol.* **17** 2113
- [112] Barnes W L 1999 Electromagnetic crystals for surface plasmon polaritons and the extraction of light from emissive devices *J. Lightwave Technol.* **17** 2170
- [113] Fan S, Villeneuve P R and Joannopoulos J D 1997 High extraction efficiency of spontaneous emission from slabs of photonic crystals *Phys. Rev. Lett.* **78** 3294
- [114] Lawandy N M and Kweon G Molecular and free electron spontaneous emission in periodic three-dimensional dielectric structures, in [24]
- [115] Yablonovitch E Photonic band structure, in [24]
- [116] Brown E R, Parker C D and Yablonovitch E 1993 Radiation properties of a planar antenna on a photonic crystal substrate *J. Opt. Soc. Am. B* **10** 404
- [117] Brown E and McMahon O 1996 High zenithal directivity from a dipole antenna on a photonic crystal *Appl. Phys. Lett.* **68** 1300
- [118] Kesler M, Maloney J, Shirley B and Smith G 1996 Antenna design with the use of photonic band-gap materials as all-dielectric planar reflectors *Microw. Opt. Technol. Lett.* **11** 169
- [119] Rutledge D B, Neikirk D P and Kasilingam D P 1983 *Infrared and Millimeter Waves* (Orlando, FL: Academic)
- [120] Yokoyama H and Brorson S D 1989 Rate equation analysis of microcavity lasers *J. Appl. Phys.* **66** 4801
- [121] Bjork G and Yamamoto Y 1991 Analysis of semiconductor microcavity lasers using rate equations *IEEE J. Quantum Electron.* **27** 2386
- [122] Jaynes E T and Cummings F W 1963 Comparison of quantum and semiclassical radiation theories with application to the beam maser *Proc. IEEE* **51** 89
- [123] Mekis A, Chen J C, Kurland I, Fan S, Villeneuve P R and Joannopoulos J J 1996 High transmission through sharp bends in photonic crystal wave guides *Phys. Rev. Lett.* **77** 3787
- [124] Lin S Y, Chow E, Hietola V, Villeneuve P R and Joannopoulos J D 1998 Experimental demonstration of guiding and bending of electromagnetic waves in a photonic crystal *Science* **282** 274
- [125] Fink Y, Ripin D J, Fan S, Chen C, Joannopoulos J D and Thomas E L 1999 Guiding optical light in air using an all-dielectric structure *J. Lightwave Technol.* **17** 2039
- [126] El-Kady I, Sigalas M M, Biswas R and Ho K M 1999 Dielectric waveguides in two-dimensional photonic bandgap materials *J. Lightwave Technol.* **17** 2042
- [127] Becker P C, Olsson N A and Simpson J R 1999 *Erbium-Doped Fiber Amplifiers. Fundamentals and Technology* (London: Academic)
- [128] Kosaka H, Kawashima T, Tomita A, Notomi M, Tamamura T, Sato T and Kawakami S 1999 Superprism phenomena in photonic crystals *J. Lightwave Technol.* **17** 2032
- Kosaka H, Kawashima T, Tomita A, Notomi M, Tamamura T, Sato T and Kawakami S 1998 *Phys. Rev. B* **58** 10096
- [129] Genereux F, Leonard S W and van Driel H M Large birefringence in two-dimensional silicon photonic crystals *Phys. Rev. B* (submitted brief reports)
- [130] Hecht E 1975 *Schaum's Outline of Theory and Problems of Optics* (New York: McGraw-Hill)
- [131] Krauss T F, De La Rue R M and Brand S 1996 Two-dimensional photonic-bandgap structures operating at near-infrared wavelengths *Nature* **383** 699
- [132] Baba T and Matsuzaki T 1996 GaInAsP/InP 2-dimensional photonic crystals *Microcavities and Photonic Bandgaps: Physics and Applications* ed J Rarity and C Weisbuch (Dordrecht: Kluwer)
- [133] Lin H-B, Tonucci R J and Campillo A J 1996 Observation of two-dimensional photonic band behaviour in the visible *Appl. Phys. Lett.* **68** 2927
- [134] Rosenberg A 1996 Near infrared two-dimensional photonic band-gap materials *Opt. Lett.* **21** 830
- [135] Sakoda K 1995 Transmittance and Bragg reflectivity of two-dimensional photonic lattices *Phys. Rev. B* **52** 8992
- [136] Benisty H, Weisbuch C, Labilloy D, Rattier M, Smith C J M, Krauss T F, De La Rue R M, Houdré R, Oesterle U, Jouanin C and Cassagne D 1999 Optical and confinement properties of two-dimensional photonic crystals *J. Lightwave Technol.* **17** 2063
- [137] Mekis A, Fan S and Joannopoulos J D 1998 Bound states in photonic crystal waveguides and waveguide bends *Phys. Rev. B* **58** 4809
- [138] Pottier P, Seassal C, Letartre X, Leclercq J L, Viktorovitch P, Cassagne D and Jouanin C 1999 Triangular and hexagonal high *Q*-factor 2D photonic bandgap cavities on III–V suspended membranes *J. Lightwave Technol.* **17** 2058
- [139] Painter O, Vučković J and Scherer A 1999 Defect modes of a two-dimensional photonic crystal in an optically thin dielectric slab *J. Opt. Soc. Am. B* **16** 275
- [140] Chen J C, Haus H A, Fan S, Villeneuve P R and Joannopoulos J D 1996 Optical filters from photonic band gap air bridges *J. Lightwave Technol.* **14** 2575

- [141] Painter O, Lee R K, Yariv A, Scherer A, O'Brien J D, Dapkus P D and Kim I 1999 Two-dimensional photonic bandgap defect mode laser *Science* **284** 1819
- [142] Meade R D, Deveny A, Joannopoulos J D, Alerhand O L, Smith D A and Kash K 1994 Novel applications of photonic band gap materials: low-loss bends and high Q cavities *J. Appl. Phys.* **75** 4753
- [143] Lourtioz J-M, de Lustrac A, Gadot F, Rowson S, Chelnokov A, Brillat T, Ammouche A, Danglot J, Van Bésien O and Lippens D 1999 Toward controllable photonic crystals for centimeter- and millimetre-wave devices *J. Lightwave Technol.* **17** 2025
- [144] John S and Busch K 1999 Liquid-crystal photonic-band-gap materials: the tunable electromagnetic vacuum *Phys. Rev. Lett.* **83** 967
John S and Busch K 1999 *Phys. Rev. Focus* **4** story 7 (circuits of light)
- [145] John S and Busch K 1999 Photonic bandgap formation and tunability in certain self-organizing systems *J. Lightwave Technol.* **17** 1931
- [146] Blinov L M and Chigrinov V G 1994 *Electro-Optic Effects in Liquid Crystal Materials* (New York: Springer)
- [147] Florescu M and John S 2001 Single atom switching in photonic crystals *Phys. Rev. A* **64** 0033801
- [148] Shnitman A, Sofer I, Golub I, Yogev A and Shapiro M 1996 Experimental observation of laser control: electronic branching in the photodissociation of Na_2 *Phys. Rev. Lett.* **53** 2886
- [149] Bandrauk A D and Wallace S C (ed) 1992 *Coherence Phenomena in Atoms and Molecules in Laser Field* (New York: Plenum)
- [150] Wang Feng, Chen Ce and Elliott D S 1996 Product state control through interfering excitation routes *Phys. Rev. Lett.* **77** 2416
- [151] Atanasov R, Hach A, Hughes J L P, van Driel H M and Sipe J E 1996 Coherent control of photocurrent generation in bulk semiconductors *Phys. Rev. Lett.* **76** 1703
- [152] Bay S, Lambropoulos P and Molmer K 1996 Atom-atom interaction at the edge of a photonic band gap *Opt. Commun.* **132** 257
- [153] Gerry C C and Eberly J H 1990 Dynamics of a Raman coupled model interacting with two quantized cavity fields *Phys. Rev. A* **42** 6805
- [154] Zhu Shi-Yao, Narducci L M and Scully M O 1995 Quantum-mechanical interference effects in the spontaneous-emission spectrum of a driven atom *Phys. Rev. A* **42** 4791
- [155] Loudon R 1983 *The Quantum Theory of Light* (Oxford: Clarendon)
- [156] Cohen-Tannoudji C, Diu B and Laloë F 1977 *Quantum Mechanics* vol 1 (Toronto: Wiley)
- [157] Spiegel M R 1965 *Schaum's Outline of Theory and Problems of Laplace Transforms* (New York: McGraw-Hill)
- [158] Vats N and John S 1998 Non-Markovian quantum fluctuations and superradiance near a photonic band edge *Phys. Rev. A* **58** 4168
- [159] Korn G A and Korn T M 1968 *Mathematical Handbook for Scientists and Engineers* (New York: McGraw-Hill)
- [160] Zhu Shi-Yao, Chen H and Huang H 1997 Quantum interference effects in spontaneous emission from an atom embedded in a photonic band gap structure *Phys. Rev. Lett.* **79** 205
- [161] Zhu Shi-Yao, Yang Y, Chen H, Zheng H and Zubairy M S 2000 Spontaneous radiation and Lamb shift in three-dimensional photonic crystals *Phys. Rev. Lett.* **84** 2136
- [162] DiVincenzo D and Terhal B 1998 Decoherence: the obstacle to quantum computation *Phys. World* **11** 53
- [163] Zhu Shi-Yao, Chan Ricky CF and Lee Chin Pang 1995 Spontaneous emission from a three-level atom *Phys. Rev. A* **52** 710
- [164] Whitley R M and Stroud C R Jr 1976 Double optical resonance *Phys. Rev. A* **14** 1498
- [165] Davis P J and Rabinowitz P 1984 *Methods of Numerical Integration* (New York: Academic)
- [166] John S and Quang T 1995 Photon-hopping conduction and collectively induced transparency in a photonic band gap *Phys. Rev. A* **52** 4083
- [167] John S and Quang Tran 1996 Quantum optical spin-glass state of impurity two-level atoms in a photonic band gap *Phys. Rev. A* **76** 1320
- [168] Dicke R H 1954 Coherence in spontaneous emission processes *Phys. Rev.* **93** 99
- [169] Gross M and Haroche S 1982 Superradiance: an essay on the theory of collective spontaneous emission *Phys. Rep.* **93** 301-96
- [170] Busch K, Vats N, Sanders B C and John S 2000 Radiating dipoles in photonic crystals *Phys. Rev. E* **62** 4251
- [171] Brennen G K, Caves C M, Jessen P S and Deutsch I H 1999 Quantum logic gates in optical lattices *Phys. Rev. Lett.* **82** 1060
- [172] Vats N and Rudolph T 2001 Quantum information processing in localized modes of light within a photonic band-gap material *J. Mod. Opt.* **48** 1495
- [173] Lanzerstorfer S, Palmeshofer L, Jantsch W and Stimmer J 1998 On the environment of optically active Er in Si-electroluminescence devices *Appl. Phys. Lett.* **72** 809
- [174] Masterov V F, Nasredinov F S, Seregin P P, Kudoyarova V Kh, Kuznetsov A N and Terukov E I 1998 Local environment of erbium atoms in amorphous hydrogenated silicon *Appl. Phys. Lett.* **72** 728
- [175] Zhao X, Komuro S, Isshiki H, Aoyagi Y and Sugano T 1999 Fabrication and stimulated emission of Er-doped nanocrystalline Si waveguides formed on Si substrates by laser ablation *Appl. Phys. Lett.* **74** 120
- [176] Komuro S, Katsumata T, Morikawa T, Zhao X, Isshiki H and Aoyagi Y 1999 Time response of 1.54 μm emission from highly Er-doped nanocrystalline Si thin films prepared by laser ablation *Appl. Phys. Lett.* **74** 377
- [177] Metcalf H J and van der Straten P 1999 *Laser Cooling and Trapping* (New York: Springer)
- [178] Gammon D, Snow E S and Katzer D S 1995 Excited state spectroscopy of excitons in single quantum dots *Appl. Phys. Lett.* **67** 2391
- [179] Sakurai J J 1994 *Modern Quantum Mechanics* (New York: Addison-Wesley)
- [180] Bethe H A 1947 The electromagnetic shift of energy levels *Phys. Rev.* **72** 339
- [181] Gradshteyn I S and Ryzhik I M 1980 *Table of Integrals, Series, and Products* (New York: Academic)